

# Schlussbericht vom 28.06.2023

---

zu IGF-Vorhaben Nr. 290 EBG

## Thema

Rapid prototyping of sheet metal parts using intelligent 3D-printed dies

## Berichtszeitraum

01.01.2021 - 31.12.2022

## Forschungsvereinigung

Deutsche Forschungsvereinigung für Meß-, Regelungs- und Systemtechnik e.V. - DFMRS

## Forschungseinrichtung(en)

1. Fraunhofer-Gesellschaft e.V.

Fraunhofer-Institut für Werkzeugmaschinen und Umformtechnik IWU

2. Universität Bremen

Bremer Institut für Messtechnik, Automatisierung und Qualitätswissenschaft (BIMAQ)

Gefördert durch:

Authors: J. Glänsel<sup>1</sup>, A. Geist<sup>1</sup>, A. Pierer<sup>1</sup>, D. Weise<sup>1</sup>, A. Fischer<sup>2</sup>, M. Terlau<sup>2</sup>, Ł. Madej<sup>3</sup>,  
K. Perzynski j<sup>3</sup>, F. Rosoux<sup>4</sup>

<sup>1</sup> Fraunhofer Institute for Machine Tools and Forming Technology

<sup>2</sup> Universität Bremen, Bremer Institut für Messtechnik, Automatisierung und Qualitätswissenschaft (BIMAQ)

<sup>3</sup> AGH University of Science and Technology, Krakow, Poland

<sup>4</sup> SIRRIS, Liège/Wallonia, Belgium

This final report is both CORNET final report and IGF final report.

## Table of Contents

1	Project Summary.....	5
2	Projektzusammenfassung .....	6
3	Administrative Data of the Project .....	7
3.1	Title of the project .....	7
3.2	Coordinator and partners .....	7
3.2.1	Coordinating association Germany: Deutsche Forschungsvereinigung für Meß-, Regelungs- und Systemtechnik e.V. (DFMRS).....	7
3.2.2	Coordinating association Poland: Centrum Promocji Innowacji i Rozwoju Koordynator Klastra Obróbki Metali (Metal Processing Cluster) .....	7
3.2.3	Coordinating association Belgium: Sirris .....	7
3.2.4	Research Partner: University of Bremen, Bremen Institute for Metrology, Automation and Quality Science (BIMAQ) .....	8
3.2.5	Research partner: Fraunhofer Institute of Machine Tools and Forming Technology (IWF) .....	8
3.2.6	Research partner: AGH Krakow .....	8
3.2.7	Research partner: Sirris.....	9
4	State of the Art .....	10
4.1	Incremental Sheet Metal Forming .....	10
4.1.1	ISF and its process variants .....	12
4.1.2	ISF Process Design.....	12
4.1.3	Demarcation to other research projects.....	13
4.1.4	TPIF with flexible counter tools as counter tools and alternatives .....	13
4.2	Tool deflection measurement.....	15
4.3	Simulation technologies .....	16
4.4	Additive manufacturing .....	16
5	Research Method.....	18
6	Cooperation of the Project Partners and Project Execution .....	20
7	Introduction to the Work Program.....	21
7.1	WP1: Analysis of requirements for machine tool concept for combined AM and ISF .....	21
7.2	WP2: Development of system for deflection monitoring and compensation .....	25
7.3	WP3: Development of a machine tool concept and technology for combined AM and ISF .....	38
7.4	WP4: Development and qualification of AM technology .....	44
7.5	WP5: Virtual twins for simulation of manufacturing process and machine tool behavior .....	58

7.6	WP6: Integration of developed technologies and iterative optimization of developed machine tool system and process technologies.....	77
7.7	WP7: Verification on real components .....	79
7.8	WP8: Project management.....	102
8	Summary and Outlook.....	103
9	Comparison of the results with the objectives of the proposal .....	104
10	Use of the grant.....	106
11	Explanation of the necessity and appropriateness of the work performed .....	107
12	Demonstration of the Scientific, Technical and Economic Benefits of the Results Obtained, in Particular for SMEs, as well as their Innovative Contribution and Industrial Applications.....	108
13	Update of the plan submitted with the application for the transfer of results to industry, supplemented by an assessment of the feasibility of this transfer concept, which also includes all work published or to be published shortly in connection with the project..	110
Annex	.....	115
Annex 1: References.....		115

## 1 Project Summary

Economic and automatable manufacturing of high-quality customized sheet metal parts in a growing variety and with decreasing lot size is a challenge for industrial production. Especially in conventional forming technologies like deep drawing and stretch drawing, high tool costs and a close linking of tools and part geometry complicate solving this task. Already the implementation of slight variations implicates high cost and time effort. To encounter these challenges, incremental sheet metal forming (ISF) is a promising alternative for manufacturing complex components in small quantities. Thereby, a forming stylus forms the final part successively by a CNC-controlled movement over a counter tool. In comparison to conventional drawing methods, this reduces tool costs and time required to achieve the first finished part. However, in the current state of the art, the manufacturing of the ISF-counter tool takes place in a separate conventional milling process, which causes high invest and operational costs (for machine tool plus ISF-machine), material waste during the counter tool manufacturing due to chip removal and an increased manufacturing time.

**RapidSheet combined additive technologies for the manufacturing of the counter tool and the ISF-process.** In the first step, the machine tool manufactured the counter tool in a large-scale additive manufacturing (AM or 3D-printing) process that fulfills requirements such as fast production of a large bulk part with high surface quality, sufficient hardness, and highly accurate geometry also for nearly flat horizontal areas. After the printing, the machine tool formed sheet metal parts. The future optimization of the AM process and the ISF-process requires compensation strategies to avoid thermal and material behavior depending on deviations (e.g. necking and spring-back effects) as well as tool deviations due to forming forces. Based on that RapidSheet put a spotlight on very complex in-process deviation measurements and simulative investigations, which had to solve difficult cross-domain problems (e.g. material behavior, thermal deviations). To tackle this challenge, new numerical simulation models with an adaptive refinement of meshes were developed in this project. Based on these simulations an optimized manufacturing strategy was deduced.

Technological and scientific challenges rised in the following tasks:

- adaptive FE Simulation of the ISF and AM processes. Simulation-based compensation strategies for geometrical deviations of parts and counter tools,
- development of dedicated AM technology ready for the integration into machine tools,
- demonstration of combined AM and ISF-processes,
- development of process and machine monitoring systems for ensuring optimal final part geometry and reliable machine operation.

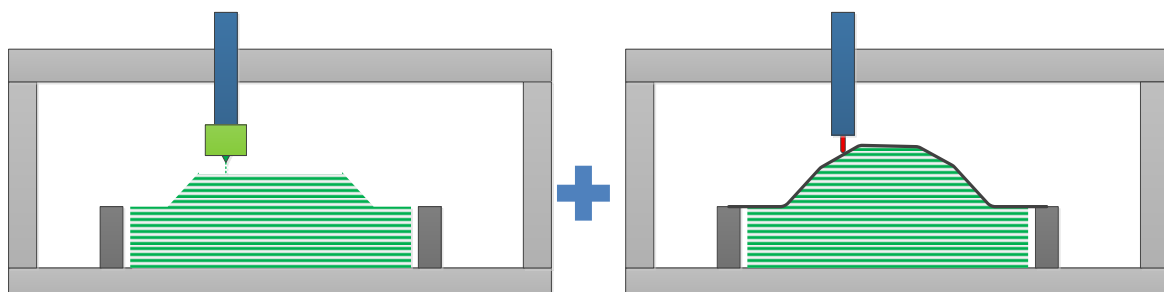


Figure 1: Left: 1st step - 3D-printing of the counter tool; Right: 2nd step - incremental sheet metal forming with a forming stylus

## 2 Projektzusammenfassung

Die wirtschaftliche und automatisierbare Herstellung hochwertiger kundenspezifischer Blechteile in wachsender Vielfalt und mit sinkenden Losgrößen ist eine Herausforderung für die industrielle Produktion. Insbesondere bei konventionellen Umformtechnologien wie Tief- und Streckziehen erschweren hohe Werkzeugkosten und eine enge Kopplung von Werkzeug und Bauteilgeometrie die Lösung dieser Aufgabe. Bereits die Umsetzung geringer Varianten ist mit einem hohen Kosten- und Zeitaufwand verbunden. Um diesen Herausforderungen zu begegnen, ist die inkrementelle Blechumformung (IBU) eine vielversprechende Alternative für die Herstellung komplexer Bauteile in kleinen Stückzahlen. Dabei formt ein Umformdorn durch eine CNC-gesteuerte Bewegung über ein Gegenwerkzeug sukzessive das Endteil. Dies reduziert im Vergleich zu konventionellen Ziehverfahren die Werkzeugkosten und den Zeitaufwand bis zum ersten Fertigteil. Nach heutigem Stand der Technik erfolgt die Herstellung des ISF-Gegenwerkzeugs jedoch in einem separaten konventionellen Fräsvorprozess, was hohe Investitions- und Betriebskosten (für Werkzeugmaschine plus IBU-Maschine), Materialabfall bei der Gegenstempelherstellung durch die Spanabfuhr und eine erhöhte Fertigungszeit verursacht.

RapidSheet hat additive Technologien für die Herstellung des Gegenwerkzeugs mit dem IBU-Prozess kombiniert. Im ersten Schritt hat die Werkzeugmaschine das Gegenwerkzeug in einem additiven Fertigungsprozess (AM oder 3D-Druck) hergestellt, der Anforderungen wie die schnelle Herstellung eines großen Bauteils mit hoher Oberflächenqualität, ausreichender Härte und hochgenauer Geometrie auch für nahezu flache horizontale Bereiche erfüllt. Anschließend wurden die Blechteile mittels IBU in der Werkzeugmaschine ausgeformt.

Die zukünftige Optimierung des AM-Prozesses und des IBU-Verfahrens erfordert Kompensationsstrategien zur Vermeidung von Abweichungen (z.B. therm. Verzug und Rückfederungseffekte) sowie von Werkzeugabweichungen aufgrund von Umformkräften. Darauf aufbauend legte RapidSheet einen Schwerpunkt auf sehr komplexe prozessbegleitende Abweichungsmessungen und simulative Untersuchungen, die schwierige bereichsübergreifende Probleme (z.B. Materialverhalten, thermische Abweichungen) lösten. Hierfür wurden in diesem Projekt neue numerische Simulationsmodelle mit einer adaptiven Netzverfeinerung entwickelt. Auf der Grundlage dieser Simulationen wurde eine optimierte Fertigungsstrategie abgeleitet.

Technologische und wissenschaftliche Herausforderungen ergaben sich aus den folgenden Aufgaben:

- adaptive FE-Simulation der IBU- und AM-Prozesse. Simulationsbasierte Kompensationsstrategien für Geometrieabweichungen von Teilen und Werkzeugen,
- Entwicklung einer speziellen AM-Technologie, die in Werkzeugmaschinen integriert werden kann,
- Demonstration von kombinierten AM- und IBU-Prozessen,
- Entwicklung von Prozess- und Maschinenüberwachungssystemen zur Gewährleistung einer optimalen Endteilgeometrie und eines zuverlässigen Maschinenbetriebs.

### 3 Administrative Data of the Project

#### 3.1 Title of the project

RapidSheet - Rapid prototyping of sheet metal parts using intelligent 3D-printed dies  
(IGF 290 EBG)

Acronym: RapidSheet

#### 3.2 Coordinator and partners

##### 3.2.1 Coordinating association Germany: Deutsche Forschungsvereinigung für Meß-, Regelungs- und Systemtechnik e.V. (DFMRS)

Address: Linzer Str. 13, 28359 Bremen

Tel.: +49 4222 950 218

Fax: +49 4222 950 219

Website: [www.dfmrs.de](http://www.dfmrs.de)

Contact: Michael Sorg

Tel.: +49 4222 950 218

E-mail: [sor@dfmrs.de](mailto:sor@dfmrs.de)

##### 3.2.2 Coordinating association Poland: Centrum Promocji Innowacji i Rozwoju Koordynator Klastra Obróbki Metali (Metal Processing Cluster)

Address: Żurawia 71 lok. 2.04 (Białystok Science and Technology Park), 15-540 Białystok

Tel.: +48 85 722 24 56

Website: [www.metalklaster.pl/en](http://www.metalklaster.pl/en)

Contact: Sebastian Rynkiewicz

Tel.: +48 501 432 426

E-mail: [biuro@metalklaster.pl](mailto:biuro@metalklaster.pl), [s.rynkiewicz@metalklaster.pl](mailto:s.rynkiewicz@metalklaster.pl)

##### 3.2.3 Coordinating association Belgium: Sirris

Address: Liège Science Park. Rue du Bois Saint-Jean, 12, 4102 Seraing Liège/Wallonia

Tel.: +32 4 361 87 00

Fax: +32 4 361 87 02

Website: [www.sirris.be](http://www.sirris.be)  
Contact: Didier Garray  
Tel.: +32 498 91 93 31  
E-mail: [Didier.garray@sirris.be](mailto:Didier.garray@sirris.be)

### **3.2.4 Research Partner: University of Bremen, Bremen Institute for Metrology, Automation and Quality Science (BIMAQ)**

Address: Linzer Str. 13, 28359 Bremen, Germany  
Tel.: +49 (0) 421 / 218-64600  
Fax: +49 (0) 421 / 218-64670  
Website: [www.bimaq.de/](http://www.bimaq.de/)  
Contact: Dr. Ing. Dirk Stöbener  
Tel.: +49 (0) 421 / 218-64640  
E-Mail: [d.stoebener@bimaq.de](mailto:d.stoebener@bimaq.de)

### **3.2.5 Research partner: Fraunhofer Institute of Machine Tools and Forming Technology (IWU)**

Address: Reichenhainer Straße 88, 09126, Chemnitz, Germany  
Tel.: +49 (0) 371 / 5397-0  
Fax: +49 (0) 371 / 5397-1404  
Website: [www.iwu.fraunhofer.de](http://www.iwu.fraunhofer.de)  
Contact: Dr.-Ing. Janine Gläzel  
Tel.: +49 (0) 371 / 5397-1218  
E-mail: [janine.glaenzel@iwu.fraunhofer.de](mailto:janine.glaenzel@iwu.fraunhofer.de)

### **3.2.6 Research partner: AGH Krakow**

Address: Mickiewicza 30 av., 30-059, Krakow, Poland  
Tel.: +48 12 617 20 07  
Fax: +48 12 423 35 70

Website: [www.agh.edu.pl](http://www.agh.edu.pl)  
Contact: Prof. Dr.-Ing. habil. Łukasz Madej  
Tel.: +48 12 617 51 54  
E-mail: [lmadej@agh.edu.pl](mailto:lmadej@agh.edu.pl)

### **3.2.7 Research partner: Sirris**

Address: Liège Science Park. Rue du Bois Saint-Jean, 12, 4102 Seraing Liège/Wallonia  
Tel.: +32 4 361 87 00  
Fax: +32 4 361 87 02  
Website: [www.sirris.be](http://www.sirris.be)  
Contact: Didier Garray  
Tel.: +32 498 91 93 31  
E-mail: [Didier.garray@sirris.be](mailto:Didier.garray@sirris.be)

## 4 State of the Art

### 4.1 Incremental Sheet Metal Forming

Incremental forming is a technique for forming sheet metals by the application of step-by-step incremental feed to a stylus. For the production of parts by conventional sheet forming techniques, dedicated tools are required. The dedicated tools are complex 3D design and thus are expensive. The design of counter tools for complicated shapes is very difficult and costly. The simplest variant of incremental forming technique needs only a stylus for forming the sheet metals. Industrial relevant geometries need a counter tool (Figure 2), but still save the main (cost-intensive) parts of a drawing tool.

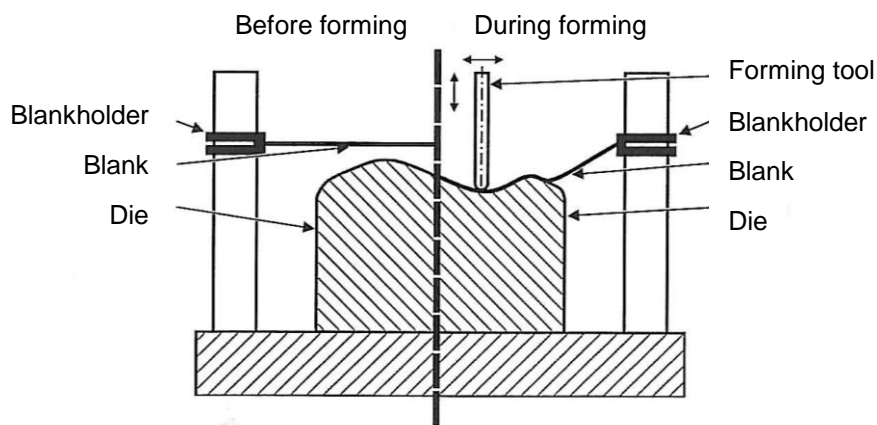


Figure 2: Process principle of incremental sheet forming

As a result of more than three decades of incremental sheet metal forming establishing itself as an interesting and cost-efficient forming technology for discrete manufacturing, the applications of this technology can be found in different sectors. Different shapes, dimensions and materials are possible (Figure 3).

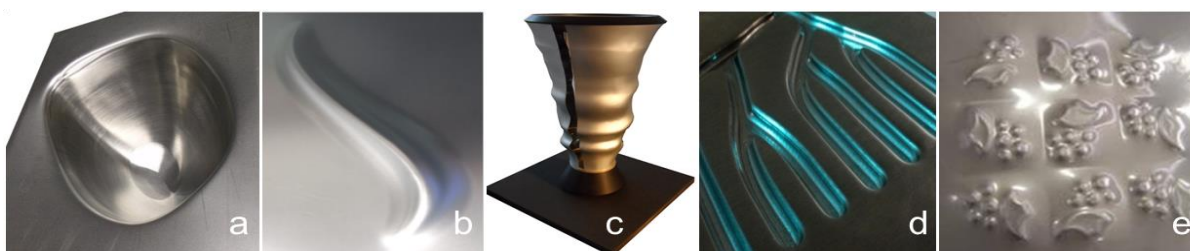


Figure 3: ISF applications: a) bowl, b) bead, c) trophy, d) channels [all FhG-IWU], e) floor tile [1, 2]

Main advantages of ISF are:

- Short time-to-market: ISF partially or totally eliminates the need for part dependent tools (Figure 4). In many cases, only a CNC programmed tool track is needed.
- ISF is cost effective for small to medium sized series (no complex and expensive tools but higher forming times; Figure 4). ISF is typical cost effective up to 300-700 pieces [3].
- ISF provides a high degree of flexibility and can be adapted to very different geometries, materials and conditions. Changes in part design can be easily and quickly accommodated.
- ISF enables producing parts of almost any size. The size is only limited by available hardware (e. g. the machine at FhG-IWU enables to form sheets up to 3,000 mm x 4,000 mm).
- ISF offers high reproducibility and enables producing sheet metal parts with improved properties (hardness, strength, etc.).

More than 50 % time reduction in process is expected compared to traditional techniques (manual forming), which will reduce the time to market. Additionally, this process-methodology is based on CAX tools, allowing a direct CAD file - physical part connection, with simple tools. Therefore, part modifications - unavoidable in some sectors, can easily be handled.

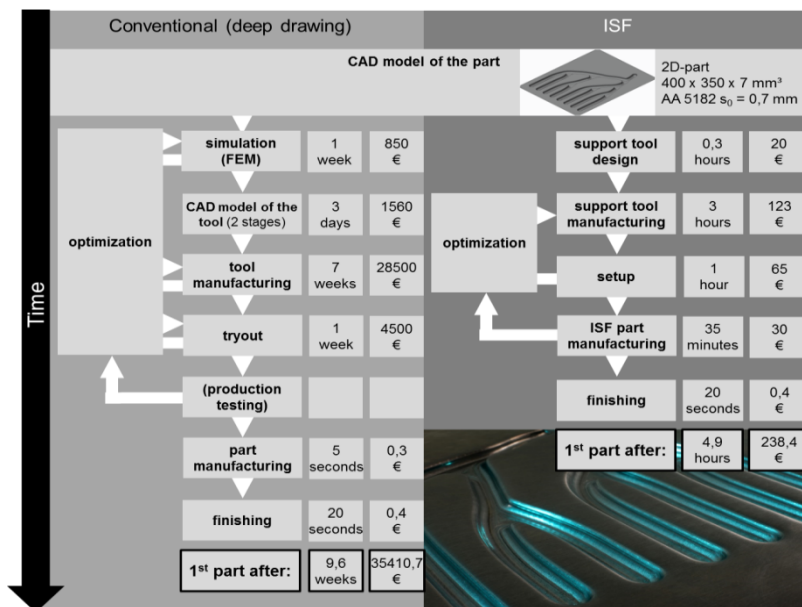


Figure 4: Comparison of deep drawing and ISF for a 2D-part

#### 4.1.1 ISF and its process variants

ISF refers to a procedure in which the workpiece shape is gradually generated by several successive movements of the tool or active component [4]. ISF is often classified by the support below the workpiece: without supporting tool, with full or partial counter tool, or with kinematical counter tool (Figure 5):

- Single Point Incremental Forming (SPIF): SPIF, i.e. ISF without counter tool was developed by Jeswiet, Leach and Filice [5, 6, 7]. For this method, no counter plate or tool is required.
- Incremental backward bulge forming/TPIF (Two-point incremental forming): TPIF was developed in 1993 by Powell and Andrew [8] and applied by Matsubura [9]. For this method, there are two points where force is introduced into the sheet. Partial or full counter tools are used as counter plates. Components for automotive industry and medical technology were formed successfully [10]. Due to its high flexibility and simplicity in terms of control TPIF was used as benchmark technology in RapidSheet.
- Kinematic Support Incremental Forming (Kinematic TPIF (KISF)): KISF is a process variant of TPIF. Here, the geometry is formed by two CNC controlled tools, so that forming without geometry dependent counter tools is enabled. Here, the challenge is to control the movement of the secondary tool depending on the positioning of the forming tool. Well known research institutes for this technique are Ruhr-Universität Bochum and MTA SZTAKI.

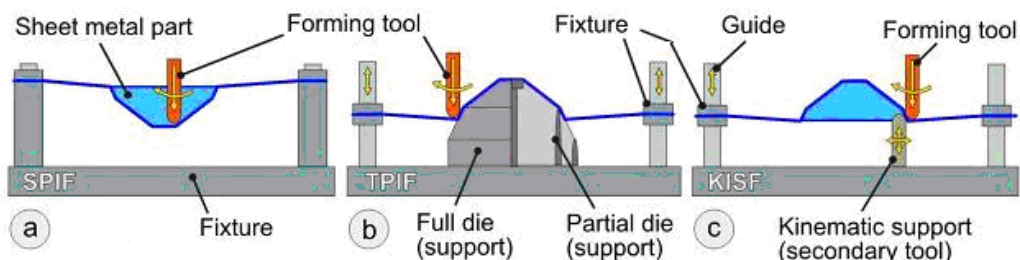


Figure 5: Process variants of ISF [11]

#### 4.1.2 ISF Process Design

The motion of the stylus is planned to use a geometric programming package, CAD/CAM (computer-aided manufacturing), which provides a CNC trajectory, analogue to a milling trajectory with a spherical tool. The forming tool axis should coincide with the normal to the surface in most cases. The axis of the supporting tool can be on the same line as that of the forming tool.

When using straight forward milling tool paths, the geometric accuracy of parts is not sufficient. To increase the accuracy, different strategies are being researched [12, 13, 14, 15, 16]. Due to the limited tool size in ISF deformations occur in a small zone only. Thus, high strains are introduced locally and no material flow into the forming zone is possible resulting in a limited formability [17].

Compared to conventional methods as deep drawing, ISF requires much lower forces, because of the gradual force application and the limited plastic forming scope. Research on

forces in ISF leading to useful models for force prediction has been performed e.g. by Jeswiet and Duflou [18], [19].

Most ISF research focusses on the forming of a part starting from a flat blank and without interaction with other processes. Hence, simple clamping rigs are used. However, the majority of industrial parts necessitate working on preformed parts and varying contours to be clamped and cut.

In the context of Rapid Prototyping, ISF made a limited introduction in industrial environment. Examples of companies, which are testing the technology, are Beauvary GmbH ([www.beauvary.com](http://www.beauvary.com)) in Germany and OCAS N.V. ([www.ocas.be](http://www.ocas.be)) in Belgium. Both companies use the method for producing prototypes and small series for different industrial fields.

#### **4.1.3 Demarcation to other research projects**

There are other research projects dealing with incremental sheet metal forming. Within the FOSTA project P738 [SIBUform – Increasing the productivity and the range of applications in incremental sheet forming by combining it with stretch forming] incremental sheet metal forming was combined with stretch drawing. A special equipment and furthermore software tools for CAD/CAM integration were developed.

FOSTA project P846 [Investigation on the producibility by incremental sheet forming of free form cladding and façade elements as self-bearing structure without substructure made of stainless steel] presents a new concept for self-supporting lightweight structures for the realization of freeform surfaces. The project aims on flexible production of façade elements mainly based on incremental sheet forming. A prototype building was realized showing the potential of the proposed production method.

Within the FOSTA project P571 [Process limits and material behavior in incremental CNC-controlled sheet metal forming], forming limits and achievable geometries (i. e. radius) were investigated. Furthermore a variation of process parameters was used to analyze their effects on geometrical accuracy, surface quality and mechanical properties of the formed parts.

A flexible counter tool was not part of investigation in those projects.

#### **4.1.4 TPIF with flexible counter tools as counter tools and alternatives**

In two point incremental forming the following concepts for a flexible counter tool can be used:

1. The counter plate is made of an elastic material: In deep-drawing elastic elements on punch or counter tool are state of the art. A transfer to the ISF is possible. In this case the elastic material indicates a counter force of the operation stylus.
2. Fluid medium as flexible counter tool (Figure 6): In hydroforming operations, a fluid is used instead of solid tool. It allows a constant pressure on the whole surface. A flexible counter tool filled with a fluid is possible for incremental forming. Because of the volume constancy of the fluid, a sensitive pressure regulation is necessary. A sheet metal multipoint forming technology based on hydroforming is discussed in [20].

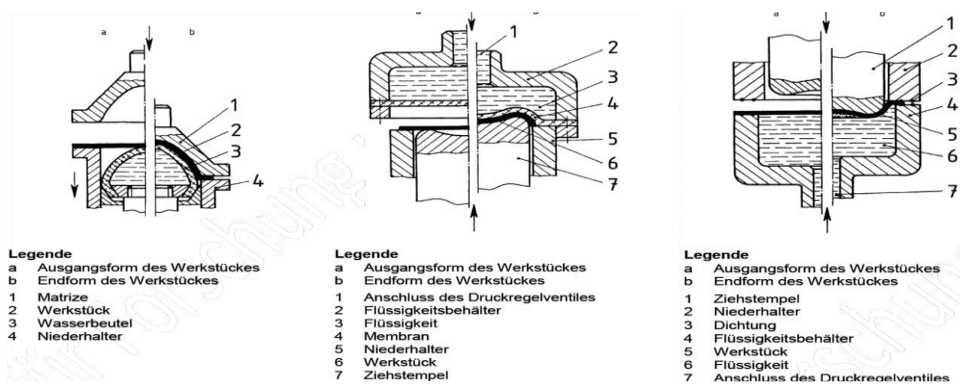


Figure 6: f.l.t.r: Drawing with water bag, drawing with membranes, drawing with one sided liquid pressure [21]

3. Metal foam as flexible counter tool: Aluminum foam is an appropriate material for a flexible counter tool. Its geometry is self-configuring during the forming operation and so it represents an interesting alternative for the manufacturing of i.e. prototypes [22].

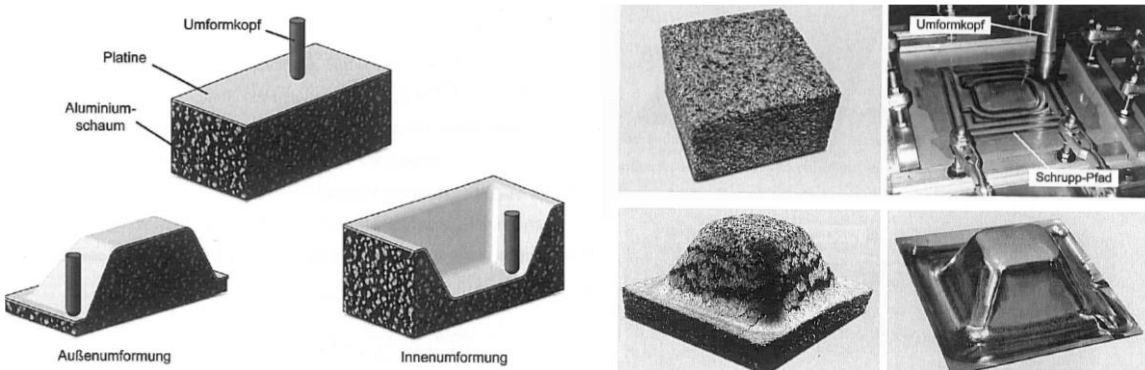


Figure 7: ISF with aluminum foam counter tools [23]

4. Flexible counter tool with multipoint forming concept: The idea of a multipoint forming counter tool is a highly flexible geometry generated with a multitude of movable pins. For each geometry, the pins are driven in the right position. Several studies deal with this concept [24, 25, 26].

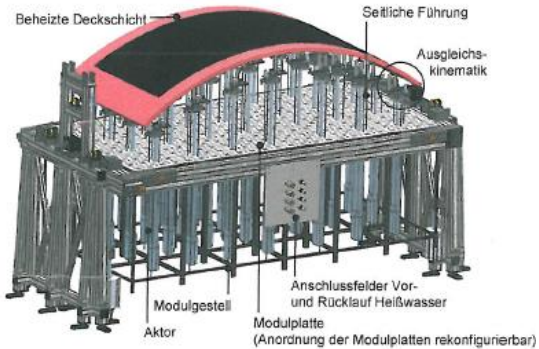


Figure 8: Multipoint tool [27]

If a different technological alternative than counter tool less forming technology is chosen, it will occur a significant increase of economic requirements that is caused by technological times, purchased price of added material or the price of the tool.

The resulting shape can be milled from a solid material. The blank is then usually a large piece of steel which is expensive to buy. Milling times are long and more than 90% of the material is waste and the process is a very non-ecological and uneconomical option.

Another possibility is a 3D printing. This variant is particularly time consuming. The profiled sheet will have a poor surface that will be caused by the remnants of the supports in the place of printing. Large sizes cannot be printed.

The product can be manufactured using simple hand tools. The costs are very low, but the quality of the workmanship is very bad. There will be roughly centimeters of deviation from the real shape. For the most part, defective pieces will be produced.

In addition, a tailored drawing tool can be produced and sheet can be formed. This variant is described above and it is absolutely unsuitable for single-purpose machines due to its financial and time demand.

## 4.2 Tool deflection measurement

One disadvantage of ISF is that major geometrical deviations occur due to spring back [28] and tool deflection [29]. Compensation of these effects require determinating them. Based on forming force measurements, an in-situ springback compensation during forming is possible, but a purely vertical forming force was considered. For large and thick sheets, the greater forming forces cause the stylus to be significantly deflected, which was not taken into account in this study. To determine the tool deflection, a prediction of the tool deflection using mechanical calculations is performed [30]. However, these predictions are based on model assumptions and do not consider the machine tool error or deformations of the machine tool. Therefore, a tool deflection measurement is preferred instead.

In conventional production machines, the tool position is detected during the process for control purposes by integrated sensors such as glass scales [31]. If the tool is subjected to strong forming forces, static and dynamic deformations of the supporting structures for the tool head can occur. The integrated sensors cannot detect these effects, so that external sensors are

required, which must be capable of measuring the three-dimensional tool tip position in the ISF process. So, the measurement system has to work contact-less and fast, capturing the tool position close to the tool tip in a single shot. Additionally, the measurement system shall be independent of the machine tool kinematics. To meet the requirements for an in-process deflection measurement of the moving tool, optical measurement systems are reasonable approaches.

To cover the entire machining volume during the ISF-process, tracking measurement approaches, i. e. tracking laser interferometry, are reasonable. Laser trackers are usually applied to measure the machine tool error [32]. Even in robotic ISF, a laser tracker has been applied to measure the tool center position in order to control the forming process in real time [33]. However, to determine the tool deflection and the machine deformation, a reflector must be attached close to the tool tip. The tracked reflector at the tool tip might move out of the system's field of view during a loss of view and then the tracking system fails. An alternative is using a triangulation principle based on a camera-based measurement system. Using cameras is advantageous due to their comparably low costs and large measuring range [34]. However, the tool tip is only present in a few pixels in an image. Solutions are limiting the measurement range per camera and increasing the information content in the image by imaging the shadow of an LED attached to the tool tip [35]. Therefore, camera-based measurement systems are promising approaches for measuring the tool deflection in ISF.

### 4.3 Simulation technologies

Most of the numerical simulations of elasto-plastic material deformation conditions are carried out through finite element (FE) methods, which can be successfully used in modeling of standard plastometric tests (e.g. compression, tension, torsion) as well as complicated metal forming operations [36]. So, the accuracy of a FE solution is particularly related to a proper description of the material hardening behavior. In the classical FE packages, direct solution methods are used which entail long calculation times due to the "fill-in" that occurs. The unique generation of the FE-mesh leads to an unchangeable uniform area mesh with a shorter computing complexity and time. The conventional FEM with protected source code of the algorithms can be adapted via user interfaces. Adaptivity means that the local FE-meshing is controlled by a residence-based a-posteriori error estimator to optimally refine step-width of the FE-mesh [37,38,39].

### 4.4 Additive manufacturing

Additive manufacturing, commonly also known as "3D printing", is a process that creates three-dimensional objects, generally sliced into horizontal layers. This manufacturing technique can work with either metals, polymers, ceramics or biochemical. The main difference with classical manufacturing is the additive character of the technique whereas classical processes generally consist in removing materials. As machine tool manufacturers have also made efforts in the past to improve the productivity and accuracy of their machines in the context of several research projects, complex 3D components can be manufactured ever faster. Due to the high accuracy, which is increasingly in the two-digit micrometer range, reworking of the printed parts is generally no longer necessary. 5-axis milling is therefore in close competition with 3D printing. For the production of the dies, additive or machining processes can be considered. The advantages of machining are as follows:

- Faster than 3D printing for large, state-of-the-art parts

- Can be easily implemented on conventional series machines such as the DMU80 or HEC630

However, the energy and environmental aspects are more favorable for additive processes, such as 3D printing, for the following reasons:

- Production of raw material for machining processes is very energy-intensive;
- Machining process needs a lot of energy (several kW el. power of the machine)
- Chips are considered waste with little environmental awareness
- 3D printing of thermoplastics is more energy efficient
- Printed parts can be easily recycled (remelting or pelletising) to feed the printer again, thus creating a closed material cycle.

Thermoplastic materials are easy to reuse, as they can be remelted as often as required whereas the required thermal energy is significantly lower compared to metal materials. For this reason, additive processes are ideal for resource-saving and sustainable production. Among the different techniques existing in the additive manufacturing market and according to the scope of the project, the study will be mainly based on material extrusion processes for their accessibility in terms of cost and ease of use.

This additive manufacturing technique (generally called FDM - fused deposition modelling - or FFF - fused filament fabrication) commonly uses spooled polymers, extruded through a heated nozzle, which causes the polymer to melt. The material (generally PLA, ABS, PET) is then deposited layer by layer on a heated bed to ensure good adhesion and reduce warping.

Alternatives exist to the classical material extrusion method. For example, concerning small scale parts, Hyrel commercializes printing heads working on the syringe principle and able to print with exotic materials such as pastes or gels. Concerning feeding of materials, pellets are also considered, especially for larger scales thanks to their higher productivity and lower cost compared to spooled filament. In fact, according to Titan Robotics, flow rates for filament extrusion are about 3 kg/day whereas for pellet feeding some higher values were found in the literature. Pellets extruders can be either mounted on robotic arms or on large 3-axes machines such as the Atlas from Titan Robotics. According to the data collected in the literature, it can be clearly seen that pellets extrusion is certainly more advantageous for the present application with its higher productivity. Finally, one has also to mention the fact that pellets and filament extruders can be combined on the same machine to take advantage of each: productivity for pellet and higher resolution of filament-based printing heads.

## 5 Research Method

The research method put the AM and the ISF technologies in a central position in the project. The phenomenological description of the thermal process behavior during the AM and the ISF-process was based on a complex mathematical model. The resulting simulation tool led to significant progress in the simulation of the production of complex shapes. Macro scale calculations also had been supported by micro scale modelling based on a digital material representation concept [40] and heat transfer Lamé-simulations coupled via the temperature-dependent stress tensor [41]. For process simulation, thermal and thermo-elastic simulations were particularly suitable to determine the thermal behavior in the extruder and the printed part. In Figure 9 the necessary systems are highlighted, which can be considered simulatively within the project.

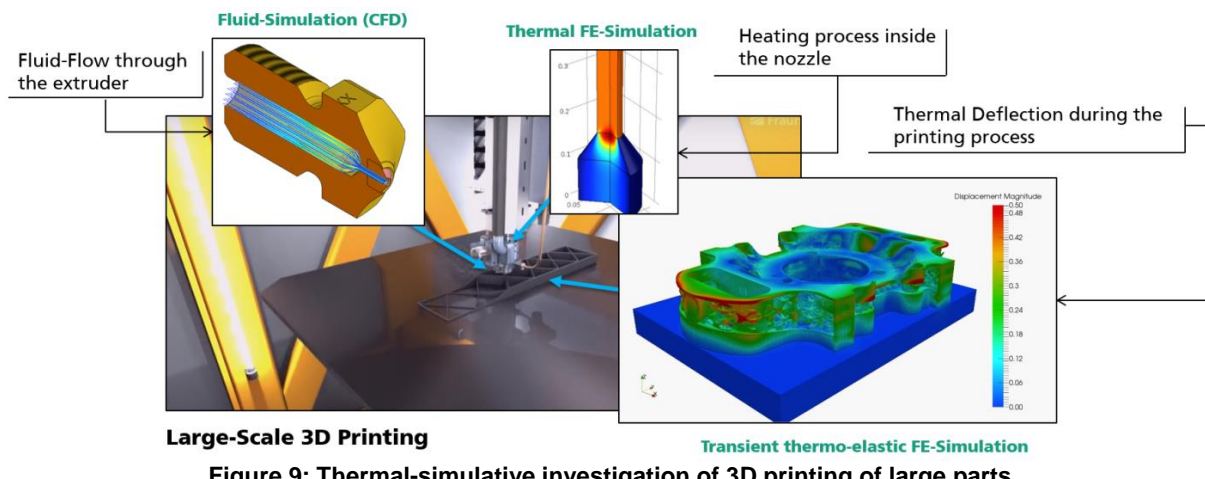


Figure 9: Thermal-simulative investigation of 3D printing of large parts

In order to consider the thermally induced expansion and shrinkage of the printed part, a time-resolved simulation during the entire printing process was necessary. Thus, the thermal expansions could be taken into account in real-time by a concurrent correction in the control system. The necessity for this is shown by the example of thermal expansion for the thermoplastic material "Acrylonitrile-Butadien-Styrene" (ABS), for which a thermal expansion coefficient of  $60 - 110 \mu\text{m}/(\text{m}\cdot\text{K})$  applies. This is almost 10 times the value of steel. Especially during the ISF-process the machine deflection is a limiting factor regarding achievable precision. For this reason, a global deflection monitoring system had been developed and integrated in the manufacturing process.

For the development and adaption of the full process chain steps, research was based on existing knowledge of the partners, literature and a stepwise approach from small size to large-scale oriented tests, which eased to determine feasible process parameters and enabled correct decisions to be made at the milestones. The outcomes had been discussed by the consortium and user committee. Afterwards, optimization strategies had been applied. The final step as part of this eight WP (Figure 10) was the transfer of the gathered knowledge into applications at SMEs of the user committee.

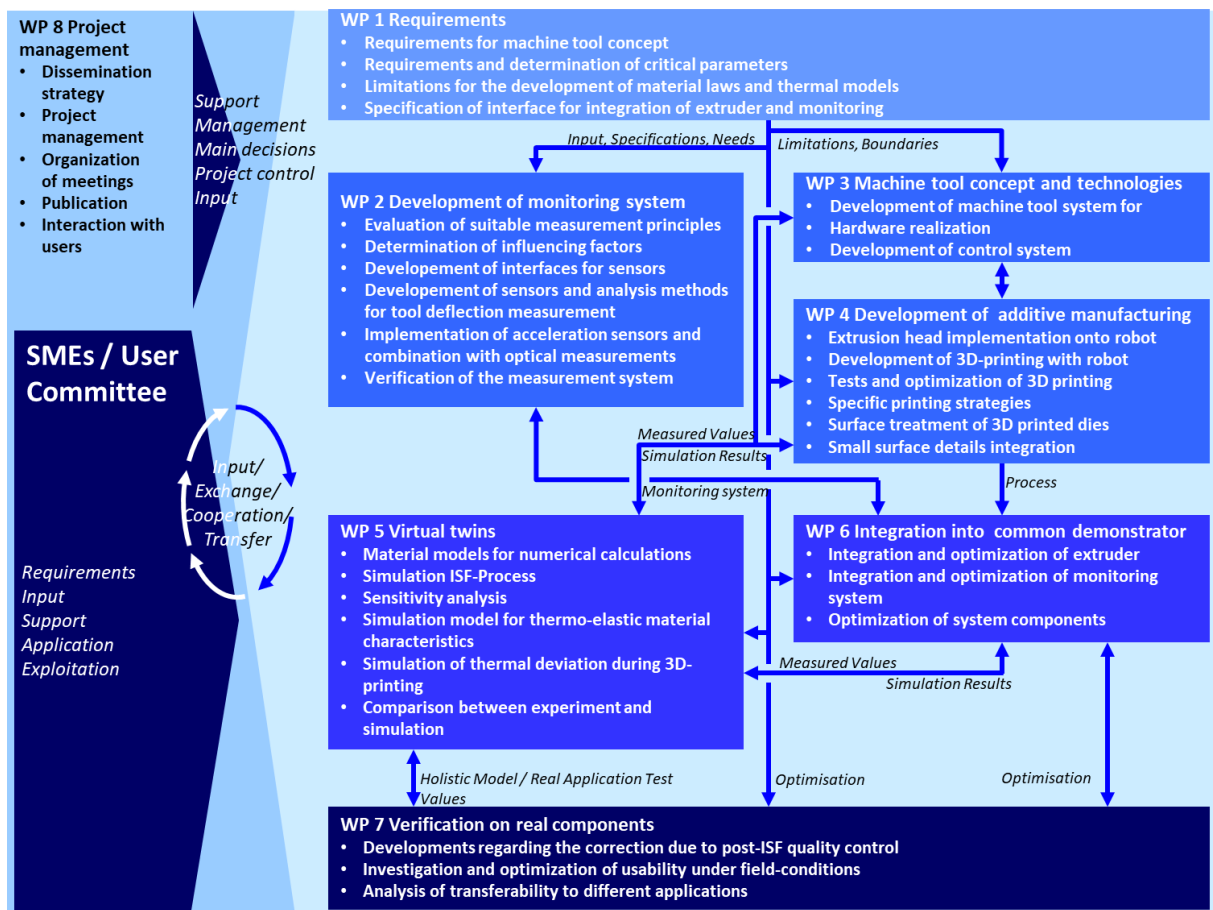


Figure 10: PERT chart of RapidSheet

## 6 Cooperation of the Project Partners and Project Execution

The cooperation between the involved research performers was necessary to reach the project goals, since it brought together the required expertise in various fields. This built up a level of knowledge which could not be obtained by a single partner or by several partners working in parallel. The project consortium partners each had specific and necessary tasks to fulfil. However, in the following, the expertise and tasks of the partners are briefly described.

 Deutsche Forschungsvereinigung für Meß-, Regelungs- und Systemtechnik e.V.	<p>DFMRS cooperated with companies in the German tool and materials industry as well as with the metrology industry. As the central interface between industry and science, DFMRS planned and implemented the joint R&amp;D project. The DFMRS was the leader of the project. In addition, it focused on the dissemination and exploitation by SMEs and the integration of industrial requirements into the project.</p>
	<p>MPC was involved in the literature evaluation of possible machine tool components suitable for the envisioned combination of AM and ISF. It was also responsible for activity coordination from the Polish side. Promotion activities and dissemination of results within the manufacturing companies were also carried out by MPC.</p>
	<p>SIRRIS is the collective center of the Belgian technological industry. SIRRIS applied its know-how in the field of advanced manufacturing development like AM of polymeric, ceramic and metal parts. Research within this project is focused on the integration of AM capability for innovative counter tool forming into ISF technology</p>
	<p>BIMAQ contributed to the research project by its expertise in geometrical measurement applications, with a focus on the in-process monitoring of the tool deflections in the high-load ISF-process. This enhanced the achievable final part quality and the reliability of the manufacturing process itself.</p>
	<p>In RapidSheet, Fraunhofer IWU was responsible for the development of the resource-efficient forming process and the concept of the stylus path, the necessary path generation, the selection of the process parameters and the corresponding experiments. In order to maximize the relevance for industrial applications, Fraunhofer IWU was in close contact with the research partners.</p>
	<p>AGH was primarily responsible for the development of the digital shadow of the developed SPIF technology. The goal was to investigate both sheet material behaviour and counter tool material behaviour under loading conditions. AGH was responsible for running a series of numerical simulations with various process assumptions.</p>

## 7 Introduction to the Work Program

### 7.1 WP1: Analysis of requirements for machine tool concept for combined AM and ISF

#### Requirements regarding integration of the machine tool concept

To come a step closer to accelerating and automating the incremental forming process, a combination of counter tool production and the actual incremental forming process on a portal machine from Haase is planned as the basic design, which will then be gradually upgraded in the course of the project for a hybrid 3D printing-ISF process. So that the process variables (maximum forming force, tool deviation, printing duration, compressive strength, manufacturing accuracy, ...) can be optimally designed in advance, simulation-based investigations into the structural-mechanical properties of the gantry machine were carried out using the Ansys software package. When selecting the machine, attention was paid to a simple geometry and a large working area to be able to produce large-area counter tools with a high degree of counter tool flexibility. In addition to the material model and workspace size, the boundary conditions, which were set opposite at the Tool Center Point (TCP), are also drawn. As a simple demonstrator part for the 3D printing process, the geometric dimension of a truncated pyramid placed in the center of the workspace was selected to act as the opposing force in the incremental forming process for the structural mechanics simulation. A value up to a maximum of 2,000 N at the effective point was specified as the forming force. This corresponds to the force that must be applied by the gantry machine during forming and that the printed counter punch must be able to withstand.

A variety of factors can influence the properties of the additively manufactured tool in 3D printing. For example, the software required for production and the process parameters defined via it (nozzle temperature, filling factor, layer thickness, etc.), the material used and the environment can all have an influence on the objects. In initial experimental investigations, the influence of the above-mentioned factors on selected target variables was investigated fundamentally. 100 samples and scientifically substantiated by methods of statistical experimental design. The focus was on the investigation of the process parameters nozzle temperature, filling factor, wall thickness, layer thickness and printing speed defined by means of so-called slicing software. The production time, component mass, component dimensions and, above all, mechanical properties were defined as target parameters. The latter were determined by means of tensile, compression and flexure tests. To determine the optimum counter tool temperature in terms of good properties and high part quality, three temperature levels were investigated (215°C, 225°C and 235°C) and the results compared. For the investigation of the remaining four selected process parameters and their evaluation, the means of statistical experimental design were used. Two stages of each process parameter were tested by means of a partial factorial experimental design and evaluated with the aid of effect and interaction diagrams. Based on these results, the settings of 215°C counter tool temperature, 1.6mm wall thickness, 0.1mm film thickness, and 70 mm/s printing speed are generally recommended for test specimens made of the modified Tough PLA grade with respect to good mechanical properties. However, depending on the specimen shape and loading type, adjustments may be necessary for high part quality. Based on the study of 20%, 60% and 100% filled specimens, a strong linear relationship can be concluded between the target variables (except for the part dimensions) and the filling factor. In a comparison of Tough PLA, ABS and nylon samples, which were manufactured with the same settings except for material-specific adjustments, parts made of Tough PLA exhibit the highest moduli and strengths under tensile and bending loads

in this investigation. Only under compressive loading does the use of ABS lead to higher characteristic values. Water storage of Tough PLA, ABS and nylon parts to investigate the influence of moisture on the properties of the additively manufactured specimens results in either a decrease or an increase in the mechanical properties determined, depending on the material.

values compared to the "dry" state. When using nylon, it is important to note the strong tendency of the filament to absorb water from the environment, which requires special handling of the material. Apart from individual deviations, a good reproducibility of the results can be assumed due to small standard deviations in the measurements.

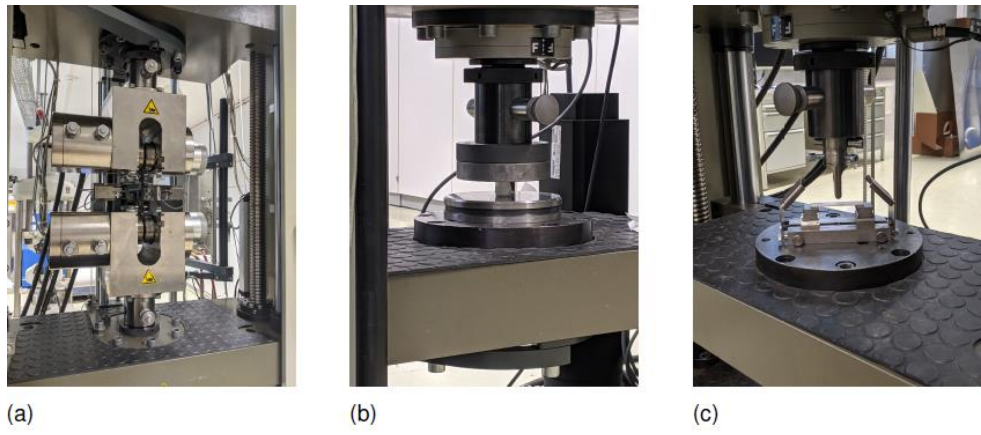


**Figure 11:** Component test rig: (a) tensile test, (b) compression test, and (c) flexure test.

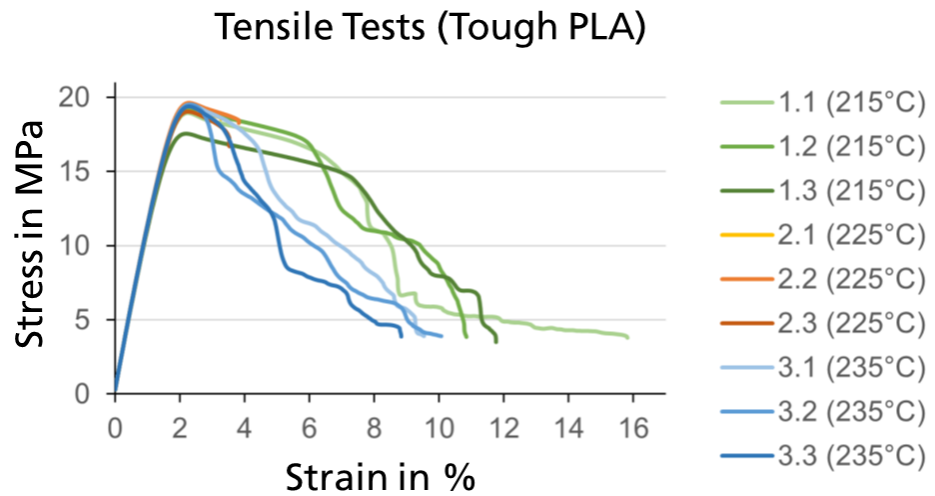


**Figure 12:** Exemplary stress-strain diagram of the tensile tests (section 1).

## **Analysis of technical requirements and determination of critical to quality parameters for AM technology for forming counter tool and ISF-process**

When developing a CNC-controlled machine for 3D printing counter tools for Incremental Sheet Metal Forming (ISF), it's important to consider the technical requirements and critical-to-quality (CTQ) parameters:

- Material Selection:
  - The 3D printing material should have good mechanical properties, such as high strength, hardness, and wear resistance.
  - It should also have good thermal stability to withstand the heat generated during the ISF process.
  - Common materials for this application include ABS, PLA, fibre-reinforced PLA (ToughPLA).
- Dimensional Accuracy:
  - The 3D-printed counter tools need to have precise dimensions and geometry to ensure accurate and consistent forming of the sheet metal. Accuracies in the range of 0.1..0.5mm shall be possible.
  - The mentioned accuracy requirement must also be taken into consideration regarding the resolution and accuracy of the CNC-controlled machine, as well as the capabilities of the 3D printing process itself.
  - Minimize factors like shrinkage, warping, and distortion during the printing process.
- Surface Finish:
  - The surface finish of the 3D-printed counter tools is critical to ensure smooth and uniform contact with the sheet metal. Printing of curved 3d-shaped layer instead of the commonly used layer-by-layer-printing (2.5D) must be taken into consideration as appropriate technology
  - Aim for a high-quality surface finish to minimize the risk of defects and improve the overall forming process.
  - Optimize the printing parameters and consider post-processing techniques like polishing or machining if necessary.
- Tool Durability:
  - The 3D-printed counter tools should be durable and resistant to wear over multiple forming cycles.
  - Evaluate the mechanical properties of the chosen material to ensure it can withstand the forces exerted during the ISF process.
  - Consider reinforcement techniques like adding inserts or reinforcements to critical areas of the tool.
- Design for Tool Integration:
  - Ensure the 3D-printed counter tools can be securely integrated into the CNC-controlled machine for precise positioning and movement.
  - Design the tool with suitable features (e.g., mounting holes, clamps) to facilitate easy installation and alignment.
  - Consider compatibility with the CNC machine's software and control system for seamless operation.
- Validation and Testing:
  - Establish a rigorous testing procedure to validate the performance and quality of the 3D-printed counter tools.

- Conduct dimensional verification, surface inspection, and functional testing using representative ISF processes.
- Monitor key parameters such as tool wear, accuracy, and repeatability, and iterate the design and manufacturing process as needed.

### **Analysis of boundary conditions for the development of material laws for the ISF-process and thermal models for AM**

To develop digital twins of the additive manufacturing and single-point incremental forming simulations, the respective boundary conditions were designed. The geometries of the sheet test pieces, along with the concept of the support counter tool-shapes, were determined first. It was assumed that the simulations based on the three major shapes of the supporting counter tools: pyramid, triangular and rectangular ones that are going to be investigated at Siris and IWU would be the basis of the work plan. The numerical model replicating a SPIF setup under development at the AGH was also designed. Besides that, three different approaches to considering the support counter tool material models were defined. The first is the classical assumption of a non-deformable tool (rigid counter tool mode). The second concept assumes deformable counter tool material with elastic properties. Finally, the possibility of developing a numerical model of the counter tool replicating its morphology related to specific character of 3D printing was evaluated. Polylactic acid (PLA) will be used in the fused filament fabrication 3D printing process. The Abaqus/Explicit solver without mass scaling was proposed for the investigation to maintain high-quality results and eliminate any possible unphysical artefacts. This type of simulation should then be the benchmark during the selection of the mass scaling coefficient used to speed up the simulations. The shell elements with a single Gaussian integration point (S4R) were recommended during the analysis. Selection of several finite elements should be made based on sensitivity analysis of the finite element mesh to the quality of the obtained results.

### **Specification of common generic interface for integration of developed extruder system of Sirris and monitoring methods of BIMAQ**

To monitor the tool deflection independently of the machine kinematics during the forming process, an optical measuring system positioned outside the machine is required. At common feed rates of 50 mm/s [42], a measurement rate of 50 Hz is required to obtain a new measurement point every 1 mm of tool movement. To keep motion blur sufficiently low, the duration of a measurement should not exceed 300  $\mu$ s, which is why the measurement must be performed in a single shot. The required measuring range is given by the machining volume of the machine tool with  $2 \text{ m} \times 1 \text{ m} \times 0.2 \text{ m}$ . In this range, the measurement uncertainty should be less than 50  $\mu\text{m}$ , to enable the detection of typically occurring tool deflections of 150  $\mu\text{m}$  – 450  $\mu\text{m}$  [43]. To cover the required measuring range with single measurements, the concept of a multi-sensor system with camera-based sensors is chosen.

For the integration of the sensor into the machine tool, the assembly on a frame is suitable. The data processing of the measurement system should be implemented in Python, since the software does not require a license. Since the central storage of image data of many sensors is not feasible with the required measurement rate, a system for decentral data processing is used. For each camera, an embedded PC is used to preprocess the image data, whereby the

amount of data to be further processed is greatly reduced. The data is transferred to a central PC via Ethernet, where the data of all sensors is fused and the tool tip position is calculated. As a reference estimate for the tool position, draw-wire sensors are used which measure the position of the axes of the machine tool. The data from the draw-wire sensors is read out via a serial interface synchronously with the camera trigger. The measured tool tip positions must be saved in an accessible file to enable further processing.

For the integration of the pellet extruder multiple techniques can be implemented. The extruder itself should be connected to its power source, as well as to various control signals permitting to control the torque and speed of the servomotor. Sirris chose to work using a STEP/DIR paradigm, but other methods such as PWM and UART can be used, depending on the chosen motor hardware. To generate those signals, Sirris used a microcontroller running a barebone implementation of a square wave output generator. This microcontroller also requires a speed input to generate those signals, which can be either analog or digital. If no complex additional functions are required to be done on said microcontroller, this implementation would be better suited to run on an FPGA.

## 7.2 WP2: Development of system for deflection monitoring and compensation

### Measurement concept

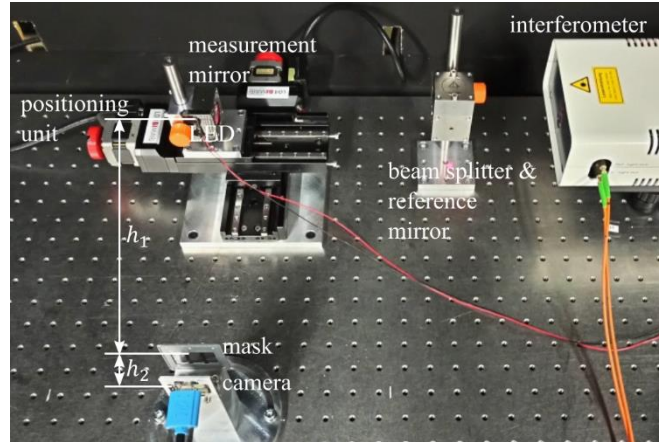
As stated in WP 1, a camera-based multi-sensor system is proposed for measuring the larger deflections of the forming tool. However, since the tool tip represents only a small point in the field of view of a camera-based sensor, a shadow-imaging measurement principle is suitable. Here, an LED is attached to the tool tip, which casts a shadow on a camera chip through a mask with transparent and non-transparent portions. The position of the LED can be determined from the shadow position on the camera chip, which can be evaluated in captured images. The advantage of the shadow-imaging principle is that the information content in the image is increased and thus the measurement uncertainty is reduced. A sufficiently large axial measuring distance can be realized for each sensor, so that several sensors can cover the required measuring volume from a frame outside the machine tool. Since only one LED has to be fixed to the tool and non-moving sensors are installed, no additional safety precautions have to be taken.

Smaller deflections with higher frequencies can be detected by means of acceleration sensors. Capacitive, piezoelectric and piezoresistive sensors are widely used. The accelerometer must be as small as possible for mounting on the forming tool, which is why capacitive MEMS accelerometers are particularly well suited. The IIS3DWB vibration sensor is only 2.5 mm × 3.0 mm × 0.83 mm and measures accelerations up to 6 kHz, covering the expected frequency range of 2 kHz to 5 kHz [44].

### Single shadow imaging sensor

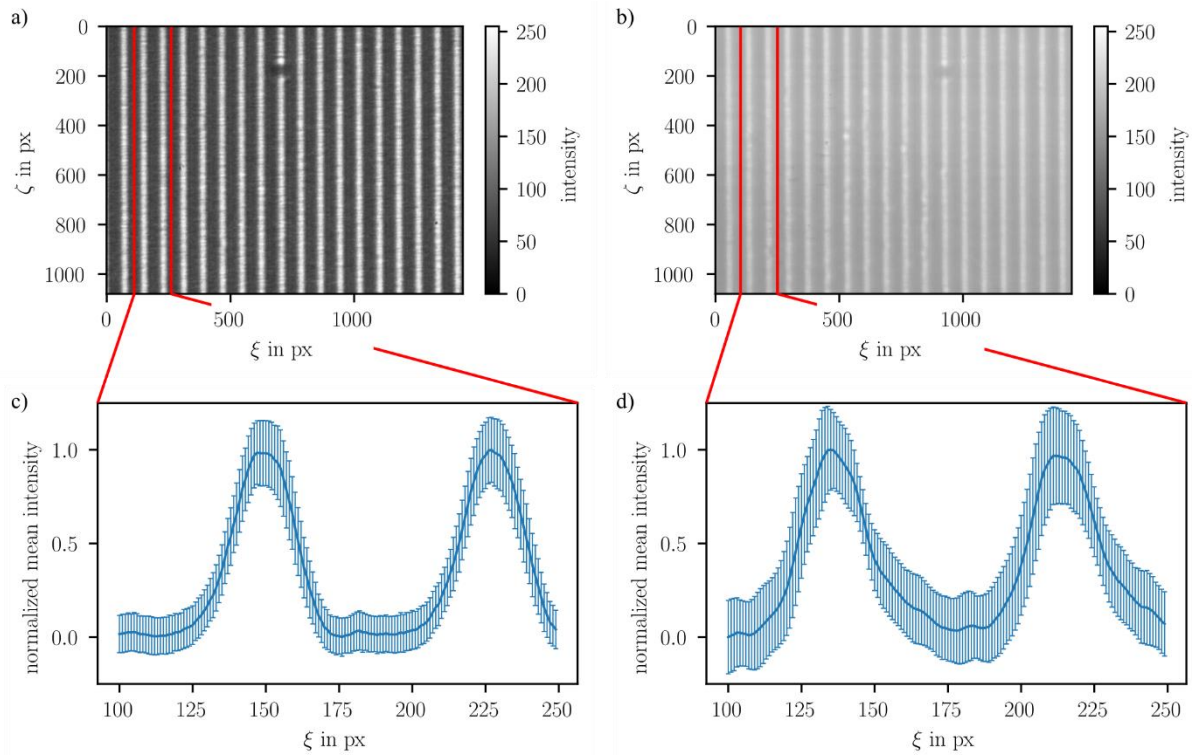
To determine the achievable measurement uncertainty of the optical measurement system and the effect of influencing factors like ambient light, experimental and simulative investigations have been conducted. For investigating the optimally achievable measurement uncertainty of a single shadow imaging sensor and its sensitivity to ambient light, a mask with a vertical

grating with aperiodic contents was used. To evaluate the shadow position in camera images, image processing algorithms based on phase evaluation, correlation and approximating a model function were tested on simulated images, first. The results showed that the model approximation provides the lowest random and systematic error. The simulation results were validated using the experimental setup shown in Figure 13, where an LED is shifted stepwise parallel to the sensor. The mask of the sensor is placed in a groove 20 mm in front of the camera.

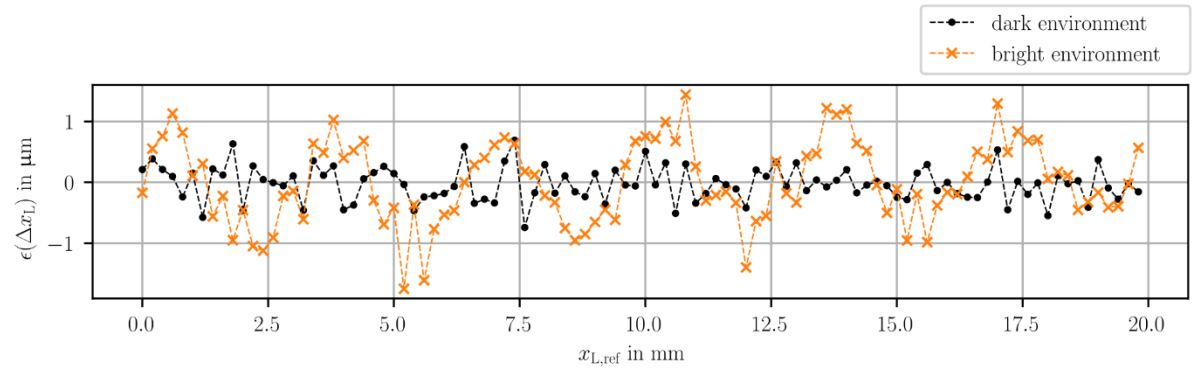


**Figure 13: Experimental setup to experimentally investigate the shadow position evaluation**

To investigate the influence of ambient light, the experiment was conducted in a dark environment and in an environment with an illuminance of 200 lux. The captured images presented in Figure 14 show a lower contrast-to-noise ratio (CNR) in the brighter environment. Simulated images prove, that the increased CNR leads to a higher random error in the evaluated shadow positions. Additionally, the experiment revealed a periodic behavior of the deviation  $\epsilon(\Delta x_L)$  of the LED shift measured by the sensor from the reference LED shift which is shown in Figure 15. The periodic behavior of the shadow shift deviation might occur because the ambient light casts an additional shadow onto the camera which interferes with the shadow cast by the LED. However, the error of the LED position that results from the shadow position error due to ambient light is below 2  $\mu\text{m}$  and therefore acceptable. Anyway, the effect of ambient light can be reduced by using a housing around the sensor, a bandpass filter between camera chip and mask or a brighter LED.

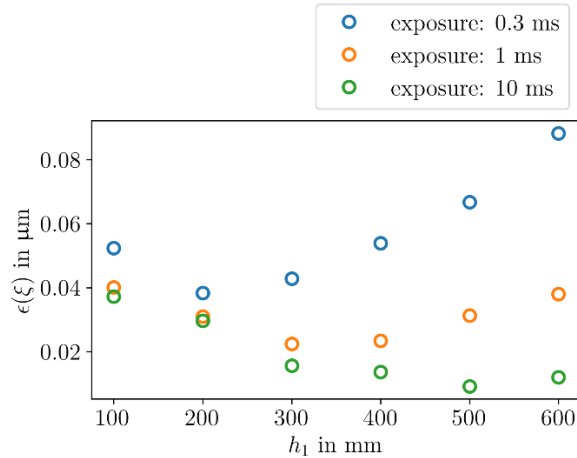


**Figure 14:** Camera images captured a) in dark environment; b) in bright environment. Section of the column-wise normalized averaged intensities wherein the standard deviations of the normalized column intensity are given as errorbars: c) in dark environment; d) in bright environment.



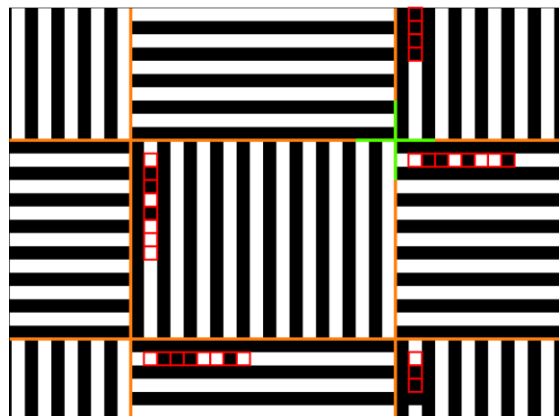
**Figure 15:** Deviation  $\epsilon(\Delta x_L)$  of the LED shift measured by the sensor from the reference LED shift for both illumination conditions.

In addition to ambient light and the LED intensity, the exposure time and the distance between sensor and LED affects the quality of the images. The standard deviation of the evaluated shadow positions in 50 images is shown in Figure 16 for various axial distances  $h_1$  and various exposure times. As expected, the deviations increase with decreasing exposure times but for longer exposure times, the minimum deviation occurs at farther distances. Due to the extension of the LED, the stripes in the image are less sharp the smaller the distance to the LED is which might be the reason for this effect.



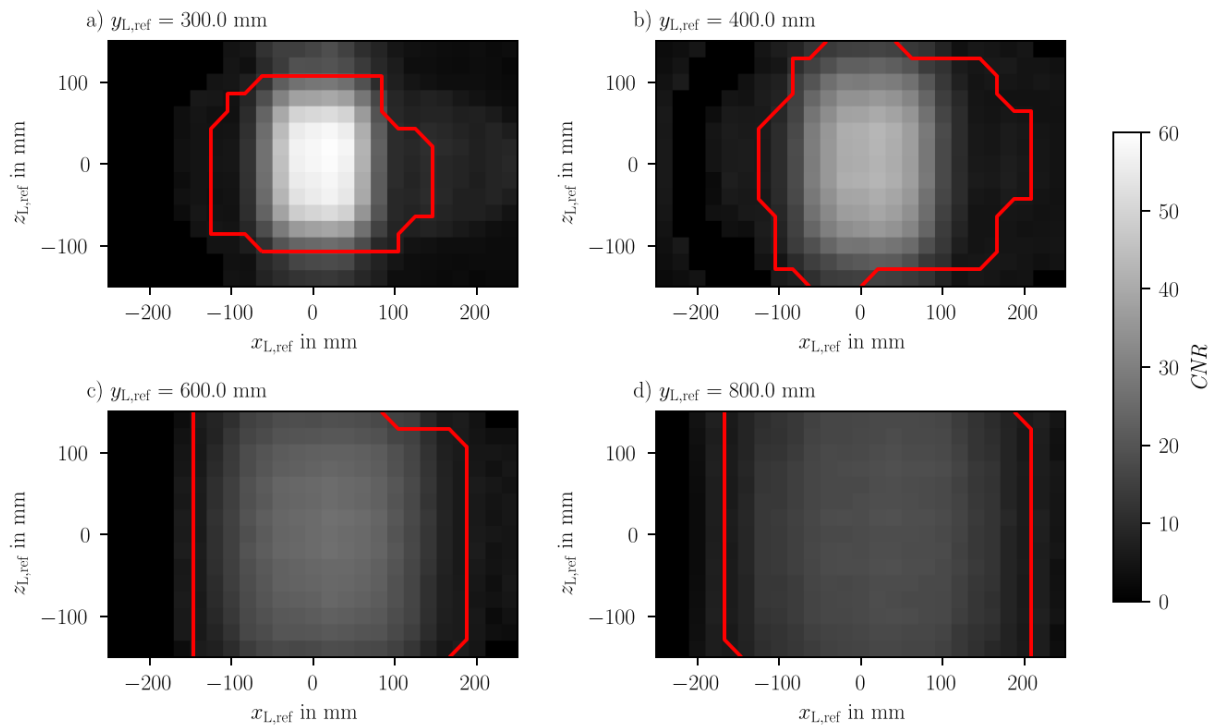
**Figure 16:** Standard deviation  $\epsilon(\xi)$  of the shadow position for various axial distances  $h_1$  between sensor and LED and various exposure times.

To enable an absolute three-dimensional LED position measurement, the mask shown in Figure 17 was developed. The mask contains alternately arranged grids with vertical and horizontal orientation. In each grid, the first transparent stripe contains a binary coding for absolute position measurement. To evaluate the shadow images, the different grids must be segmented first. In a second step, the stripes in each grid are localized. Then, the index is read in the binary coded stripe. Finally, the position of the shadow of the mask center is calculated.



**Figure 17:** Section of the mask used in the shadow imaging sensors. The mask is the black and white structure. The red squares visualize the binary coding. The center of the entire mask is marked by the green cross.

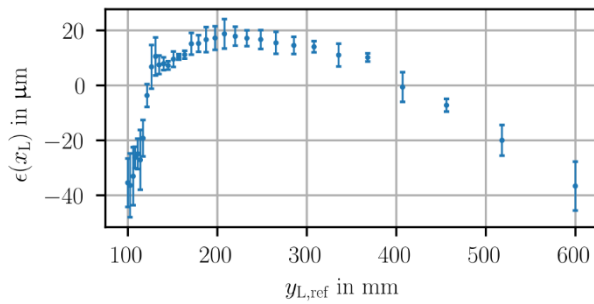
Using the mask with two-dimensional features, the three-dimensional measurement range of a sensor was examined. The measurement range is limited by the quality of the images which is mainly described by the relation between image contrast and noise, the contrast-to-noise ratio (CNR). In addition, at large angles of view, the intensity profile of the stripes changes so that the stripes cannot be detected and an evaluation of the shadow position is not possible. The resulting CNR and the identified boundaries of the lateral measurement range are given in Figure 18 for different axial distances ranging from 300 mm to 800 mm. It stands out that the measurement range of each sensor is primarily limited by the CNR of the images. Since the angle of incidence is the dominant effect, a larger lateral measurement range is covered at larger axial distances. In total, a lateral measurement range in horizontal and vertical direction of 200 mm and larger is reached and an axial measurement range of 500 mm was proven.



**Figure 18: Contrast-to-noise ratios depending on the LED position. The red lines show the boundaries within which shadow positions are evaluated. The graphs contain results for planes at a)  $y_{L,\text{ref}} = 300$  mm, b)  $y_{L,\text{ref}} = 400$  mm, c)  $y_{L,\text{ref}} = 600$  mm, d)  $y_{L,\text{ref}} = 800$  mm.**

To quantify the measurement uncertainty of the LED position, the lateral and axial position component must be calculated. Using a single shadow imaging sensor, the axial position is obtained from the magnification of the features in the mask to the features in the image plane. The lateral position measurement is based on evaluating the position of the shadow of the mask center in the image. To determine the mainly lateral position coordinate  $x_L$  of the LED, the mainly axial position coordinate  $y_L$  was assumed to be known in this investigation and vice versa.

The shadow imaging sensor was investigated in a two-dimensional measurement area using a coordinate measuring machine (CMM) as reference system. The CMM moves the LED, whose power supply is realized by batteries. In theory, each shadow position is associated to a straight line of LED positions but in the experiment, the LED light was reflected by an object close to the experimental setup which was visible in the evaluated sensor data. For this evaluation, a line was fitted in the LED positions, that correspond to a certain shadow position and the deviations from this line were calculated and averaged for several shadow positions. The results (see Figure 19) show systematic deviations up to 40  $\mu\text{m}$  which indicate the reflections. These systematic deviations should be prevented or alternatively either be captured during a calibration enabling a compensation or eliminated by using polarized light.



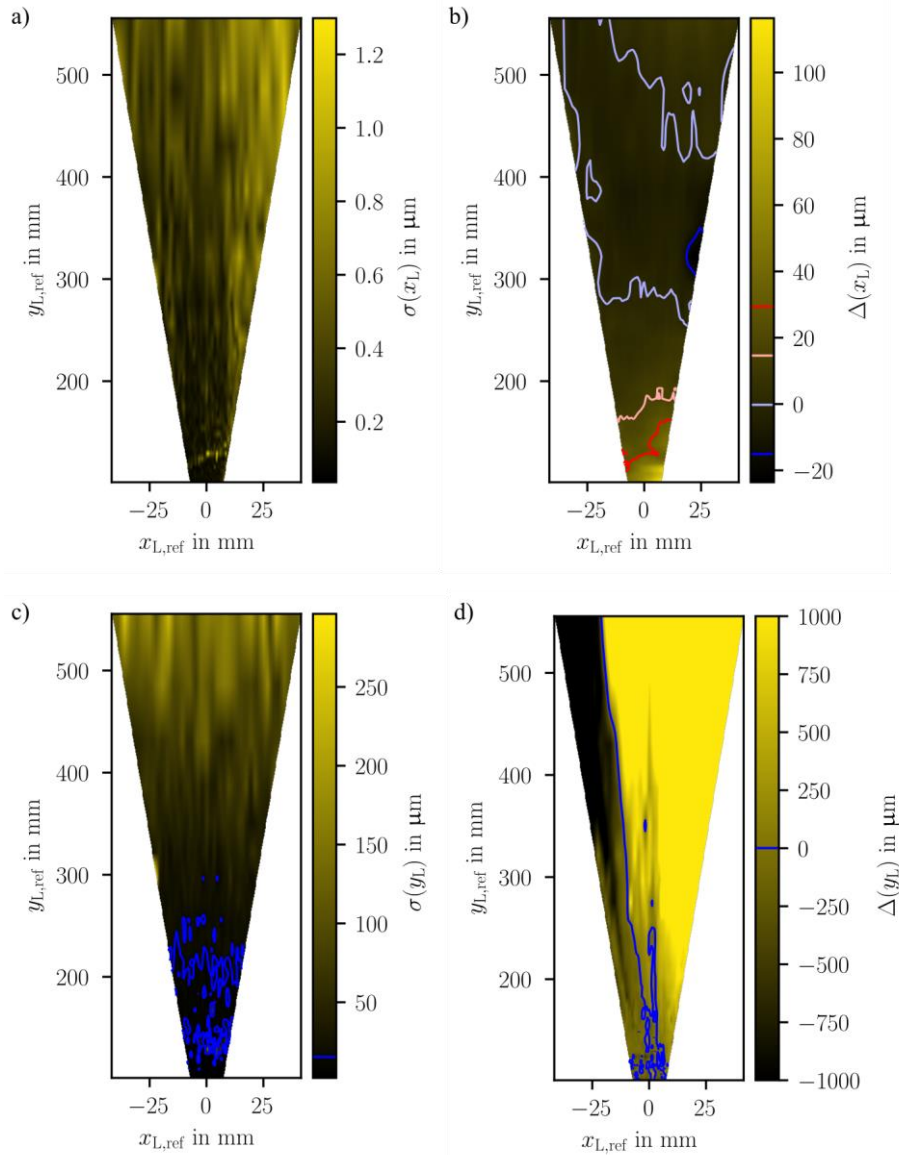


**Figure 20: Error of the evaluated LED position.** a) Random position error of the lateral position  $x_L$ ; b) systematic position error of the lateral position  $x_L$ ; c) random position error of the axial position  $y_L$ ; d) systematic position error of the axial position  $y_L$ .

### Multi-sensor system

To overcome the disadvantage that the uncertainty of measuring the axial distance is worse than measuring the lateral position component, the LED position can be calculated by combining two or more sensors as the intersection of straight lines each obtained by one sensor based on the shadow position. For this purpose in a second experiment, two sensors are positioned next to each other with a distance of approx. 150 mm as shown in Figure 21. To combine the data of multiple sensors, each sensor is connected to a Raspberry Pi 4 via USB 3.1 (see Figure 22), to which the captured images are transferred for preprocessing. Image processing algorithms implemented in Python reduce the full image to the location of the stripes in the image or the absolute shadow position. The image processing results are arranged in a string and sent via Ethernet to a central PC using a socket connection with Python.

In both sensors, the shadow position is evaluated, and the LED position is then calculated as the intersection of straight lines resulting from the evaluated shadow positions. Since the systematic error dominates the measurement uncertainty, only the systematic error of the lateral and axial position is shown in Figure 23. In the middle area, the lateral position error is below 15  $\mu\text{m}$  and the axial position error is below 50  $\mu\text{m}$ . To further decrease the axial position error, the intersection angle should be closer to 90° and the angle of incidence of the light ray to the camera should be closer to 0°.

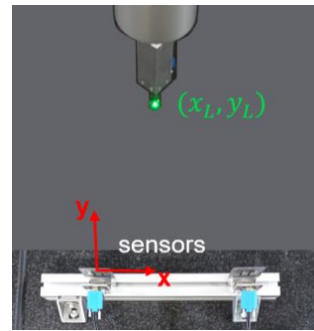


**Figure 21: Experimental setup for uncertainty investigation of two sensors next to each other.**

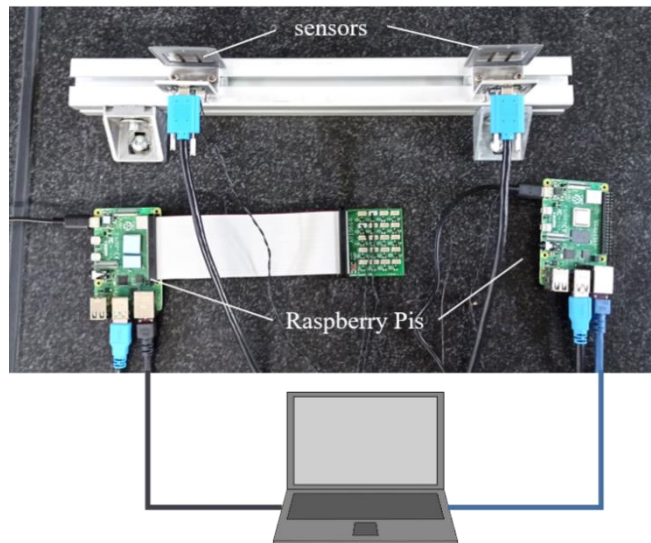


**Figure 22: Sensor setup on a MayTec Profile. The sensors are connected to Embedded PCs (Raspberry Pi 4) via USB 3.1, which are connected to a computer via Ethernet.**

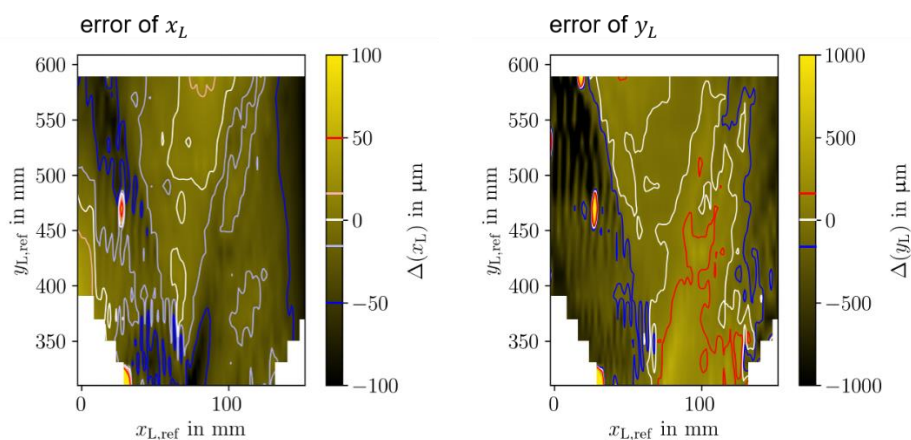


**Figure 23: Systematic error of the evaluated lateral LED position  $x_L$  and axial LED position  $y_L$ .**

To optimize the results of the axial position component, the sensors are arranged perpendicularly in a third experiment. As shown in Figure 24, sensor 2 and sensor 3 are oriented perpendicular to sensor 1. Here, the mask containing two-dimensional features is used and the LED is moved in a three-dimensional measuring volume of 300 mm x 500 mm x 200 mm along the paths given in Figure 24. The results of the evaluated random error for each position component provided Figure 25 show that the angle of view of the laterally measuring sensor is the dominant influence on the random error. Nevertheless, the random error is below 5  $\mu\text{m}$  for all position components ( $x_L, y_L, z_L$ ) at most of the tested LED positions. In contrast to this, the systematic error shown in Figure 26 ranges from -150  $\mu\text{m}$  to +150  $\mu\text{m}$  and dominates the measurement uncertainty. However, the systematic error follows a tendential parabolic course over the angle of view of the laterally measuring sensor which can be compensated. After compensation, a scatter remains that is below 50  $\mu\text{m}$ , and therefore, the required measuring uncertainty is reached inside the required measuring range per sensor.

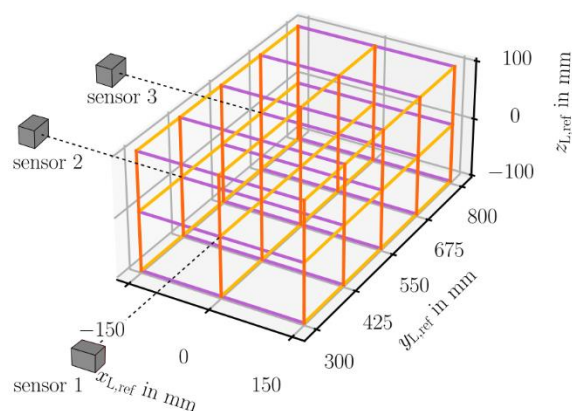


**Figure 24: Schematic setup with perpendicular sensors. The lines are the paths on which the LED is moved to evaluate the measurement uncertainties.**

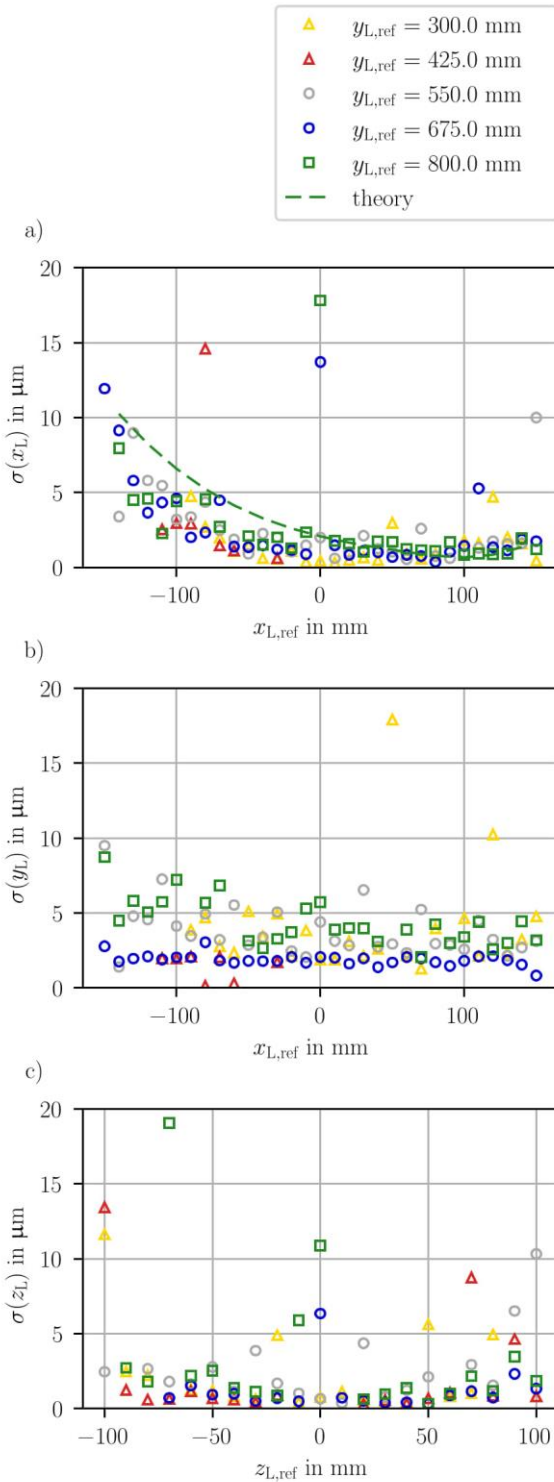


**Figure 25: Random error of the measured LED position for various axial distances  $y_{L,\text{ref}}$  to sensor 1:**  
**a)** Random error of the  $x$ -position vertically centered, **b)** random error of the  $y$ -position vertically centered, **c)** random error of the  $z$ -position horizontally centered in front of sensor 1.

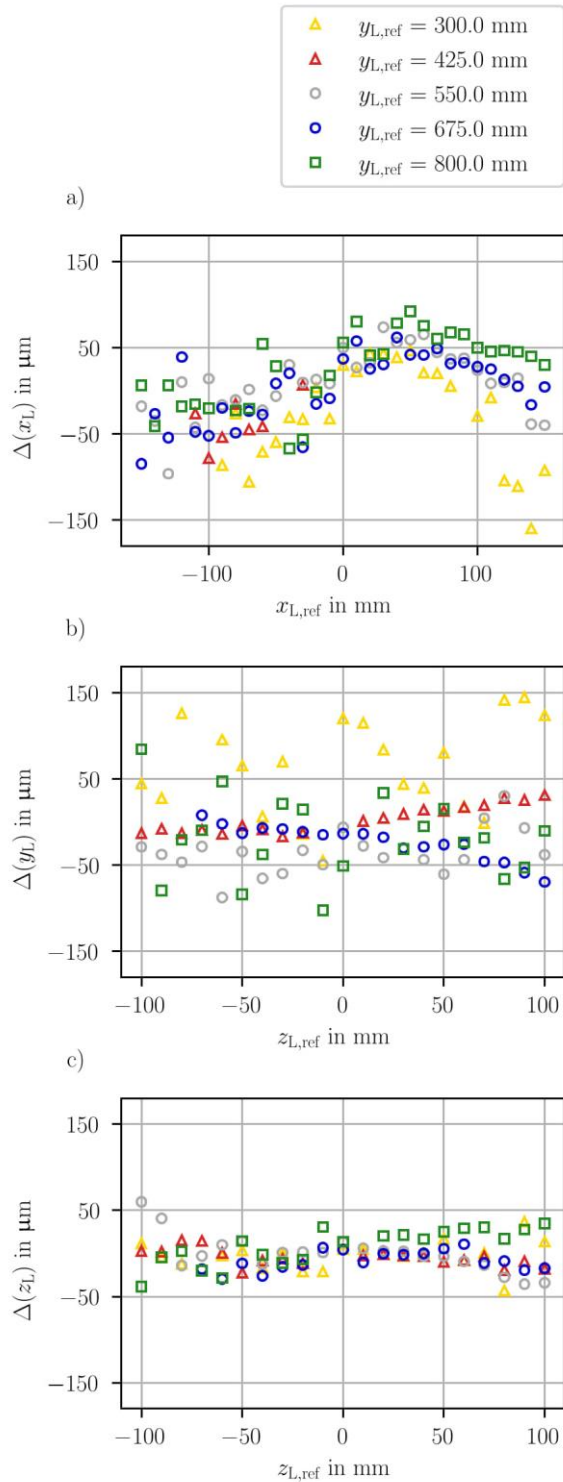


**Figure 26: Systematic error of the measured LED position for various axial distances  $y_{L,\text{ref}}$  to sensor 1:**  
**a)** Systematic error of the  $x$ -position vertically centered, **b)** systematic error of the  $y$ -position horizontally centered in front of sensor 1, **c)** systematic error of the  $z$ -position horizontally centered in front of sensor 1.

## High-frequency measurement

To also capture high-frequent LED movements, an acceleration sensor is attached to the model tool at BIMAQ, see Figure 27. Thereby, the acceleration data is obtained via an SPI interface.

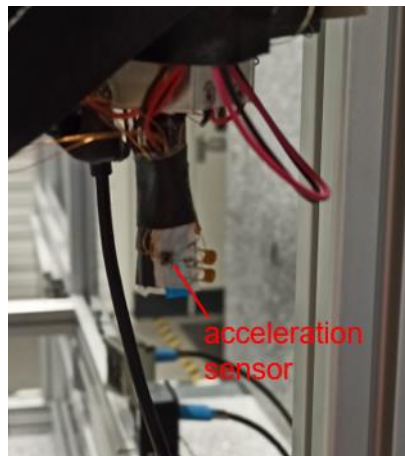


**Figure 27: Acceleration sensor attached to model tool.**

To enable the usage of the acceleration sensor in the ISF process, a wireless measuring concept for the acceleration sensor is developed, which is shown in Figure 28. The accelerometer, a microcontroller and a transceiver are attached to the tool tip. The data recorded by the accelerometer is transferred to a microcontroller. Then, the microcontroller transfers the preprocessed data to a transceiver, which sends the data to another transceiver outside the machine tool wirelessly. The receiving transceiver is connected to a Raspberry Pi 4 which transfers the received data to the central computer.

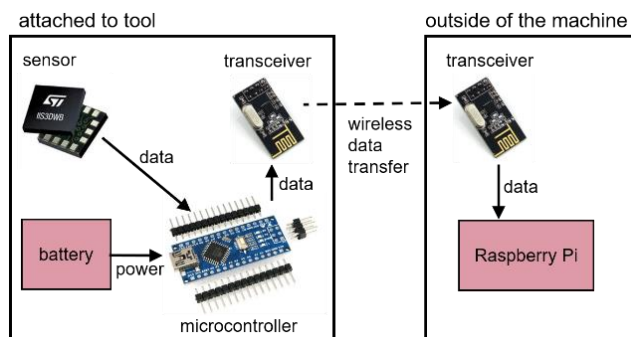


**Figure 28: Wireless acceleration measurement system.**

With the IIS3DWB vibration sensor, the acceleration provided in Figure 29 was captured during one-dimensional stepwise tool movement. Thereby, the acceleration was measured along the axis, in which the tool moved. The acceleration and deceleration between holding positions is clearly detectable by the peaks. The high-frequent scatter between the peaks shows vibrations during the holding positions.

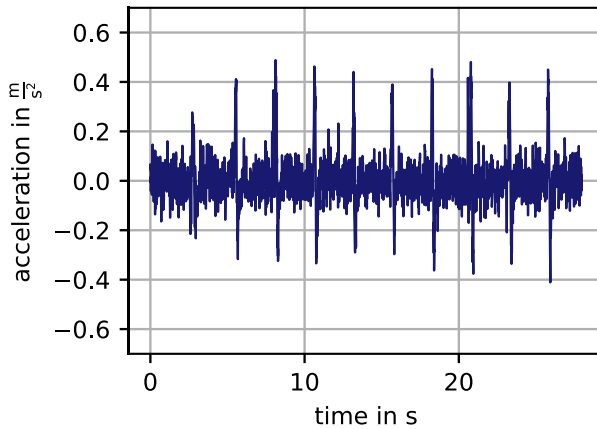


**Figure 29: Acceleration captured during one-dimensional stepwise tool movement. The shown acceleration component is along the moving direction.**

To combine the low and high frequency measurement, the acceleration data measured by the accelerometer is integrated twice to obtain position data. Furthermore, a time synchronization is necessary for combining both systems. The signal sent by one Raspberry Pi to trigger the cameras simultaneously could also be used as a clock-signal to align the signal of the accelerometer in time. The combined position data is finally stored in a txt-file so that the measured positions can be compared to the simulation data and then used to optimize the tool path.

### Integration of monitoring system in machine tool

For the integration of the measurement system in the machine tool, the sensors are mounted on a frame made of MayTec-profiles as in laboratory experiments (see Figure 30). Due to even brighter ambient light on the machine tool at Fraunhofer IWU, where an illuminance of 500 lux was measured, the nominal luminous intensity of the LED should be at least 1000 mcd. A flash LED can be used to further increase the luminous intensity and enable shorter exposure times at a similar CNR. The bright environmental illuminance of 500 lux also requires the use of a 3D-printed housing, which is optional in laboratory experiments. Additionally, it is mandatory, that the tool does not rotate during the forming process, to ensure a constant offset between the LED location at the tool tip and the center of the tool tip. Since the sheets are fixed in a frame and then formed downwards, a tilted sensor setup is suitable so that the tool tip is not hidden by the frame in the sensor's field of view. Using a mask with a vertical grating, it is necessary to know the vertical LED position at each sensor measurement to determine the LED movement. Therefore, it is advantageous to use a mask that contains features in vertical and horizontal direction. Absolute features are advantageous, to enable an absolute position measurement. Thus, no approximate reference position needs to be known after each loss of view.

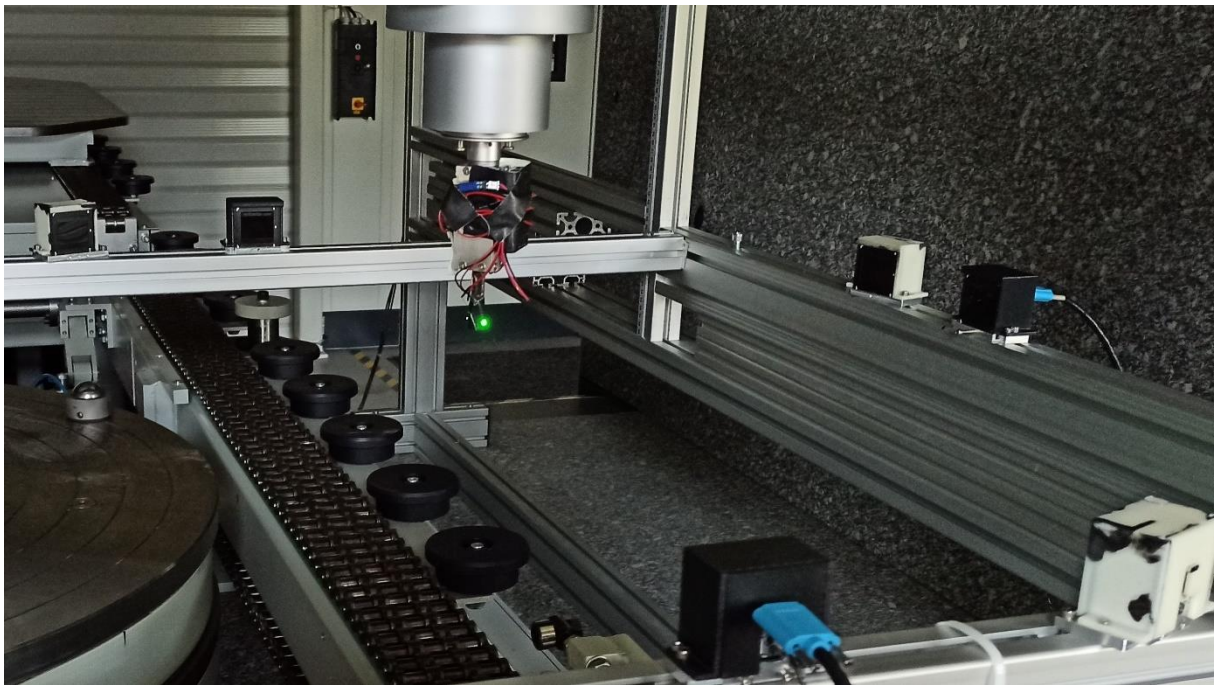


**Figure 30: Experimental setup with multiple sensors at a coordinate measuring machine.**

Another requirement relevant for the sensor integration into the machine tool is the length of wires. Trigger wires and USB wires are applied between the Raspberry Pis and the cameras and must have a length of 3 m. The Ethernet wire between the Raspberry Pis and the central computer must be 5 m long. In the feasibility study of RapidSheet, the draw-wire sensors, that are integrated in the machine tool at Fraunhofer IWU and served as reference system, are read out in the program HTerm as hexadecimal numbers and saved as txt-file.

The measured positions should be saved in a txt-file which is readable by any computer. The list of points can be upsampled or downsampled for a comparison to the tool tip positions determined in the machine tool simulation. This way, the knowledge obtained from the measurement can be used to improve the simulation. The identified x, y and z positions of the forming stylus were used as input data for the finite element simulations in WP5. The coordinates were mapped into the format of the tool path trajectory required by the FE software. As a result, the tool path can be generated in a theoretical way or directly designed based on the experimental measurements. So, the tool path can be optimized based on the combined results of the tool tip measurement and the simulation.

### 7.3 WP3: Development of a machine tool concept and technology for combined AM and ISF

#### Simulation-based modeling of the printed counter tool

In order to be able to simulate the 3D printing process with the ANSYS software package, a simple truncated pyramid is used as a demonstrator workpiece. Figure 31 shows the dimensions of the printing geometry and the base plate on which the 3D printing is built.

Meshing is done by regular subdivision into uniform hexahedra to better account for the layer-by-layer printing process in the simulation. This ensures that only the volume elements within the printed layer are taken into account and that there is no interference from neighboring layers. The height of the volume elements thus corresponds to the individual layer as a process parameter of 3D printing. The base plate can be heated for the 3D printing process, for which corresponding boundary conditions are provided in the model.

For the layer-by-layer application of the material, a motion function was developed according to the G-code path, which is also stored in the 3D printer's control system. In addition, a volume element clustering is carried out, which determines the respective material length per process step. This serves to increase the efficiency of the very computationally intensive simulation. For the pressure settings, the values from the upper table in Figure 31 were initially used in order to shorten the simulation times. In the future, however, the simulations will be used for calculation with the print settings for real 3D printing. In this way, the layer structure can be simulated realistically in the FE model.

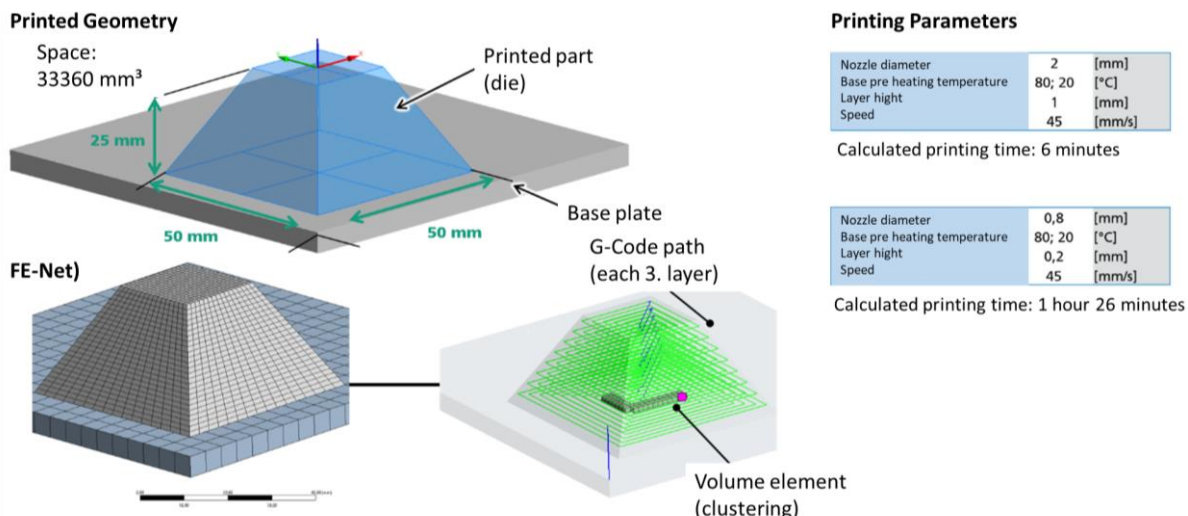


Figure 31: Model setup for thermo-elastic 3D printing simulation

After the simulation model with all its boundary and initial conditions was built for a transient calculation, the first results could be simulated for the simplified pressure settings from the upper table of Figure 31.

The time course of the layer-by-layer material application by the extruder is shown in Figure 32 for selected time  $t_1=230\text{s}$ ,  $t_2=700\text{s}$ , ...,  $t_n=1710\text{s}$ . During the simulation, the printing plate is preheated at  $80^\circ\text{C}$ . At time  $t_1$  of the printing process, the second material layer is being applied. The red colored area shows the material section applied at this time, which has a temperature of about  $160^\circ\text{C}$ . This corresponds to the process temperature in the printing plate. This corresponds to the process temperature in the print nozzle for the filament PLA, a thermoplastic plastic that is used for very many 3D printing applications and is inexpensive to

procure. Most of the injected heat diffuses into the environment of the workspace and only a small part of the heat remains in the print workpiece. Layer by layer, the material is thus applied and the shape of the counter tool takes on its form. At time  $t_5=1265\text{s}$ , one of the last material layers is applied. From the resulting temperature field at time  $t_5$ , it can be deduced that the surface temperature has already cooled significantly to  $20-50^\circ\text{C}$  and only the core of the truncated pyramid has a higher temperature of about  $75^\circ\text{C}$ .

After a time  $t_n=1710\text{s}$ , the printed workpiece has reached the ambient temperature after cooling and has thus also assumed the geometric final state.

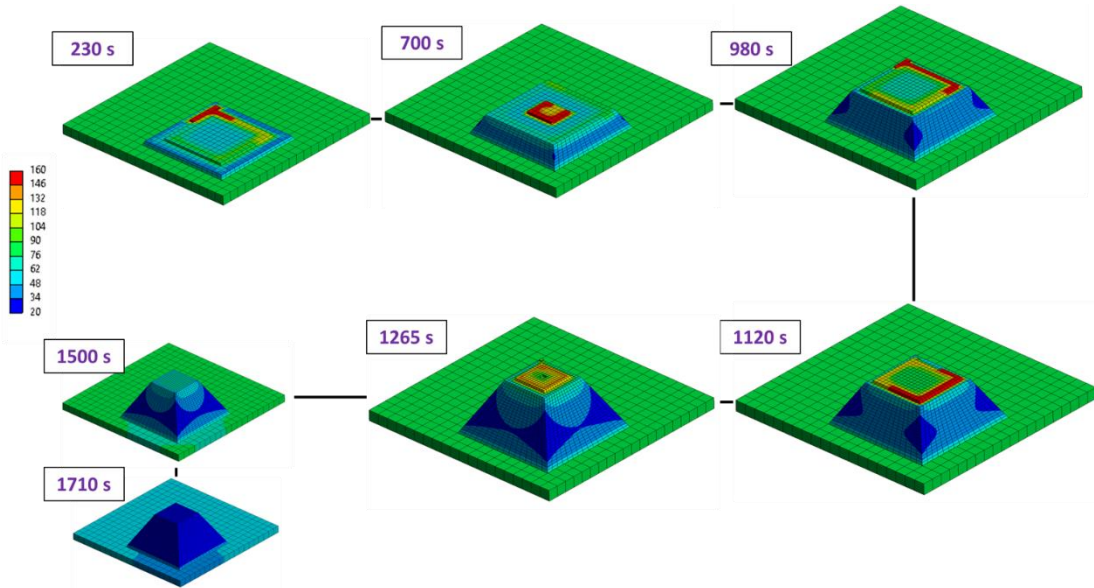


**Figure 32: Result of the simulated layer structure in selected time steps**

A closer look at the workpiece reveals the plastic material behavior during the cooling process. Figure 33 shows the displacement at the center of the workpiece in a displacement-time diagram on the left. For the course in x-, y- and z-direction, it becomes clear for the center point that the material contracts and thus an undesirable shrinkage effect can be seen. For this specimen with a total height of only 25mm, the shrinkage error is up to 0.4mm, which corresponds to about 1.6% compared to the initial value. This rather high value is due to the coefficient of thermal expansion of the plastic, which is  $90 - 120 \mu\text{m/m} \cdot \text{K}$  and thus 10 times higher than for normal steel.

This negative effect must be taken into account in the production of the workpiece and must be taken into account in the parameter settings by means of compensation strategies during the 3D printing process in order to minimize the source of errors.

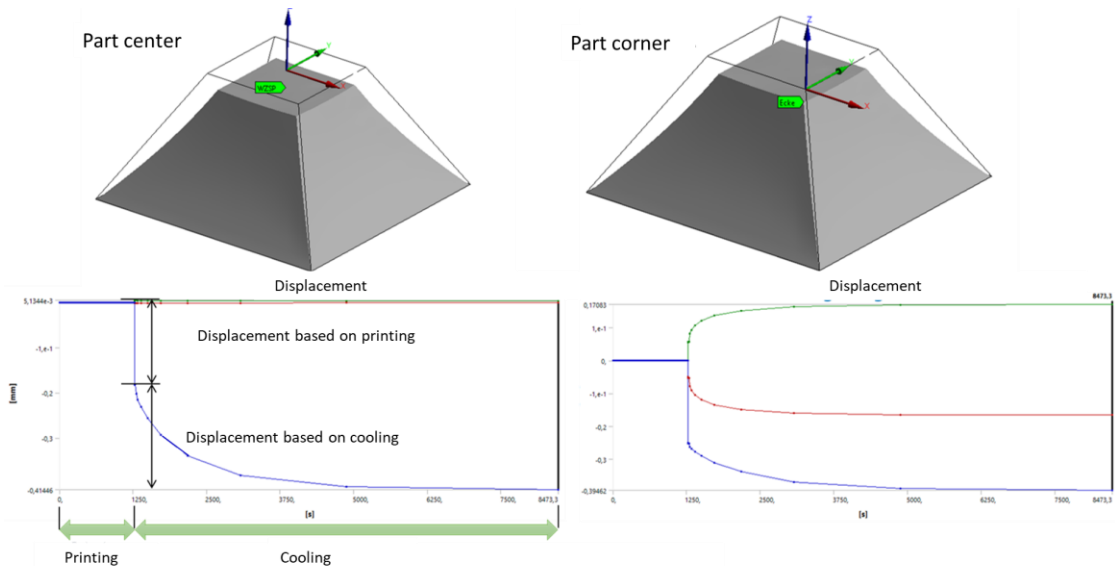


Figure 33: Thermo-plastic shrinkage behavior during the cooling process of the 3D printed part

## Development of individual components for the machine system

### Extruder:

Initially, a commercial filament extruder is to be integrated into the machine system. In later work steps, it is planned to integrate a Pelet extruder (see report of the Belgian partner Sirris) into the machine system. The extruder melts the filament for printing the parts and presses it out at a specified speed. Various parts are installed for this purpose, which will be discussed below.

The extruder consists of various individual components, such as the heating cartridge, the temperature sensor, two fans and the stepper motor. The heating cartridge and the temperature sensor are mounted directly in the counter tool of the extruder in order to control the temperature as precisely as possible. The fans run continuously. One fan cools the extruder and the other cools the output filament. The stepper motor pushes the filament into the counter tool from above to ensure a continuous materialfluss.

The arrangement of the parts described is shown in the following figure.

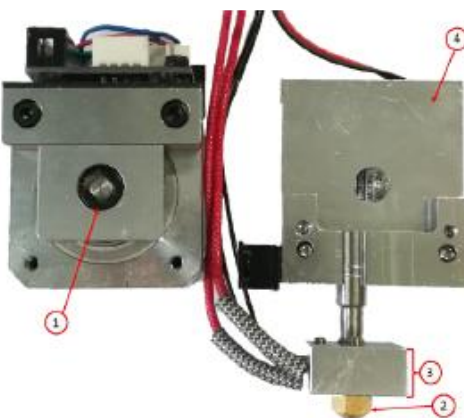


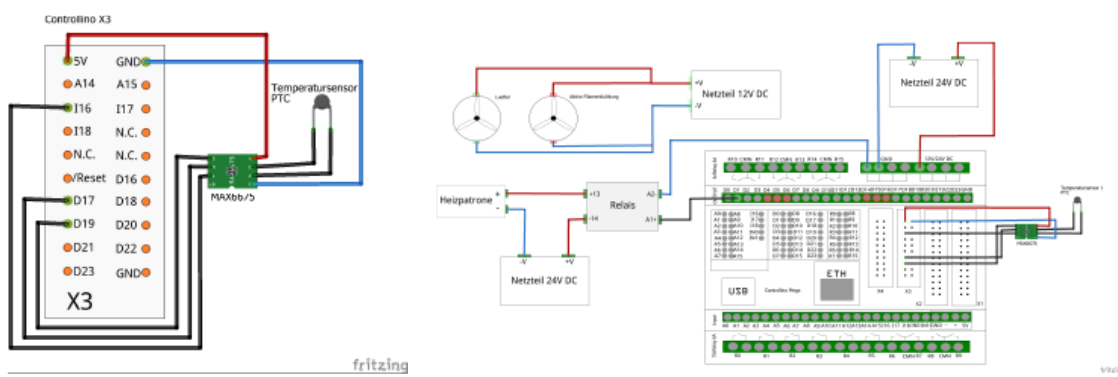
Figure 34: Extruder

The stepper motor with feed wheel is marked with 1. Number 2 shows the nozzle and 3 the forming head with heating cartridge and temperature sensor. Opposite the stepper motor is the heat sink marked 4 and a fan mounted behind it.

### Temperature control

The initially used PLA filament, which is to be used for 3D printing, melts at a temperature of approx. 160 °C. Therefore, quite precise temperature control is necessary. To be able to measure the temperature in the extruder nozzle, a type K temperature sensor was attached to the nozzle. This can be read out with the aid of the Controllino via an adapter. In this case, the MAX6675 controller is used as a signal converter.

The tub pin header X3 of the Controllino is used for the connection. The exact connection diagram can be seen in the following figure.



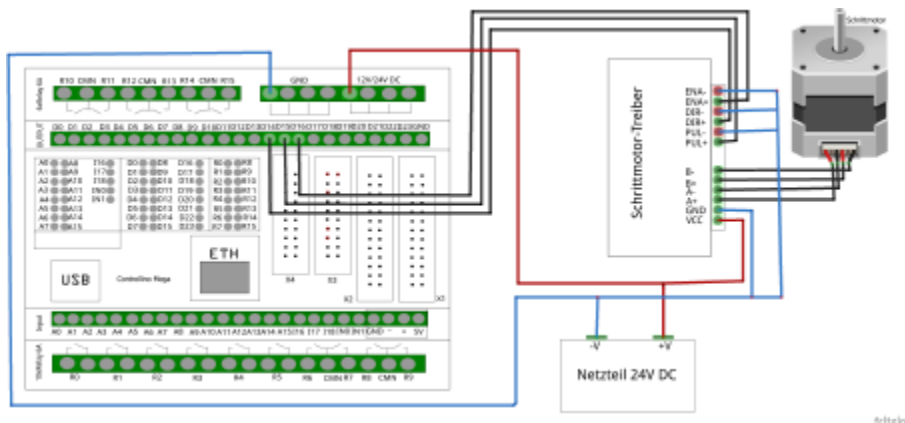


Figure 37: Wiring diagram of the internal stepper motor

### Clamping frame

The sheet to be formed is to be clamped in the clamping frame (Figure 38). The frame is then moved to place the sheet on the forming piece and to form it with the stylus. The frame consists of four side parts to which fastening devices for the sheet metal are attached. In addition, four stepper motors are attached to the frame to keep it parallel and guide it downward. All four stepper motors must therefore work in parallel. The frame is a so-called gantry system. This refers to a motion system in which multiple feed motors move a common axis. Since the motors move in angular synchronism, the gantry drive behaves as if it had only one motor. In this case, four closed-loop stepper motors work on the stenter frame, which are controlled in parallel via the Controllino.

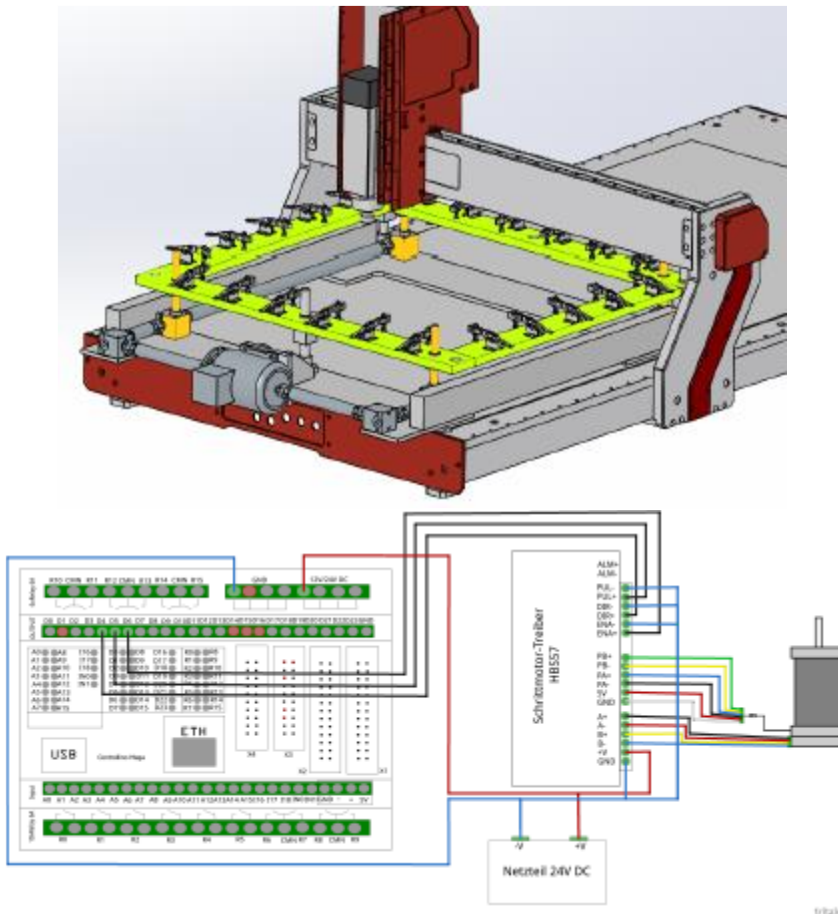


Figure 38: Clamping frame

The clamping frame is marked in green in Figure 38 above. The four stepper motors are shown in orange. The clamping frame could not be built during the practical course, so the following chapters deal with the commissioning of the stepper motors. The external stepper motors have the task of keeping the clamping frame, in which the sheet is clamped, parallel to the substrate and moving it up and down. They are controlled by the same Controllino that was used to control the ex-truder functions. This in turn sends its signals to the HBS57 stepper motor driver, which then transmits them in converted form to the stepper motor. The Controllino can control up to 4 motors. In perspective, these should be able to be moved synchronized via the CNC.

In the previous chapters, the commissioning of the individual components was described in detail. Now these single components are to be combined in a complete system. For this purpose, the hardware of the temperature control and the clamping frame control will first be linked. The circuit diagram of the complete system is shown in the following figure.

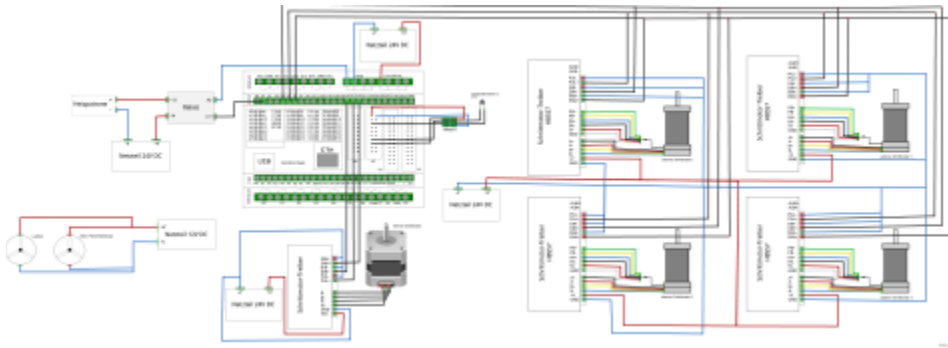


Figure 39: Overall circuit of the clamping frame actuator system

## 7.4 WP4: Development and qualification of AM technology

To enable the printing of large-sized parts, a commercial extruder was utilized and affixed to a 6-axis industrial robot. Specifically, the extruder employed for this purpose is the MDPH2 model manufactured by Massive Dimensions, and it was mounted onto a Staubli TX2-90L robot as showed in Fig.40. However, due to the constraints imposed by the industrial robot's nominal payload capacity of 8 kg, it is unfeasible to install a larger extruder.

After obtaining a 3D model of the intended object, a G-code can be generated using a standard 3D printing slicer. However, since the robot cannot comprehend the G-code directly, a Python post-processor was specifically developed and seamlessly integrated into the RoboDK framework. This enables the translation of the G-code into VAL3, the programming language compatible with our Staubli robot.

RoboDK allows the user to create very dynamic, hardware agnostic programs and quickly post-process them to a chosen robot/tool combination.



Figure 40 : Overall architecture of the robotic printing unit

The functionalities provided by RoboDK allow to post-process complex g-codes rapidly, however, tool synchronization in our case was still nonexistent. The next task was to precisely dispense the correct quantity of material in accordance with the distance covered. It is also essential to differentiate between printing movements and positioning movements as material should not be extruded in the latter case.

To synchronize the robot's feed rate with the extrusion speed, similar to a conventional FDM 3D printer, the solution involves integrating a controller into the system and programming it to correlate these speeds. Industrial robot controllers are not designed to synchronize in real time

with external axes of this nature, so various programming techniques, data transfer methods, and information translation had to be employed to resolve the issue.

The calibration method was based on finding the transfer function between the mass flowrate of extrudate and the motor PWM values. This involves accurately evaluating the amount of extruded material and consequently the length of extruded filament at different extrusion speeds, temperatures, and materials. The process entails extruding for a specific duration at a known motor speed. Precise weighing of the extruded material is then conducted and correlated with the gearbox ratio, motor speed constant and screw's rotation speed. Based on the obtained results from weighing the filament, a material flow rate curve is derived by performing a best-fit analysis of the different measurement points (Figure 41).

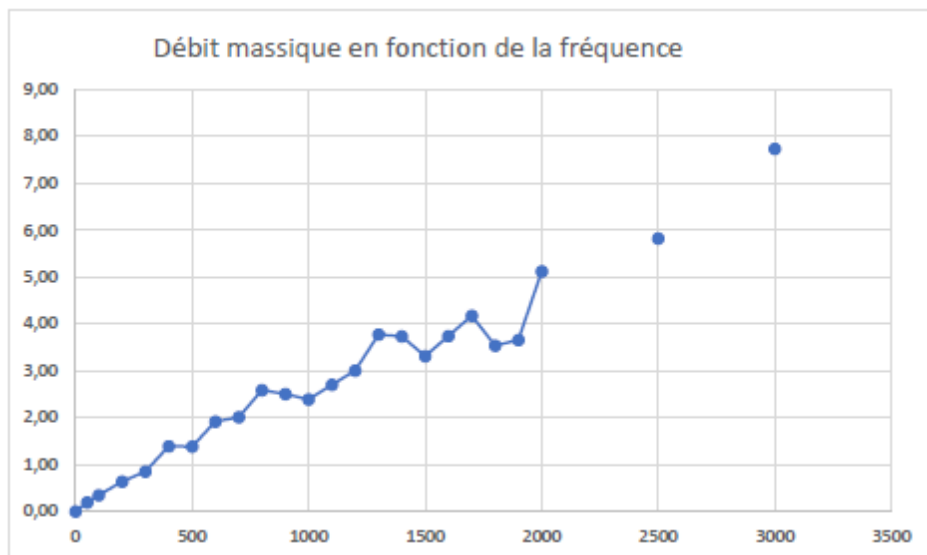


**Figure 41 : Mass flow rate vs frequency**

## Refactoring of the extruder

Major reliability issues were encountered with the mechanical components of the extruder following longer and more intensive printing sessions. It was observed multiple times that the gearbox coming with the extruder, and more precisely the output shaft would not be able to withstand the peak torque of the motor. During the printing process, the gearbox shaft is subjected to significant alternating torque of tens of Nm. These repeated shocks during successive printing steps result in fatigue on the output shaft of the gearbox, eventually leading to failure. This output shaft was replaced several times with different materials before eventually changing the unit (Figure 42).

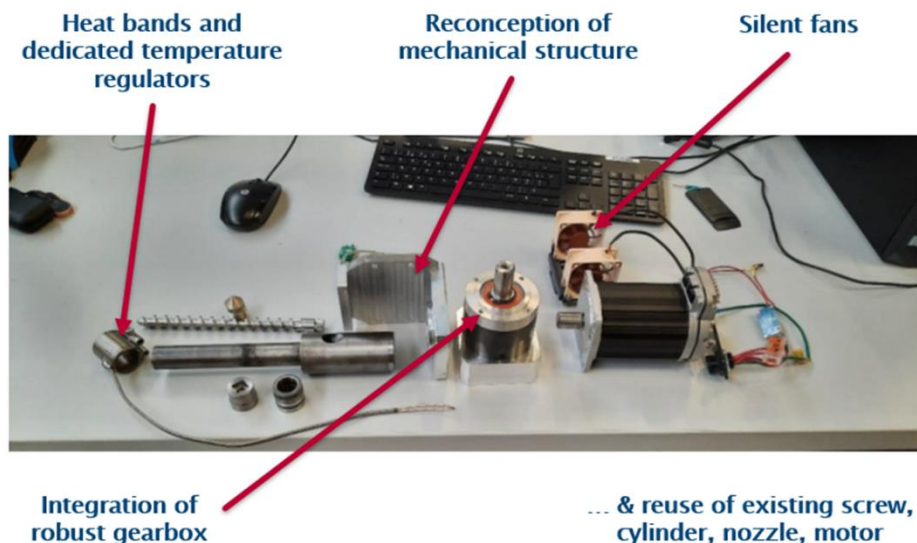


**Figure 42: Extruder components and refactoring**

To address this problem, a new gearbox from Neugart was integrated. It features a larger diameter output shaft and a peak torque capable of withstanding the fatigue induced by repeated shocks. The output shaft diameter was increased from half an inch to 20mm as a result, and some work was required on the gearbox to screw coupling, as well as the mantle of the extruder.

Additionally, it was discovered that the bent sheet metal frame of the extruder was inadequate and easily bent during low intensity work. During the disassembly, it was also noted that there were no mechanical alignment mechanism between the gearbox, motor, and screw. Angular misalignment occurs due to axial misalignment of the different rotating components, which could also explain the breakage of the gearbox output shaft. Therefore, the entire mechanical support chassis was redesigned, optimized to minimize weight, and manufactured using EN AW-7075 aluminum. The final result is much more robust, 500 grams lighter, and significant reductions in extruder's energy consumption and motor heat dissipation were observed. Testing confirmed the elimination of thermal overheating errors or safety torque issues on the extruder motor.

## Development of the control electronics

To execute extrusion commands in coordination with the robot's movements, the robot communicates with a microcontroller that controls the extruder (Figure 43). For the majority of the project, the microcontroller used is an ATMEGA328P, based on an 8-bit architecture that offers limited flexibility for adding more advanced features such as pellet filling management, sensor readings, or sending tracking and diagnostic information to the cloud.



**Figure 43 : Control scheme of the pellet extruder**

The main clock speed of the microcontroller is relatively slow (~20MHz), and the precision of the analog inputs is not great. For the process, we require an analog input sent by the EtherCAT coupler. This input is constantly monitored at a high speed by the system to update the extrusion commands for the robot. The internal clock frequency of the ATMEGA core is 125 kHz, and each analog-to-digital conversion takes approximately 13 clock cycles, resulting in a refresh rate of 104  $\mu$ s for the ADC. The maximum resolution is 10 bits for an output range of 0-5 V, providing a resolution of about 5 mV. Based on this, we can define an error of approximately 0.1% on the requested setpoint. These performance characteristics are sufficient for our application.

It should also be noted that this type of single-core microcontroller excels in performing a single task simultaneously. Adding cloud connectivity, sensors, or servos would significantly impair the loop for reading and transcribing the setpoint. To enhance the electronics and enable task parallelization, a transition to an STM32H7 core has been initiated and will be continued in future projects. This new controller would allow us to graft multiple real-time features, such as pellet consumption tracking, cloud-based control interface and dynamic extrusion adjustments without taking precious clock cycles from the extrusion control loop.

This new controller provides two physical cores connected by a bus. The first core is an ARM Cortex-M7, which is more powerful and dedicated to managing peripherals and auxiliary functions, such as sensor readings, pellet dispensing, and cloud communication. The second core is an ARM Cortex-M4, exclusively dedicated to managing the extruder and generating the necessary signals for it. One benefit of this architecture is the precise generation of the motor control signal, unaffected by the measurement loop or the program running on the microcontroller.

By utilizing remote procedure calls pipelines on the M4 core, it is also possible to influence the extrusion setpoint through an MQTT message from a cloud server and the M7 core.

Furthermore, the higher execution speed at all levels allows for the implementation of advanced control techniques (such as input shaping and PID), further improving the quality of the printed parts.

## Fixing printing issues

Printing large parts comes with a specific set of challenges. Initial parts requested by the IWU partner were also produced as demonstration pieces. However, certain unwanted phenomena, such as warping, leading to detachment of the printed part from the print bed, were observed.

This phenomenon is caused by the contraction of the deposited filament during cooling. The successive layers shrinking throughout the part greatly amplify this effect. Substantial internal stresses appear on the first layers, causing partial or complete detachment from the print bed.

Several solutions exist to address this problem:

- Control the cooling process and the polymer crystallization in the deposition area.
- Ensure exemplary thermal homogeneity on the initial layers to reduce differential cooling.
- Precisely calibrate the thickness of the first layer.

To address a significant portion of this problem, a new 800x800 mm heated bed was fully designed, and the associated components were ordered and purchased. The heated bed consists of an aluminum plate with adhesive silicone heating elements and insulation attached underneath (Figure 44). These elements were sized based on thermal simulations to achieve a temperature above 100°C quickly (within 20 minutes). This temperature allows the use of technical polymers such as ABS, PA6, and Polycarbonate. The bed also reaches a commonly used temperature of 65°C for 3D printing in less than 5 minutes. Furthermore, the device incorporates a leveling system with adjustable knobs to optimize the quality of the printed parts. This comprehensive leveling mechanism ensures a flatness of 10µm across the 80 cm printing area. The heated bed was also designed to withstand potential collisions with the extruder. Finally, a borosilicate glass plate is mounted on top of the heated bed to serve as the print surface, similar to some FDM 3D printers. The electrical enclosure and regulators have been installed, and during the printing tests, it quickly became evident that the heated bed performs well, providing excellent adhesion for the printed parts.

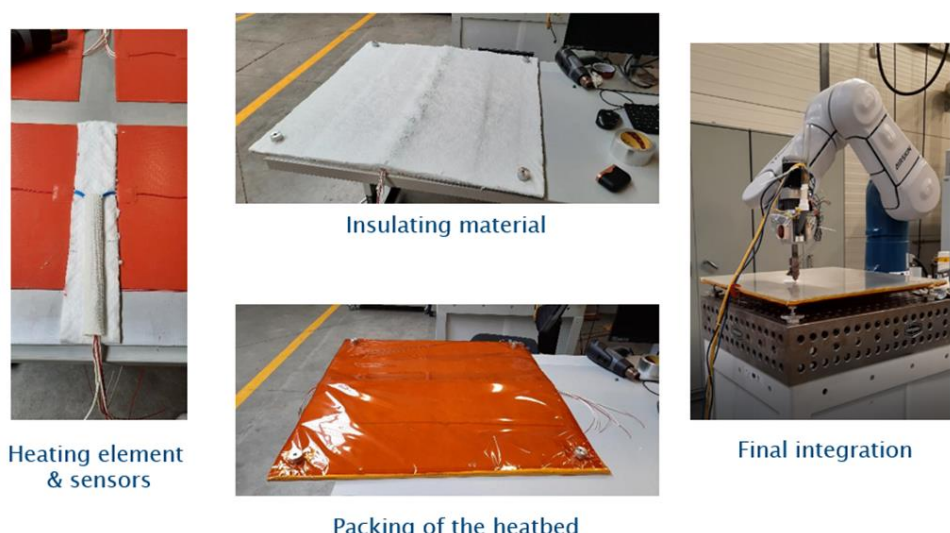


**Figure 44: Build plate construction**

Additional issues arise from the surface finish of the printed parts. Noticeable "blobs" or "zits" can be observed on the surface. These defects are inherent to the operation of pellet extruders (Figure 45). Unlike Fused Deposition Modeling (FDM) printers, pellet extruders do not have the ability to retract the molten polymer during layer changes or positioning moves. Consequently, there is residual pressure in the extruder that forces a certain amount of polymer through the nozzle.

To address this issue, the robot post-processor for VAL3 has been further enhanced to accommodate this characteristic. An algorithm has been developed to dynamically compensate for the residual pressure. As a result, the extrusion movements are desynchronized from the robot movements, enabling the flow of polymer to be shut off before completing the printing move. This technique effectively utilizes the oozing material to deposit the last few millimeters of each printing move, thereby minimizing the appearance of blobs and zits on the surface of the printed parts (Figure 46).



**Figure 45: Printing defects in large volume parts**

Hereafter, the results are obtained after all improvements on one ISF tool design.

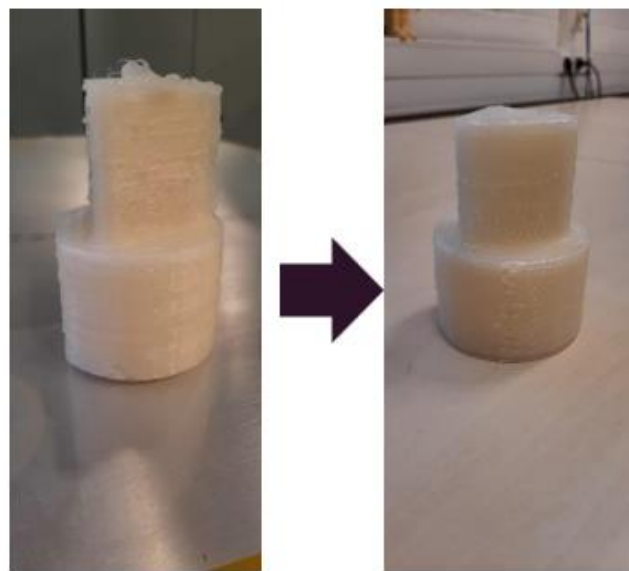


Figure 46: Printed die surface quality improvements

### Automatic pellet feeding

In order to automate the process and facilitate the production of large components without requiring constant human supervision, as well as to enhance the reliability of the input material supply, a pellet feeding system has been devised. The operational principle of the system is as follows:

A reservoir, capable of holding up to 5 kg of pellets, is positioned above the robotic system and connected to the extruder via a flexible tubing arrangement. Through the utilization of a servo motor-controlled finned wheel, the system is able to dispense pellets in a controlled manner (Figure 47).

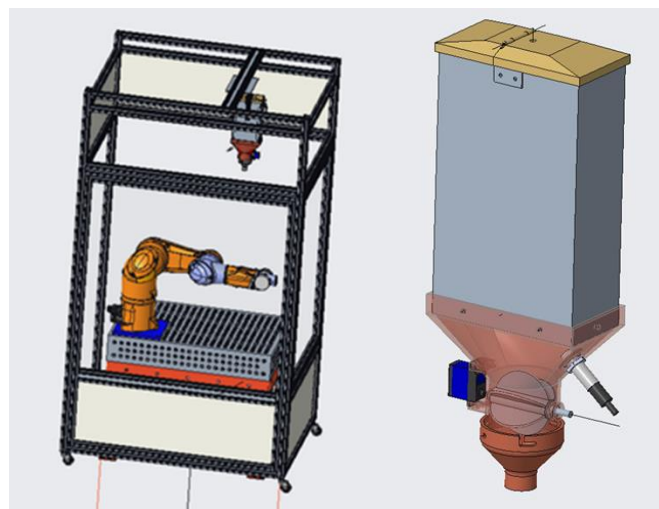


Figure 47: Automatic pellet feeding station

When the pellet level within the extruder tube falls below a predetermined threshold, an integrated capacitive sensor detects the absence of pellets and relays this information to the reservoir. Consequently, the reservoir releases a specified quantity of pellets to replenish the supply. Monitoring of the pellet level in the reservoir is facilitated by a secondary capacitive sensor. In the event that the reservoir nears depletion, a notification is generated and transmitted to the user through a cloud-based platform.

The entirety of the system is mounted on a structure composed of aluminum profiles, incorporating both doors and Plexiglas panels. The panels serve a dual purpose:

- They safeguard the robot's immediate environment during operational visits and provide suitable mounting points for additional monitoring apparatus, including cameras and sensors.
- They shield the printing volume from potential air currents and fluctuations in temperature that could significantly impact the consistency and quality of the printed components.

Such an arrangement is needed to avoid "pellet bridges" caused by the weight of the material in the feeding section, the pellet geometry, as well and the angle of repose of said pellets.

### Testing of different polymers

#### a. PLA

The robotic 3D printing process developed as part of the RapidSheet project has been extensively utilized during this period. It is evident that the improvements made to the extruder in previous steps have yielded positive results, resulting in a robust and reliable extrusion system.

Regarding mechanical characterization, various test specimens have been manufactured using 3D printing, with different filament orientations, either transverse, longitudinal or a combination of both. These specimens were subsequently subjected to three-point bending tests at the SIRRIS laboratory. Three point bending was chosen as it is the most repeatable testing setup for polymers and 3d printed polymers.

For the PLA 3D870, a grade specifically designed for 3D printing, the datasheet provides the following flexural strength values for 3D-printed parts based on the direction of applied load:

- 73 MPa in the XY plane
- 46 MPa in the ZX plane (inter-layer strength)

In practice, you can often expect a degradation of those results of around 10% when processing the polymers directly in a pellet extruder. This is due to the high level of shear the polymer experiences in the extruder. Our results were as followed:

- 64 MPa in the XY plane
- 41 MPa in the ZX plane

These results are obviously slightly lower, this can be explained mostly by two factors:

- The values as printed in the datasheet are obtained after a thermal annealing process, consisting of treating the parts at 110°C for a few hours. This helps improved the crystallinity percentage.
- The values are obtained from a filament-based printer, where shear stresses are much lower.

Subsequently, material data sheets were prepared, including the following information:

- Recommended printing parameters for each material.
- General best practices and thermal considerations for 3D printing of polymers.
- Physico-chemical characterization through DSC (Differential Scanning Calorimetry) analysis.
- Results of mechanical testing.
- Detailed information on the extruder control loop, as well as a calibration template for material flow rate in the extruder.



**Figure 48: Flexural strength samples**

b. Testing of other polymers (PA6 + GF, PEI, ABS, ABS + GF, PC, ...)

Several other polymers were also subjected to testing, including virgin or filled nylon, ABS, polycarbonate, and a high wear resistance PBT. While ABS demonstrated satisfactory printability, it did not exhibit significant improvements in mechanical properties compared to the extensively modified PLA 3D870. On the other hand, certain polymers such as polycarbonate or polyetherimide proved challenging to print large parts with due to their high shrinkage, requiring a heated chamber for successful printing.

Considering factors such as ease of printing, consistent results, and acceptable mechanical properties, PLA emerged as the optimal choice for the project.

Additional demonstration parts were printed using the robotic system and subsequently sent for testing. Due to the tight tolerances (+ - 50µm) required in certain areas of the parts, it was deemed necessary to perform post-machining operations to achieve the desired precision. Specifically, precise machining was carried out on designated areas of the dies. To accommodate the shorter length of these dies, the nozzle size was reduced to 1.2mm, and the printing

was conducted at a layer height of 1mm. The final printed parts consisted of three shells, resulting in a wall thickness of approximately 3.5mm. Additionally, the internal volume was filled using a specific geometry that occupied 30% of the total volume.

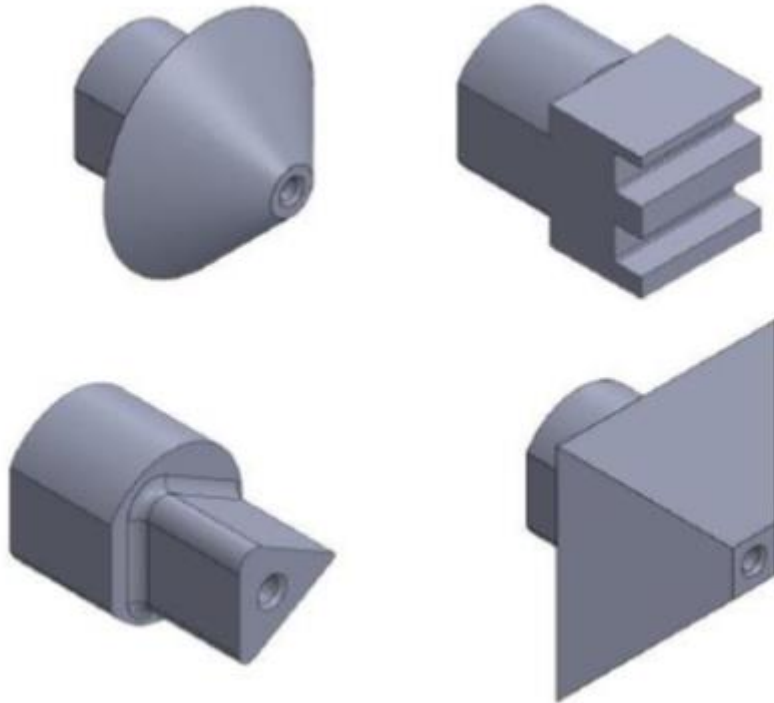


**Figure 49: Die geometries**

For large dies, some other printing techniques are required in order to minimize the printing time without compromising the mechanical integrity of the dies. Several possibilities were tested.

The first test was done using a gradual infill. This approach involves starting the print with a low infill percentage of 0-10%, and gradually increasing to a high percentage to support the top layers of the part in order to ensure a certain level of mechanical strength and proper support for the top surface of the part.

A demonstration part showed a time savings of 53% (1 hour and 30 minutes reduced to 48 minutes) using this technique. However, it should be noted that this option should be reserved for parts with a low draft angle on the side surfaces due to the initially low infill percentage.

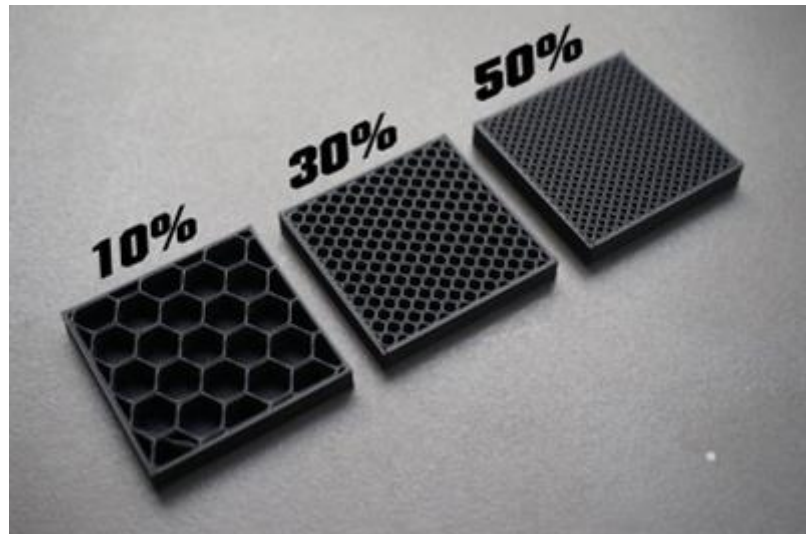


Figure 50:

The second approach proposed was to use filling blocks. In order to save time compared to the conventional approach of 3D printing with walls and infill, an idea illustrated in below involves replacing a portion of the part with filling blocks. In this method, a hollowed-out part is initially printed, and then the process is paused at a certain stage. At this point, a block is inserted to fill the cavity and provide support for the remaining part to be printed. In theory, significant time savings can be achieved with this technique. However, it presents a challenge: the filling block is not heated and may not always be made of a compatible material with the one being deposited. As a result, the adhesion of the first layer to the filling block may not be optimal and can result in defects. However, these issues tend to be resolved as the printing progresses. Our choice for a filling material ended on machinable polyurethane foam.



Figure 51:

A demonstration part allowed us to determine the following time savings:

- Original printing time: 7 hours 20 minutes
- Printing time with filling: 3 hours 52 minutes

The total time savings amount to approximately 42%. Further optimization could potentially increase the time savings, but it may compromise the integrity of the final part. Considering the relatively weak adhesion between the filling block and the 3D-printed part, the filling block can be recovered and reused for subsequent parts. Therefore, this technique should not significantly affect the overall circularity of such an approach.

### Surface quality improvement and details addition

Unlike traditional 3D printing, which involves stacking horizontal layers, non-planar 3D printing starts with horizontal layering and finishes the part with a series of finishing layers created by 3D/XYZ movement of the extruder. This approach significantly improves the surface quality of curved parts. The benefits of this technique for producing tooling for ISF (Incremental Sheet Forming) can be observed in the figure below, where the typically encountered stepped surface finish is replaced by a very smooth surface that is well-suited for precise sheet metal forming.

The geometric approximation resulting from slicing the model into horizontal layers is also eliminated, ensuring that the printed part is perfectly identical to the original 3D model.

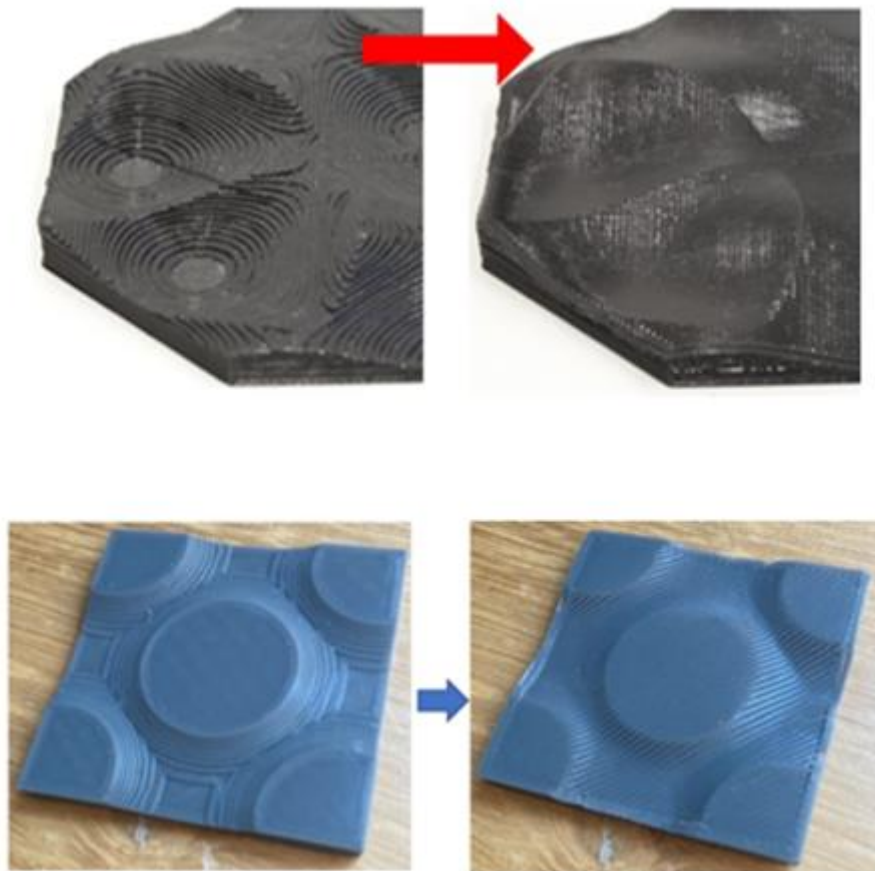


Figure 52:

One of the main challenges of non-planar 3D printing is the lack of software solutions capable of generating these specific trajectories. Traditional 3D printers, for example, can utilize add-ins like Slic3r, but their limited freedom of movement restricts non-planar capabilities to very shallow curvature angles of around 10 to 15 degrees. This limitation is due to the geometry of their printing nozzle, which is typically flat and wide, leading to potential collisions with the rest of the print volume.

In our case, an industrial robot provides much more freedom of movement, but a commercial slicer solution cannot be used "out of the box."

In this task, various existing solutions were analyzed and compared to determine the best approach for Sirris. Among them, a modified version of Slic3r was thoroughly studied.

By using this software to generate non-planar trajectories and then post-processing the code, it was possible to produce non-planar parts with our robotic 3D printing system. However, we observed areas of over- or under-extrusion in certain places depending on the curvature of the original part.

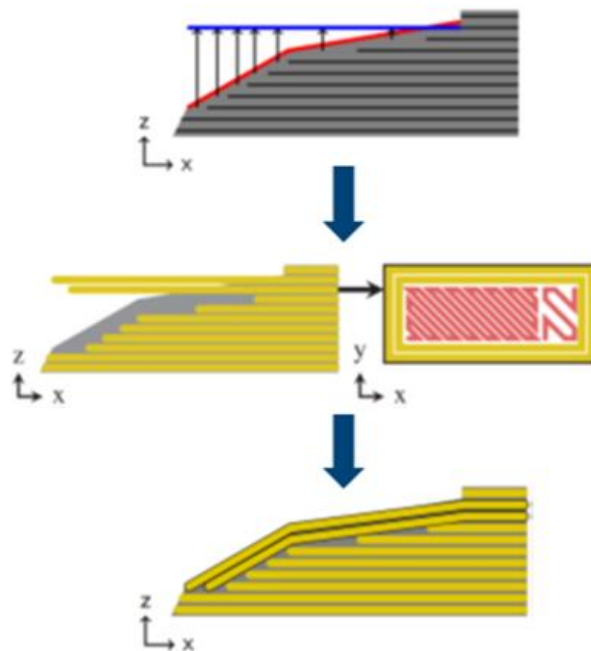


**Figure 53:**

Indeed, it appears that the last step of orthogonal projection is causing issues and resulting in areas of over- or under-extrusion. Using Slic3r to generate non-planar trajectories is therefore not a perfect solution. In the short term, we can limit the printable curvatures in the non-planar printing process to mitigate the occurrence of over- and under-extrusion.

In order to improve surface quality, a slightly narrower nozzle with a diameter of 1.2 mm was integrated into the extruder. This change slightly increases the printing time but reduces the visibility of surface defects. Additionally, the residual pressure in the nozzle was taken into account in the software. When the extruder stops between two movements, the residual pressure causes a small amount of material to be extruded from the nozzle. This results in minor surface defects, which are particularly noticeable on small or medium-sized parts or parts with holes. Therefore, stopping the extrusion slightly before the end of the trajectory allows the use of residual pressure to extrude during the final movement and eliminate the defects.

By comparing the printed parts in three ways:

- using a 1.5 mm nozzle
- using a 1.5 mm nozzle with residual pressure compensation
- using a 1.2 mm nozzle with residual pressure compensation,

The following observations were made:

- Details and corners are drawn much more accurately.
- The top surfaces are much smoother and suitable for incremental forming.
- The printing time is slightly longer (75 minutes compared to 60 minutes with the 1.5 mm nozzle) (Figure 55). However, this is still significantly shorter than the time it would take a conventional FDM printer to produce these parts (nearly 9 hours of printing).

Therefore, the process is well-refined with the new nozzle, and a good compromise has been found between speed and print quality.

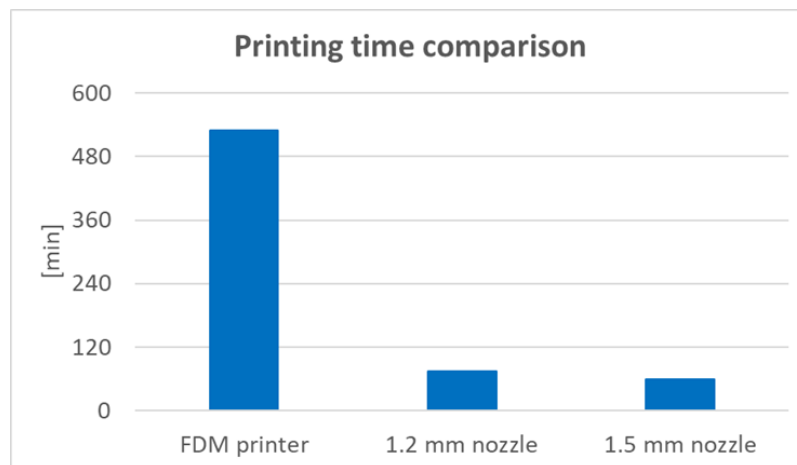


Figure 54: Printing time comparison between various nozzles and technologies

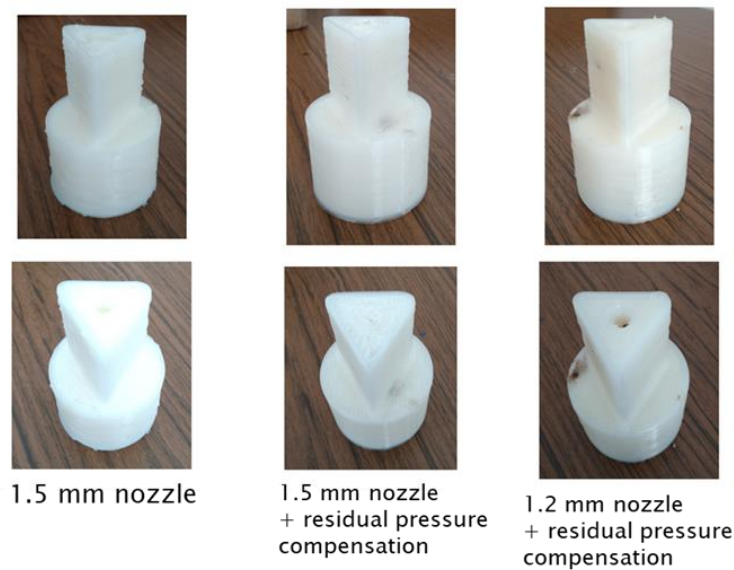


Figure 55: Comparison of the finish between different nozzles

## Evaluation of the feasibility and the quality of post treatments

Post treatment of the printed parts is possible. In order to improve the dimensional accuracy on some parts of the tools up to the required 50µm tolerances, a machining is mandatory. Such a machining can be done in a conventional milling machine, however special care must be taken to avoid issues such as delamination between layers and overheating the parts. PLA has a low vitreous transition temperature, at 65°C it starts to melt and soften significantly. Those temperatures are easily reached by the machining process, so the operator must use a slow feedrate as well as a constant coolant flush to keep the PLA in a brittle, machinable state.

The pressure applied by the machining tool on the die should also be kept at a minimum. While PLA has a high tensile strength, the bond between each layer on a small-scale part will be rather weak and brittle in tensile conditions. This is due to the cooling requirement of the printing process, and could cause the part to instantly delaminate in the weak spot between two layers during the machining process. As such, the tool should have a wide contact pattern with the part to avoid stressing particular areas.

Further improvements of the mechanical characteristics of the PLA are possible through an “annealing” process. The parts are treated in an oven at 110°C for a few minutes, this process helps promote the crystallization of the PLA and relieve internal stress, and as such raise it to a very high crystallinity percentage. While this process also helps forming stronger bonds between layers, it is not recommended for precise parts or parts which need to be stiff, as warping and a loss of rigidity is inevitable.

## 7.5 WP5: Virtual twins for simulation of manufacturing process and machine tool behavior

Dedicated software was developed within the project to provide reliable identification of flow stress model parameters for a specific hardening equation. The general concept of the implemented tool is shown in Figure 56. Each implemented feature was gathered in the independent module to make the solution as universal as possible. All presented methods can be used in both sequential or parallel manner.

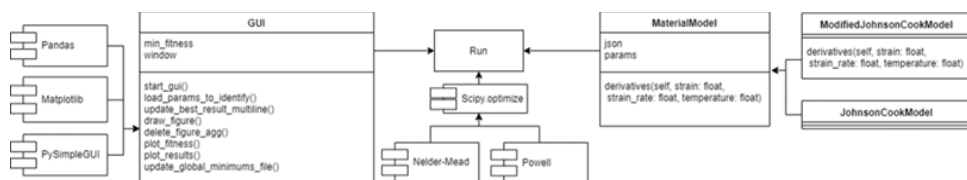
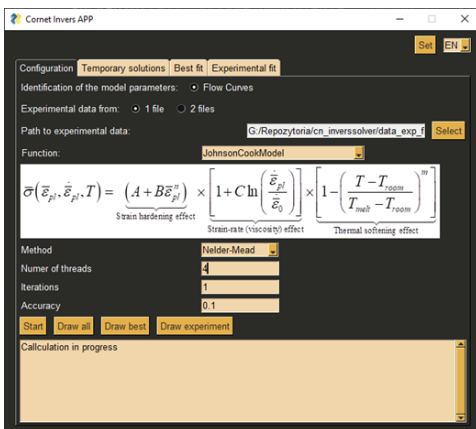


Figure 56: Concept of the material model parameters identification tool.

Material model parameters identification tool takes into account two goal function minimization algorithms, namely Nedler-Mead and Powell methods. For the sake of the project, the Johnson-Cook (JC) model is particularly considered, but the proposed tool can be easily extended with other optimization methods (e.g. particle swarm optimization) and flow stress equations (e.g. Zerilli Armstrong). The tool is implemented within the commonly used Python scripting language based on the following modules: threading, pandas, matplotlib, scipy. Additionally, for simplification of the optimization process implemented solution was equipped with easy to use graphical interface based on PySimpleGUI as seen in Figure 57.



**Figure 57:** The graphical user interface for the model parameters identification tool.

The primary sheet material investigated during the research is an aluminium alloy with flow stress curves provided by IWU. Based on the available data and the presented software, a set of the JC model coefficient was determined. An example of a comparison between the JC predictions and experimental data is shown in Figure 58.

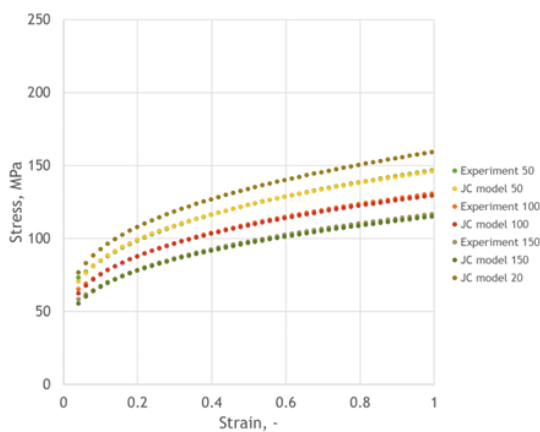


**Figure 58:** A comparison of the JC predictions and experimental data.

The developed JC model will be used for the macro scale SPIF simulations realized within the project.

However, the multi-scale simulation concept considering the macro and micro scale behavior will also be investigated within the project. Therefore, the micro-scale model as a full-filed approach was developed within WP5 to provide a material model for the lower-length scale simulation. The microstructure morphology for the digital material representation model was generated based on the cellular automata algorithm. The principle of cellular automata is based on three fundamental concepts: the cellular automaton space (a grid of a finite number of cells described by several state and internal variables), the cell neighbourhood (qualifies its closest neighbours) and the transition rules (control the changes in the cell states). Thus, the first step in the CA grain growth algorithm development is to establish the discrete space composed of cellular automata cells. With reference to 2D space, it will be a grid consisting of squares. In the next step, a set of cells is selected randomly, and then a state variable describing the cell state is set to "already grown". These cells represent grain nuclei. The second step of the algorithm is focused on grain growth. The transition rule for this stage is defined as follows: when a neighbour of a particular cell in the previous time step was in the state "already grown",

then this particular cell can also change its state. Particular grains grow with no restrictions until the impingement with other grains. After that, they grow only in the area where no grains are observed. This process is performed until the investigated computational space is covered by grains. The presented model was implemented to provide an input microstructure model for further simulations. To this research, the initial single-phase Al digital microstructure morphology was generated with the cellular automata grain growth model within the 3D computational domain. The size of the CA space was selected as  $150 \times 150 \times 150$  cells with a physical size of  $1\mu\text{m}$ .

To properly capture behaviour related to grain morphology during further FE simulations, very fine finite element meshes have to be used, which leads to excessive computational times. However, with coarser meshes, some microstructure features can even be neglected, affecting the quality of simulation results. To reduce computational time and maintain high accuracy of results, the solution-specific non-uniform FE meshes that are refined along the Al grain boundaries were generated. This approach was used to discretize the DMR model with the C3D4 FE elements within the project. To take into account the influence of various crystallographic orientations on the grain response, different flow stress curves, diversified with the Gauss distribution function, were assigned to the model. The final DMR model generated as input for further multi-scale simulations is presented in Figure 59.

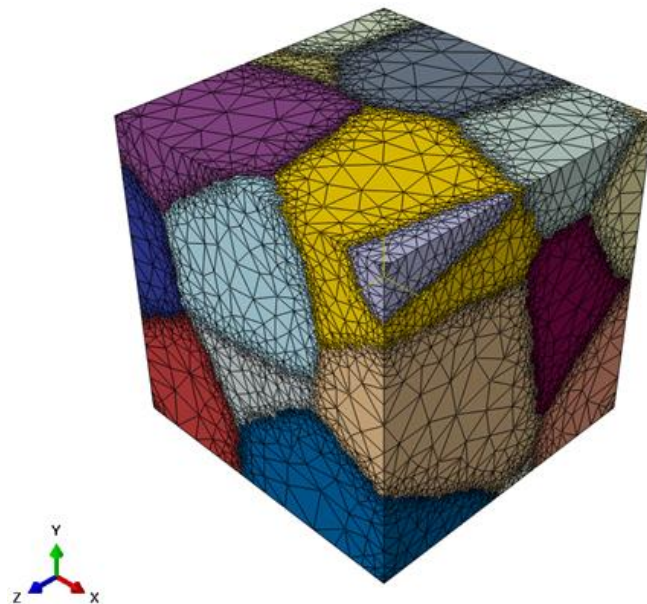
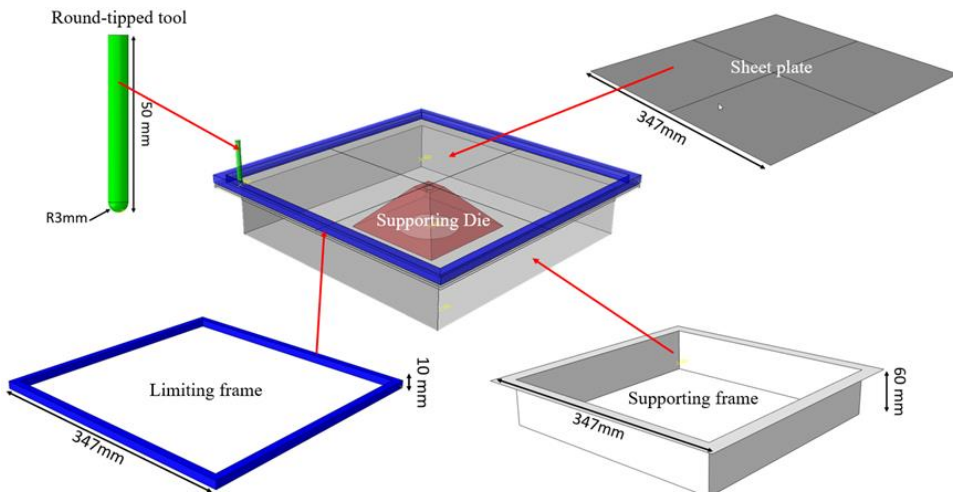


Figure 59: The digital material representation model of the investigated aluminium sheet material.

### Simulation ISF-Process

The commercial finite element program Abaqus carried out numerical simulations of the ISF-forming with different shapes of the supporting counter tools and specified deformation conditions. Developed numerical models consider five major elements of the process: round-tipped tool, limiting frame, supporting frame, supporting counter tool and 1mm thick aluminium sheet plate. The round-tipped tool is moving along the previously programmed path and is the main forming tool. The limiting and supporting frames do not allow the sheet plate movement upward during deformation. The supporting counter tool is localized in the assembly's central part and is used as support for the sheet during the forming operation. All parts, along with the assembly of the ISF process, are presented in Figure 60.



**Figure 60:** Subsequent parts and an assembly of the developed digital twin for the investigated ISF setup.

Additionally, two other digital twin models were designed to replicate the ISF machines developed at AGH university and the large-scale Mikromat 30V 5D (DynaPod) available at the IWU, as seen in Figure 61.

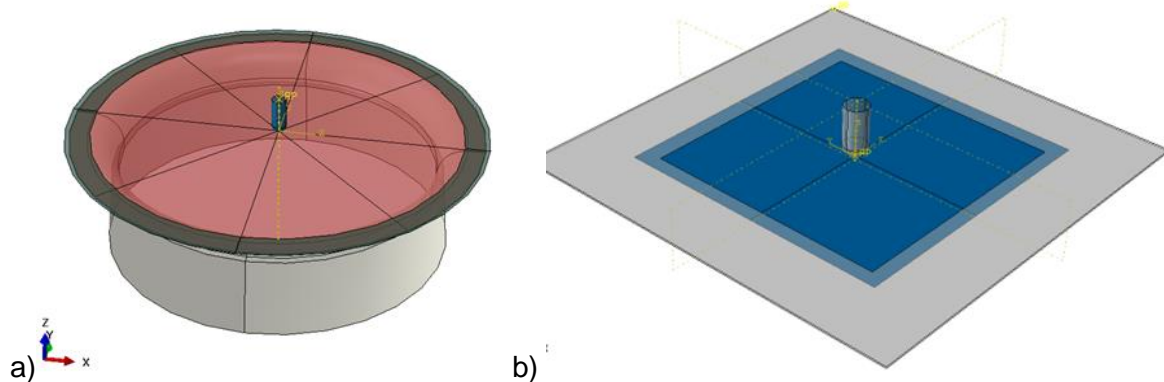


**Figure 61:** Assembly of the SPIF process for the a) setup developed at the AGH, b) Mikromat 30V 5D (DynaPod) available at the IWU.

In all cases, the constitutive equation based on the J2 plasticity and JC flow stress model were employed for the numerical investigation. Models are fully-coupled thermo-mechanical solutions. The Abaqus/Explicit solver without mass scaling was used to maintain high-quality results and eliminate any possible unphysical artefacts. The shell elements with a single Gaussian integration point (S4R) were applied for the analysis. The number of elements for the sheet plate discretization was set to 30 000. The number of finite elements was selected by sensitivity analysis of the finite element mesh and its influence on the quality of the obtained results. The core ISF simulations used three defined shapes of the supporting counter tools: pyramid, triangular and rectangular. All investigated counter tool models with their dimensions are presented in Figure 62.

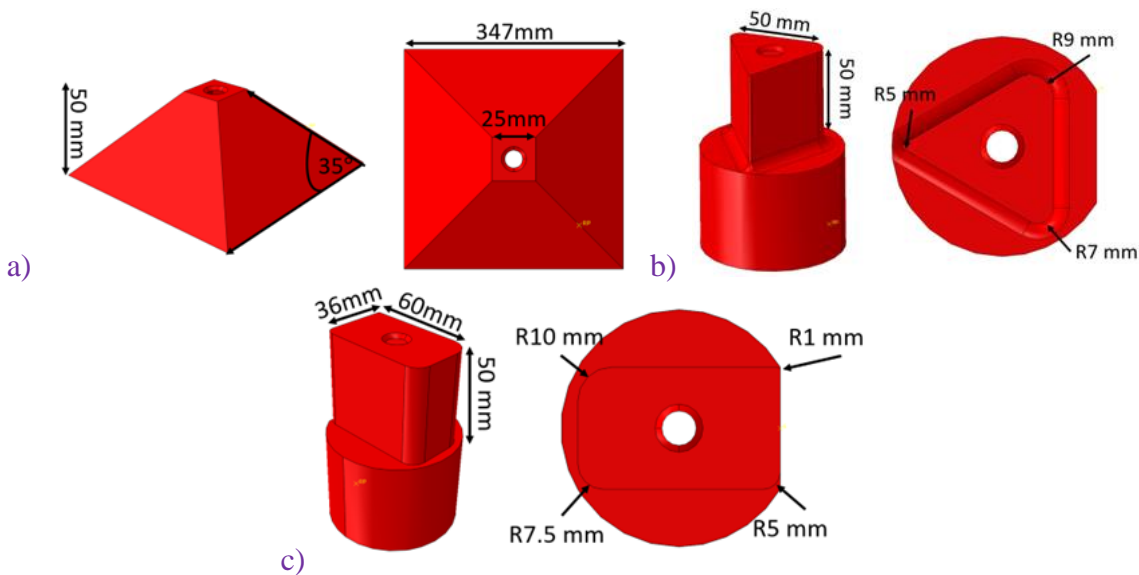


**Figure 62:** Shape with the dimension of all supporting counter tools a) pyramid, b) triangle and c) rectangular.

In this study, two series of simulations of ISF processes were prepared in which the influence of elastic properties set to supporting counter tools was taken into account.

In both series of simulations, the limiting frame, supporting frame and support counter tool are fixed in every direction. Then, the supporting counter tool was considered fully rigid in the first set of case studies. The rounded forming tip moves along a predetermined trajectory based on information embedded in the gcode file. Information about the movement trajectory of the rounded-tip tool along X, Y and Z directions was set into the displacement boundary conditions in the software. An example of the trajectory for the forming tool used in the model with a triangle supporting counter tool is shown in Figure 63.

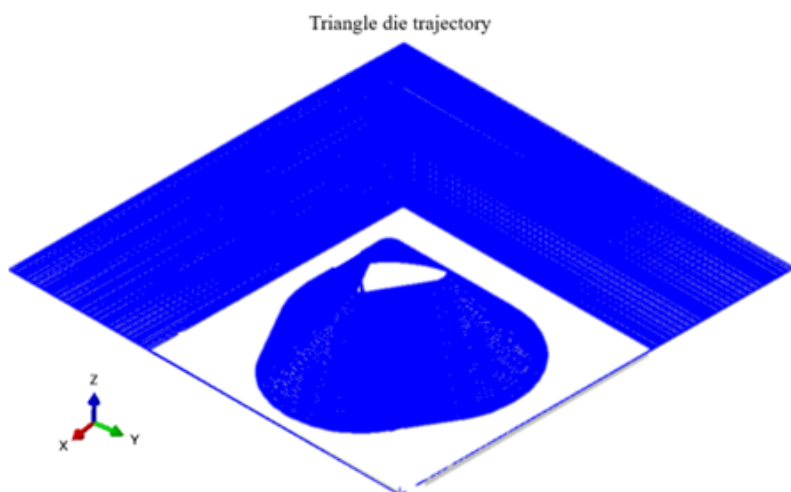


**Figure 63:** Trajectory for the rounded-tip tool used in the model with a triangle supporting counter tool.

The outer edge of the sheet plate is fully constrained and blocked by a limiting frame tool to restrain its radial movement. A Coulomb friction coefficient of 0.1 was used between the tools and the sheet.

The second set of case studies was based on similar assumptions. The only difference is that the supporting counter tool was defined as a deformable tool with elastic properties. The elastic

properties of the Ingeo Biopolymer 3D870 were used to consider the material used by Sirris for the 3D printing process of the counter tools. The Young modulus was set to 2.865 GPa and Poisson ratio to 0.34. Pyramid, triangle, and rectangular supporting counter tools were discretized with 15 000 single Gaussian point C3D8R solid elements.

Finally, the third, additional, case study was used to evaluate the capabilities for developing a more detailed simulation of the 3D-printed counter tool geometry. The 3D-printed counter tool clearly indicates the filament geometry in the final assembly, as seen in Figure 64.

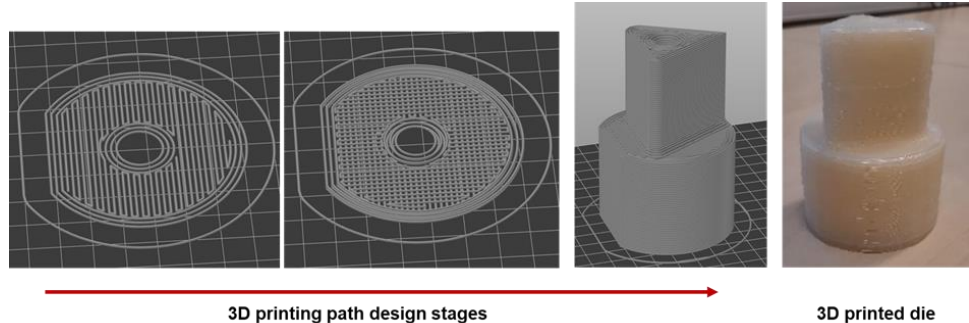


**Figure 64: Example of 3D printing path designed at Sirris and the corresponding manufactured counter tool.**

Evaluation of how this typical internal structure behaves under ISF loading was investigated within this task. Therefore, the corresponding numerical model was designed to replicate the geometry of the filament and its trajectory. At first, the concept was evaluated on a simplified test case with a rectangular counter tool subjected to loading, as seen in Figure 65. Unfortunately, already with such a simplified approach, the simulation time became excessive; therefore, only the last three deposited filament layers were considered in the first counter tool design for the ISF simulations (Figure 66).

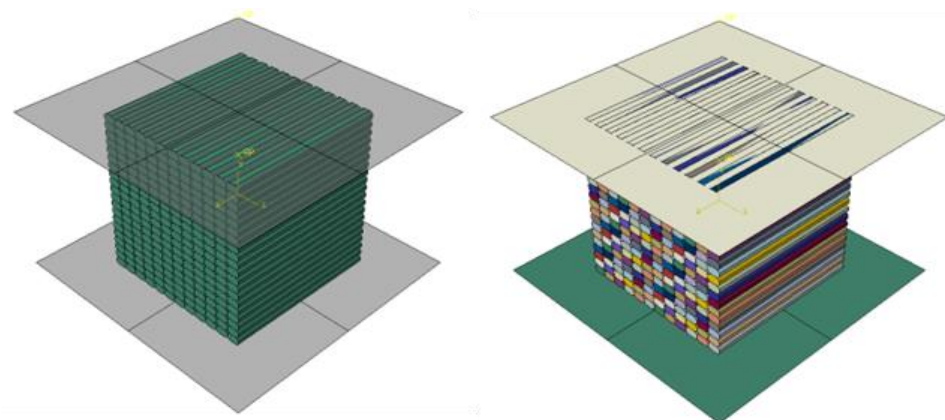


**Figure 65: A test case for the explicit consideration of the printed counter tool morphology.**

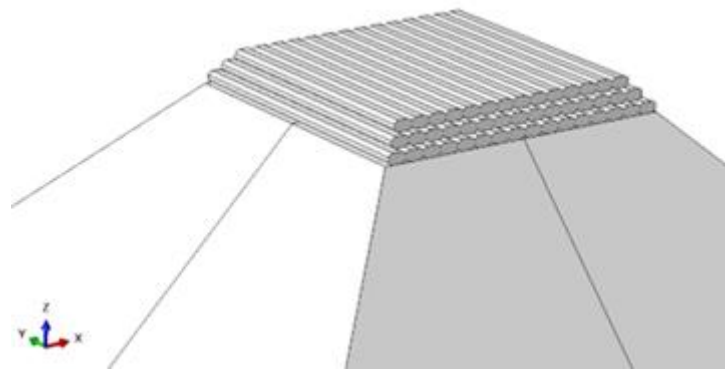


**Figure 66: The first simplification of the complex printed counter tool morphology.**

Obtained results proved that the concept is feasible and allows investigation of local interaction between the sheet and the deposited filament. At the same time, it is possible to investigate stress concentrations within the counter tool, as seen in Figure 67.

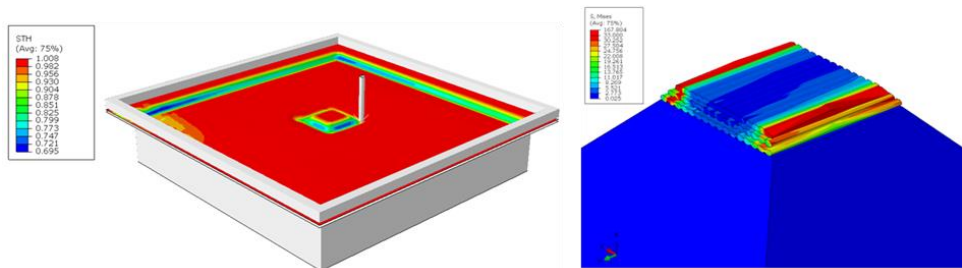


**Figure 67: Examples of sheet and counter tool behaviour under ISF conditions.**

The filament layout was simplified during the initial analysis as the single-direction parallel alignment was considered. In reality, the alignment is more complex, as presented in Figure 65. Therefore, the more complex finite element counter tool model was developed to match the real 3D filament alignment used by Sirris during counter tool manufacturing (Figure 68).

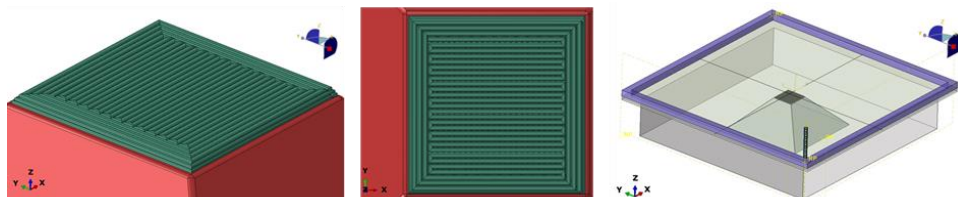


**Figure 68: The complex printed counter tool morphology.**

Unfortunately, the simulation times with such a complex model were excessive, which is why a model order reduction by symmetry planes was introduced. As a result, only  $\frac{1}{4}$  of the final counter tool model was taken into consideration during the investigation (Figure 69).

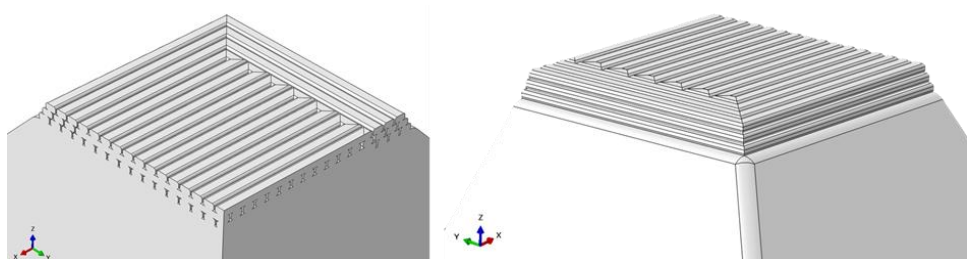


**Figure 69: Final model of complex printed counter tool morphology with symmetry planes.**

The wide range of numerical simulations to evaluate sheet material behaviour during ISF and eventually propose modifications to the process and counter tool design was realized within task 5.3.

### Sensitivity analysis

Initial simulations were realized with the developed numerical ISF models for the thick steel of 5mm. Such a thickness is exaggerated in the process but allows for checking the model's robustness. Examples of obtained results are gathered in Figure 70.

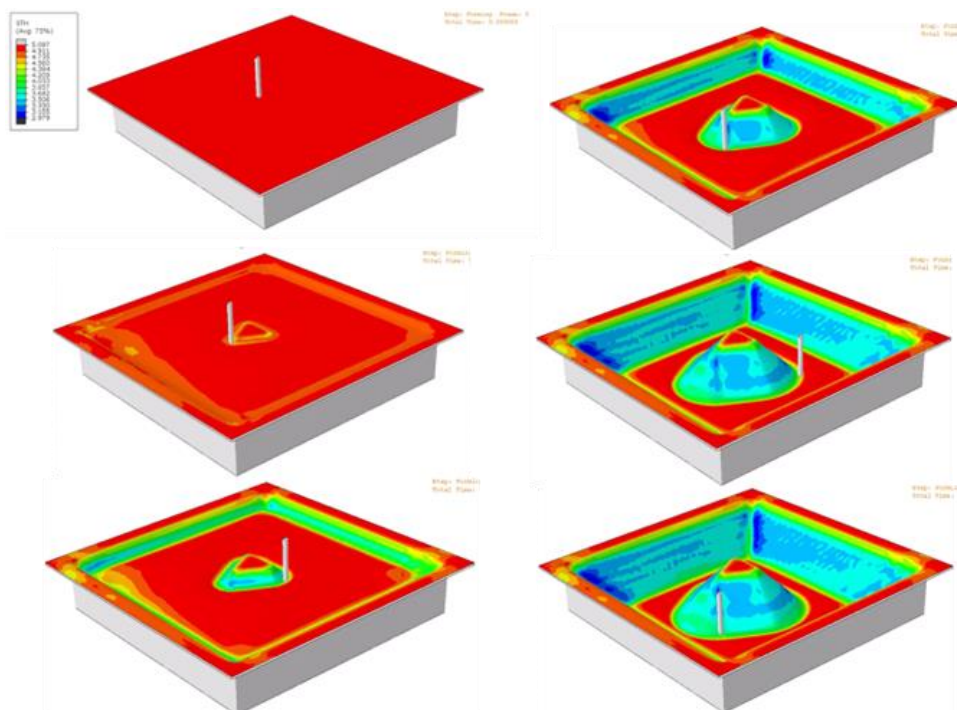


**Figure 70:** An example of thickness evolution during deformation with a rigid and sheet thickness of 5mm.

After initial model checks, the sheet thickness was reduced to 1 mm, which was used during the project. In this stage, the research focused on the evaluation of the influence of the counter tool model definitions on the material behaviour and recorded loads at the forming stylus. Force-time diagrams were generated for both investigated case studies to compare forces recorded during the deformation process qualitatively. To make the force evolution trends more transparent, the polynomial fitting curve equation was used and added to the graphs shown in Figure 71.

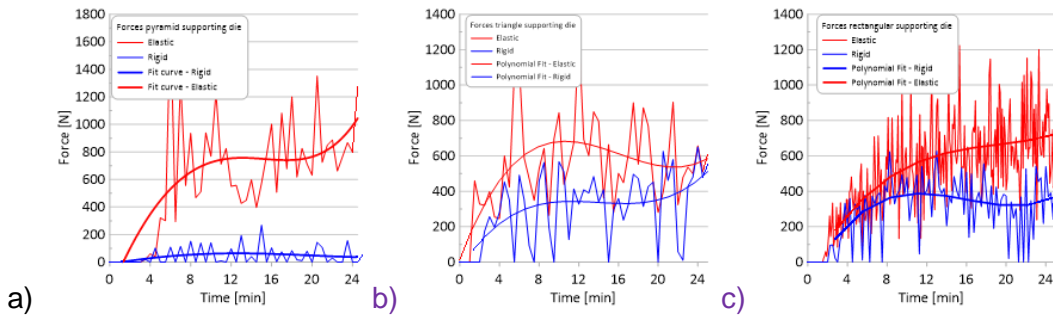


**Figure 71: Forces-time curves with the fit trend line from simulations with a) pyramid, b) triangle, and c) rectangular supporting counter tools.**

From the above curves, it can be seen that in the model where counter tools have elastic properties, registered forces are larger than in models with rigid counter tools. This is especially evident for the model with a pyramid supporting counter tool where forces are seven times higher. This behaviour is related to the fact that the elastic counter tool deforms to some extent leading to increased contact between the sheet and the counter tool. Initially, the sheet lies only on the upper part of the pyramid, and during deformation, it is deposited on the pyramid counter tool edges. This results in a progressive increase in the area of interaction between the counter tool and the formed sheet (Figure 72a). In the case of the triangular and rectangular counter tools, the top surfaces are not symmetrical and do not have side edges, which results in a smaller increase in force during the process otherwise than in the case of the pyramid Figure 72b,c. In addition, a different stress distribution can be observed on the counter tools. In the pyramid counter tool, a constant stress increase can be seen on all four edges of the upper counter tool surface. In the triangular, the highest stress increases can be observed only on its narrowest edge Figure 72b. A similar situation can be observed in the rectangular counter tool in Figure 72c.

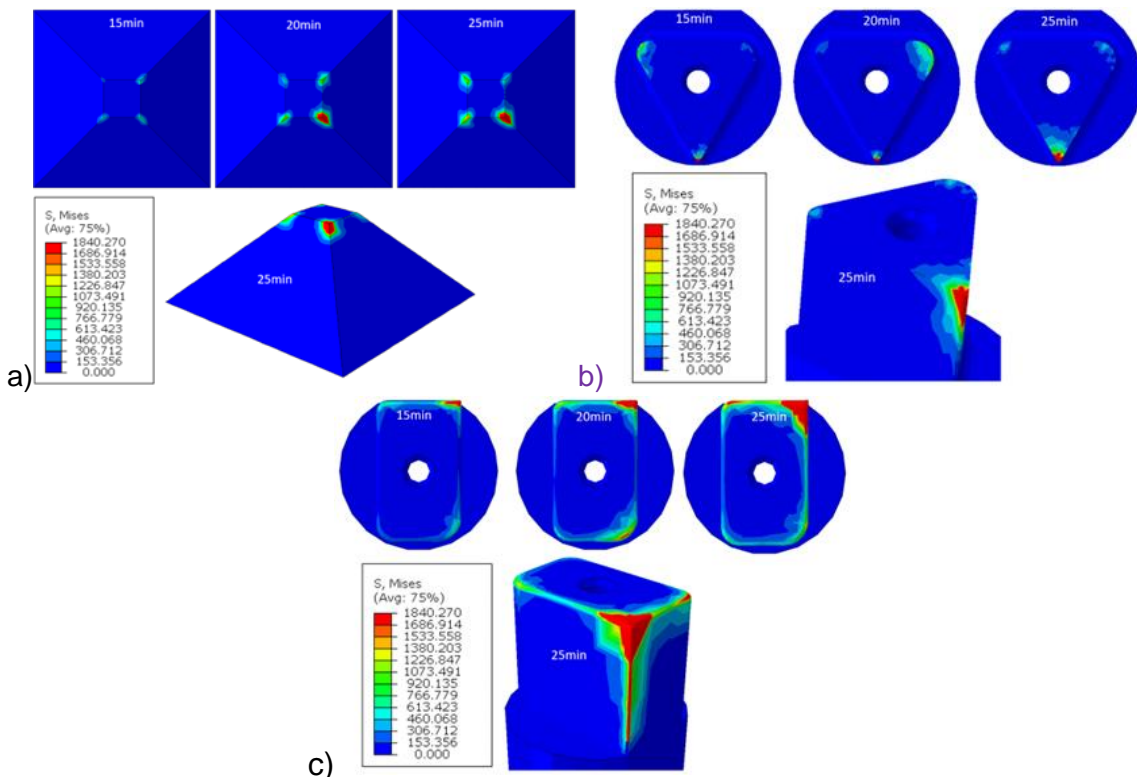


**Figure 72: Stress distributions in the elastic counter tool during subsequent time steps for a) pyramid, b) triangle and c) rectangular supporting counter tool case study.**

Obtained results indicated possible significant wear of the counter tools during ISF; therefore, its final design was modified by the introduction of rounded edges, as presented in Figure 73.

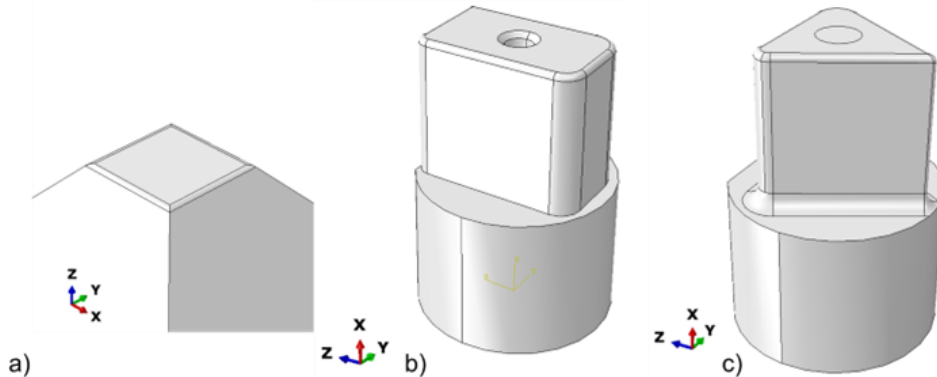


**Figure 73: Final shape design of all supporting counter tools a) pyramid, b) rectangular and c) triangle.**

During the study, another effect of assigning elastic properties to counter tools related to the sheet oscillations under subsequent loading was noticed. The oscillation of the formed sheet during the process is clear in both cases. However, this oscillation is different for the rigid and elastic counter tools. After simulations, it was noted that this phenomenon increases when an elastic counter tool model is used. In order to quantitatively analyze the range of variation of these oscillations, information was extracted from the current position of pairs of nodes lying on opposite formed edges of the sheet calculated in each timestep of the simulation. The nodes were selected to be located at the extremes of the counter tool upper surfaces. The results of these oscillations on pyramidal (Figure 74), triangular (Figure 75) and rectangular (Figure 76) matrices are shown below.

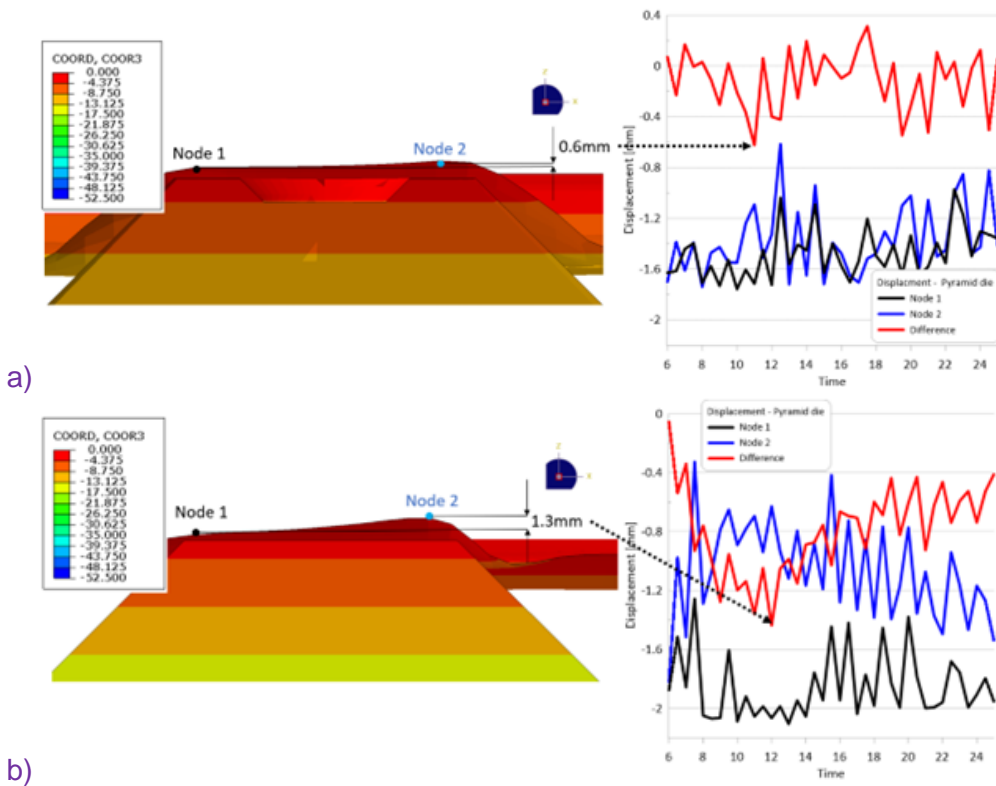


**Figure 74: Displacement of nodes in pyramidal counter tools (a) rigid and (b) elastic.**

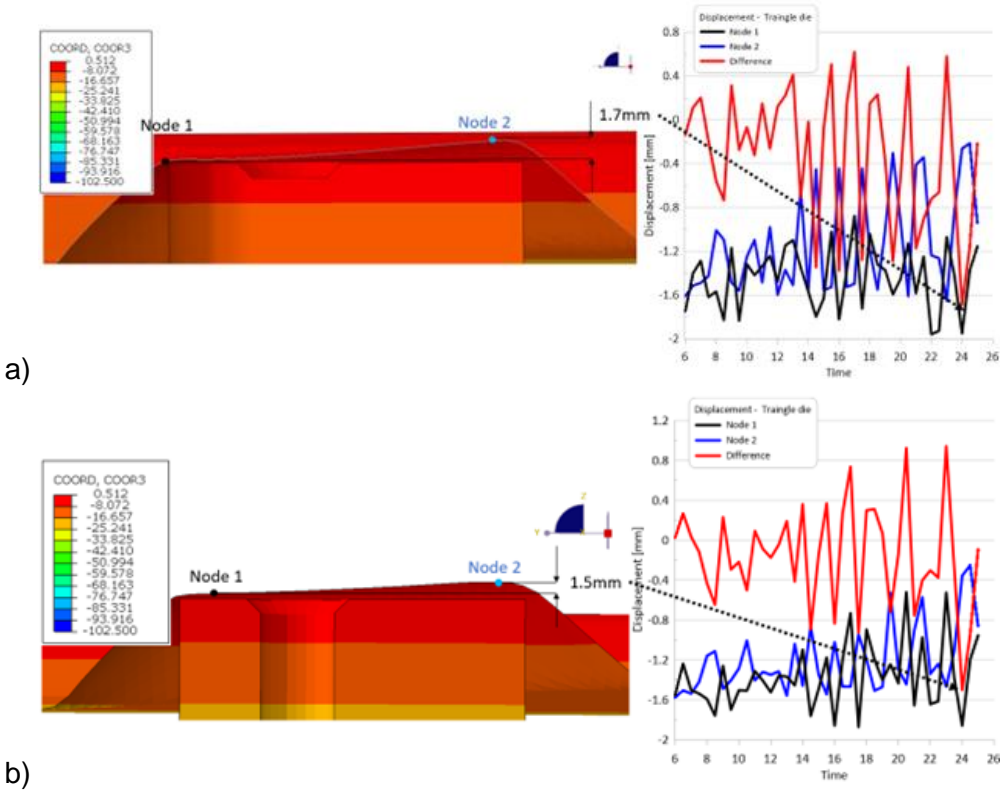


**Figure 75: Displacement of nodes in triangle counter tools (a) rigid and (b) elastic.**

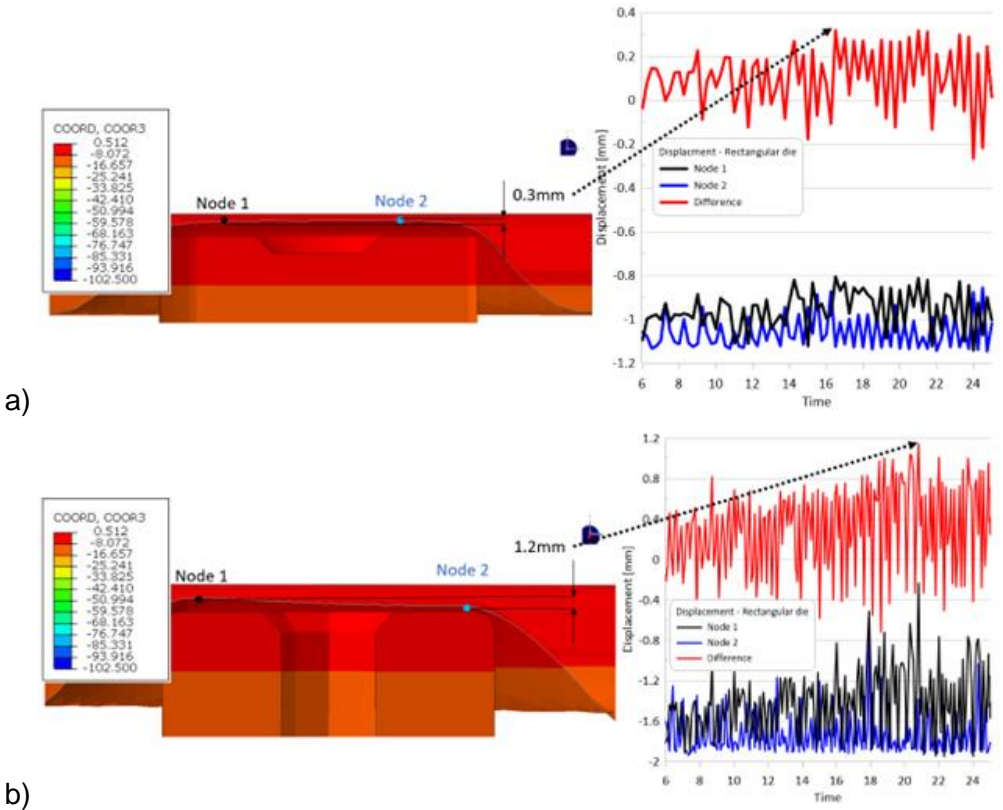


**Figure 76: Displacement of nodes in rectangular counter tools (a) rigid and (b) elastic.**

From the above results, it can be concluded that for the triangular counter tool, the level of oscillation is similar, and the difference in the position of the two nodes fluctuates around 1.5 -

1.7 mm. In the rectangular elastic counter tool, a significant increase in sheet oscillation can be noted. For the rigid counter tool, the maximum difference in the position of the nodes is about 0.3 mm. In contrast, for the elastic counter tool, this value reaches 1.2 mm. When a pyramidal counter tool is used, then the range of the oscillation also differs between rigid and elastic. Still, the most significant difference of 1.3 mm occurs at the beginning of the process, and after 15 minutes, it becomes similar to the simulation with a rigid counter tool. Figure 77 clearly shows the variations in oscillations for each simulation.

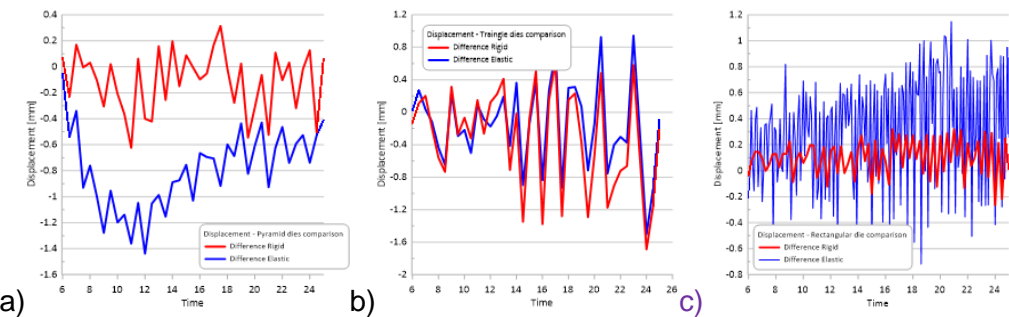


**Figure 77: Variation of sheet oscillations in a) pyramidal, b) triangular, and c) rectangular supporting counter tools.**

The computational costs are the last aspect analyzed in the use of elastic properties for supporting counter tools in ISF simulations. The calculation times are presented in Figure 78.

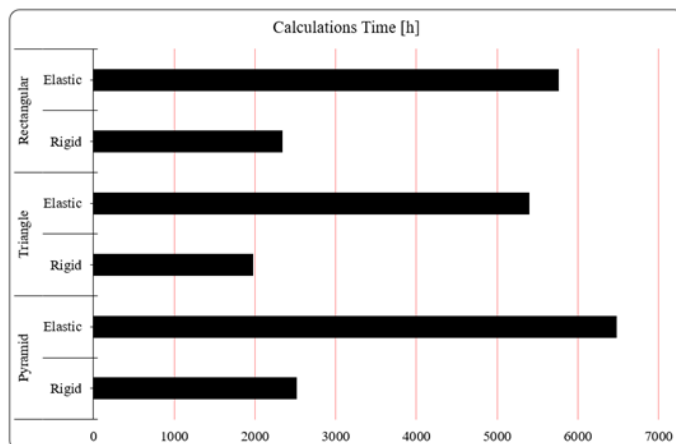


**Figure 78: Time to calculate the ISF process presented in this work.**

Calculations performed with elastic counter tools are noticeably longer, often up to three times. Of course, it is possible to use mass scaling in simulations. However, as mentioned, scaling was deliberately neglected to accurately determine the impact of elastic tools in this research.

As mentioned, the more complex variant of the counter tool model design was also investigated within the WP5. The influence of the complex counter tool surface shape, considering the deposited filament's morphology on the material and counter tool behaviour, was evaluated. Examples of obtained results in the sheet and counter tool are gathered in Figure 79 and Figure 80, respectively.

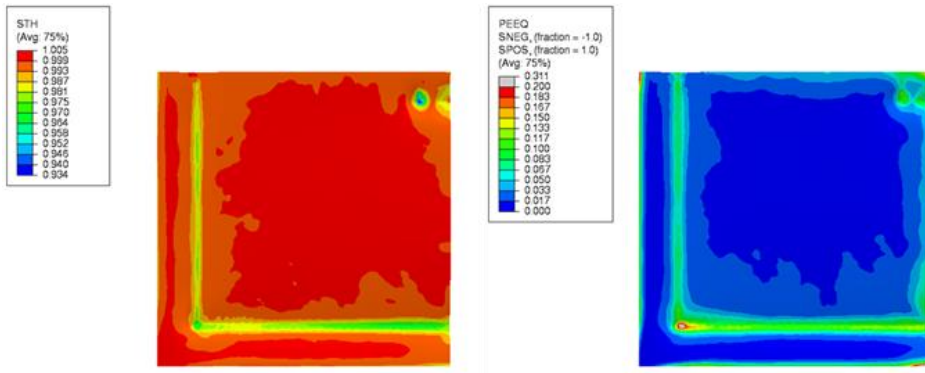


Figure 79: Examples of results for  $\frac{1}{4}$  reduced ISF model – sheet material.

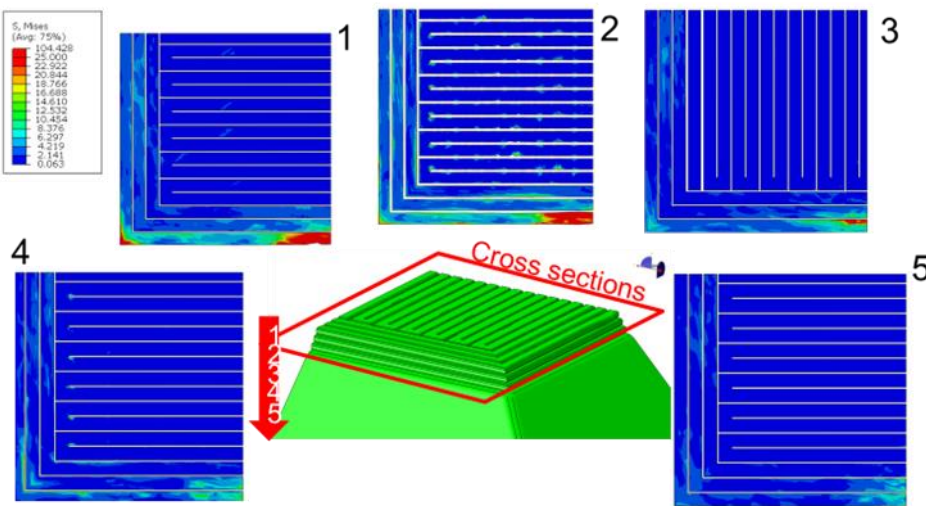


Figure 80: Examples of results for  $\frac{1}{4}$  reduced ISF model – counter tool material.

The local stress heterogeneities are even better visible at the vertical cross sections, revealing the interaction between the deposited filament during ISF loading (Figure 81).

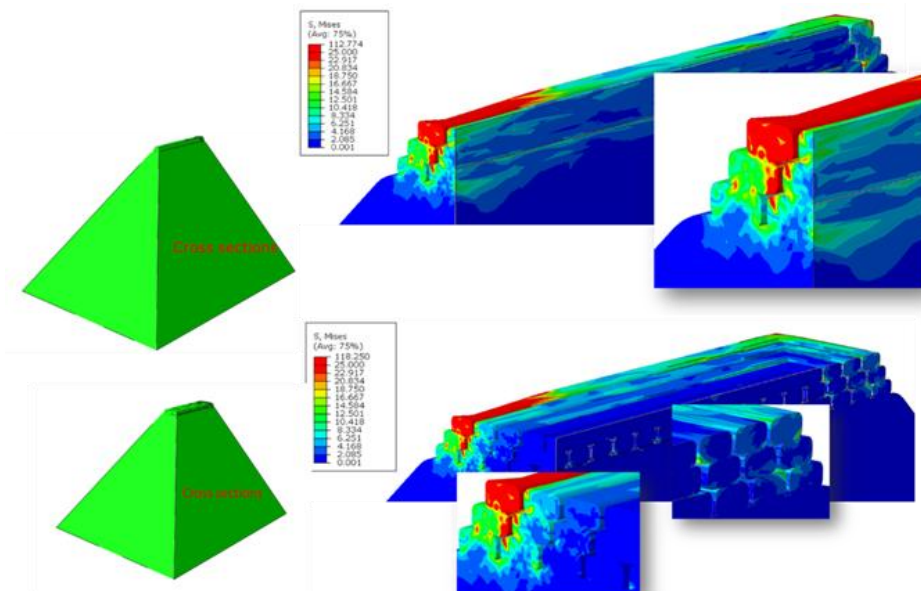
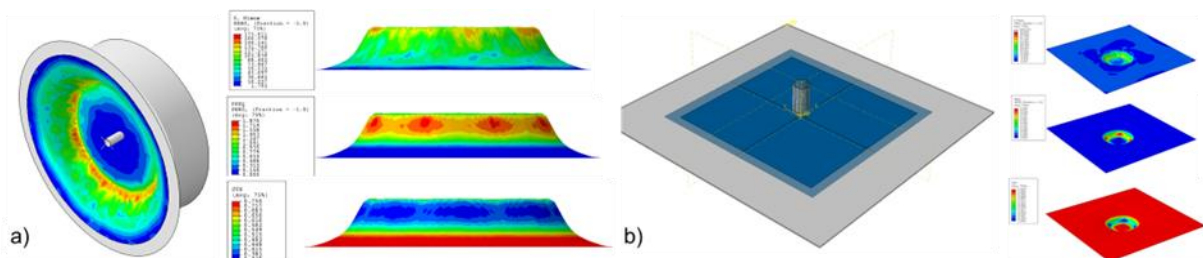


Figure 81: Local stress concentrations in the 3D printed counter tool.

Simulation results indicate some potential delamination within the counter tool during the forming operation, which should be taken into account while designing the forming tool paths in z direction.

Research within the WP5 was also used to support designing the ISF device development at AGH university and to evaluate scaling possibilities to larger equipment. Examples of results obtained for models from Figure 61 are shown in Figure 82.



**Figure 82:** Examples of simulations realized for ISF setup a) developed at the AGH, b) Mikromat 30V 5D (DynaPod) available at the IWU.

The AGH ISF model was also used to evaluate the possible influence of mentioned earlier mass scaling that could be used to speed up the simulation time (Figure 83). The initial sheet thickness was selected as 1.65mm, and the SPIF simulation was carried out without mass scaling and with mass scaling coefficient equal to 55 and 100.

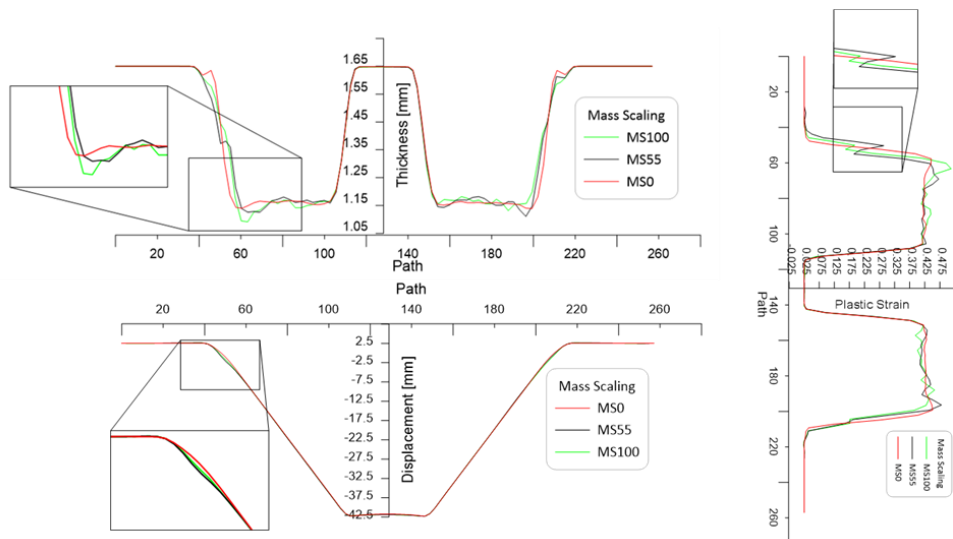


**Figure 83:** Comparison of numerical predictions for increasing value of mass scaling.

As seen, the higher the value of the mass scaling, the discrepancy between the reference results is more pronounced. However, it is evident that it is possible to select the mass scaling value, which will speed up the calculation while the error in numerical simulations is negligible.

Finally, the heterogeneities occurring at the microstructure level in the deformed sheet material were also investigated within the WP by means of the multi-scale simulation. In this case, the developed macro scale SPIF models were augmented by the DMR-based model from Figure 59. The concurrent multi-scale model was developed to evaluate the influence of marco-scale deformation conditions on the material behaviour at the micro-scale level. The information flow

is unidirectional from the macro to micro scale. The macro-scale displacement field is considered as boundary conditions for the DMR micro scale model. The DMR models were located in the two characteristic locations in the sheet, as presented in Figure 84.

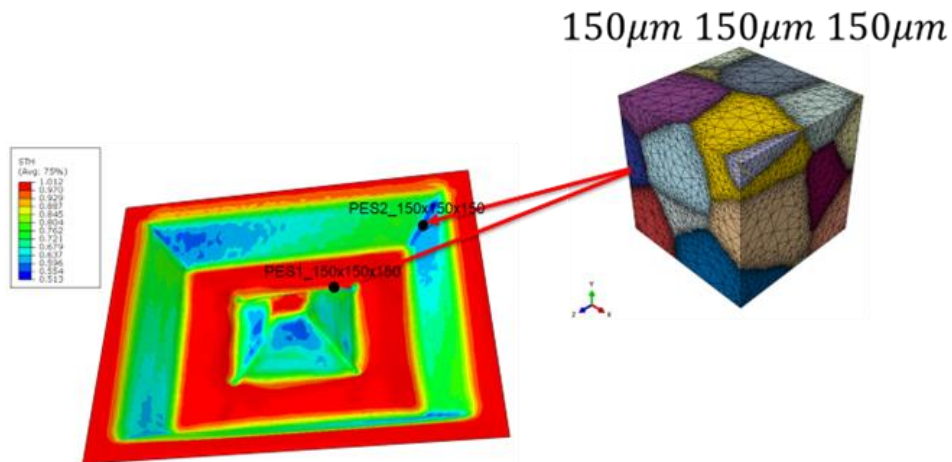


Figure 84: Concept of the concurrent multi-scale models based on the DMR model.

Examples of results from the multi-scale simulations for rigid and elastic counter tool models are gathered in Figure 85.

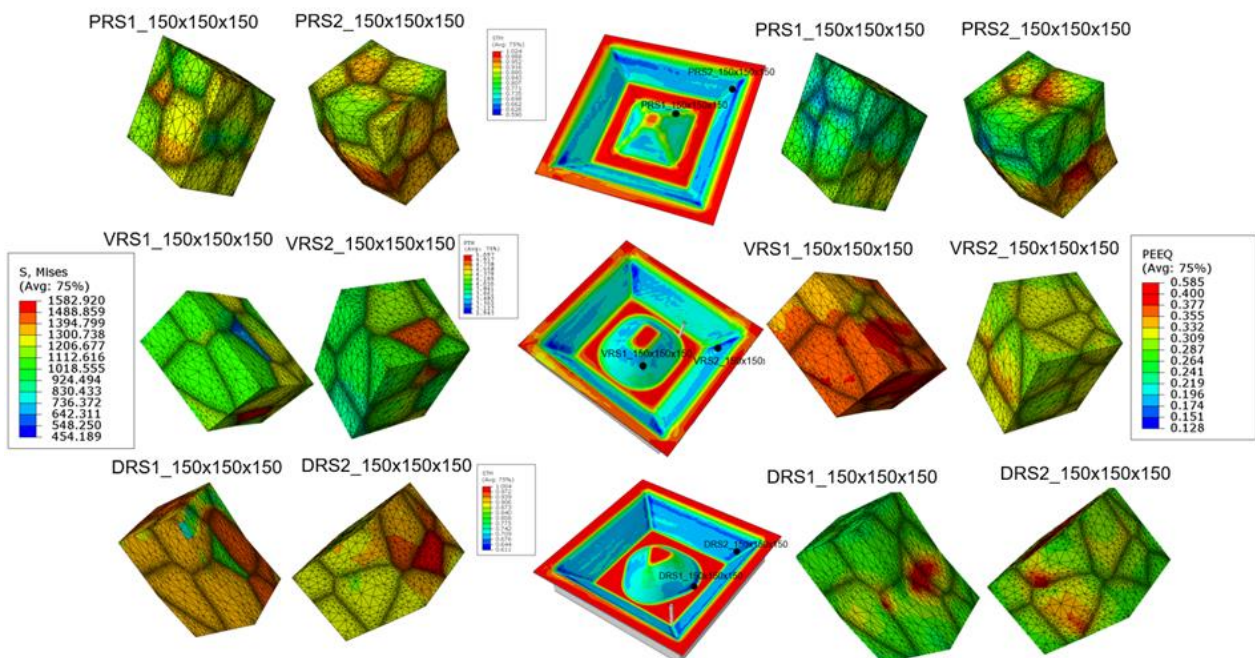


Figure 85: Equivalent strain distribution across the SPIF deformed microstructure.

As presented, the DMR model can predict local heterogeneities in the deformed microstructure, which are crucial for material behaviour during the subsequent processing operation. Such a model can predict possible fracture initiation sites not only at the macro scale level but also locally at the level of single microstructural features.

## Simulation model for thermo-elastic material characteristics

The printing process is carried out with a material that has a higher coefficient of thermal expansion than many other solid materials (such as steel). Likewise, the thematic material values such as thermal conductivity and specific heat capacity are strongly temperature-dependent. Especially in the melting temperature range, abrupt changes occur. As a result, a time-dependent temperature and deformation field occurs during the layer-by-layer buildup of the printed part. This leads to shrinkage and thermal residual stresses, especially during cool-down. The result is that the printed part is smaller than the initial CAD model (thermally deformed) if there is no compensation for shrinkage. To account for the temperature-dependent material data in the simulation model, they are implemented as tabular material parameters as a function of temperature. The temperature range is 22 °C (room temperature) to 160 °C (printing temperature).

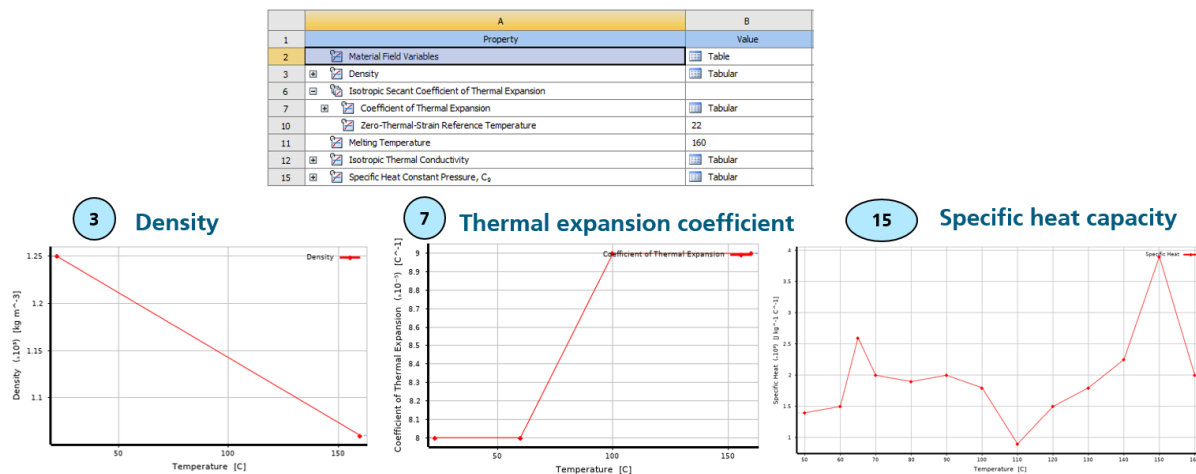
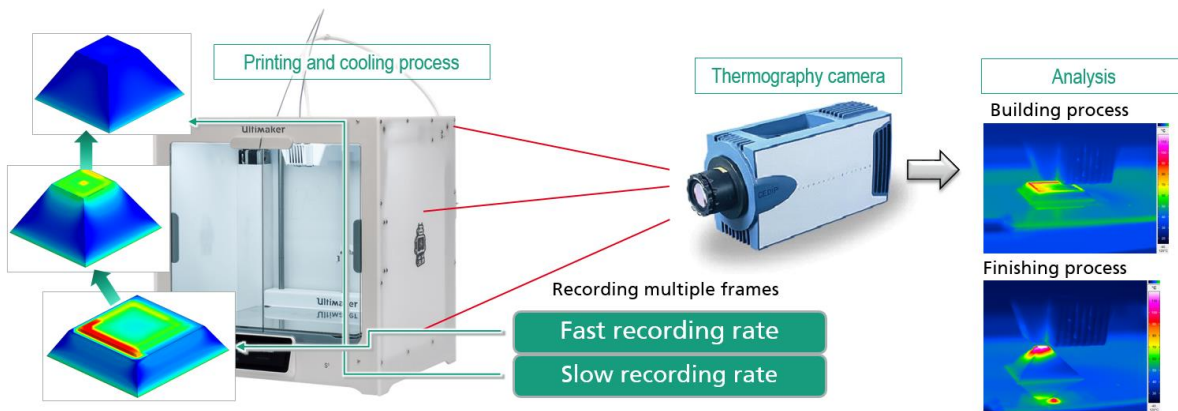


Figure 86: Overview of temperature-dependent thermal material properties for the material PLA

## Simulation of thermal deviation during the AM process of forming counter tool

The workpiece is built up in layers, with each layer being fed at a constant rate in the Z direction (layer height). In the process, the molten material PLA (approx. 160 °C) is applied along a defined path (G-code) and at a defined speed. As soon as the liquid material leaves the nozzle, it cools down very quickly as a result of convection with the cold room atmosphere and solidifies. However, residual heat still remains in the component, since a certain time is required for cooling due to the heat capacity and the inertia of heat conduction. With each further layer applied, additional heat is brought into the component by the newly applied material. For this reason, the heat (and thus the highest temperature) in solids accumulates preferentially in the center of the body. After the printing process, it takes several minutes for the component to cool down completely, since the heat escapes only slowly from the center of the body due to the sluggish thermal conduction. In order to be able to simulate this behavior in a time-resolved manner, the DED simulation approach is used, in which the structure of the workpiece is built up using activated volume elements of the FEM mesh. In addition, convective boundary conditions are applied to describe the cooling behavior. In the first simulation step, the temperature field is calculated for each time step.



**Figure 87: Analysis of the temperature field during the printing process**

A verification of the simulation model and the optimization of the boundary conditions is performed with the help of thermographic images by comparing the recorded temperature field with the simulation.

In the second simulation step, the mechanical deformation is calculated. For this purpose, a static-mechanical calculation is performed for each time step. The result is the displacements at selected points and the shrinkage dimension.

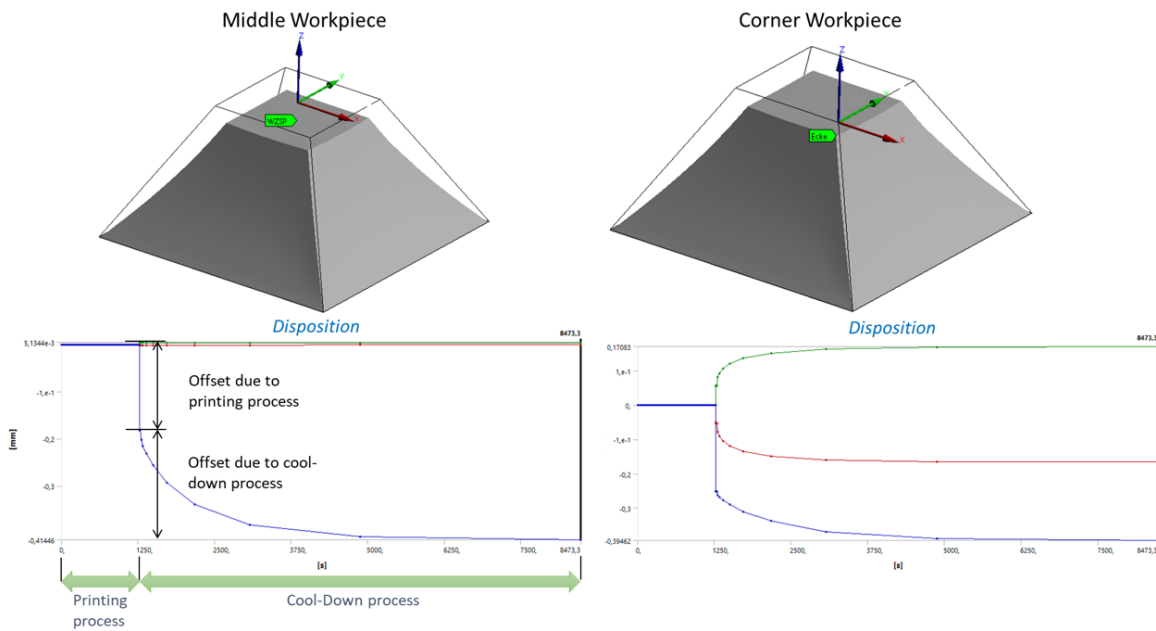


**Figure 88: Representation of the shrinkage dimension after cooling (strongly enlarged)**

For the example workpiece with a height of 25 mm, the maximum shrinkage is 0.4 mm. This displacement is later included in the overall balance as a thermo-elastic workpiece error due to the printing process.

## Simulation der mechanischen und thermischen Verlagerung an der Maschine

There are two possible types of errors in the machine:

1. the mechanical error due to the process forces (forming process)

## 2. the thermal error of the machine due to heating.

The components of the individual errors are calculated with the help of a static-mechanical and a thermo-elastic FEM simulation. The entire machine is meshed from a reduced CAD model using solid volume elements.

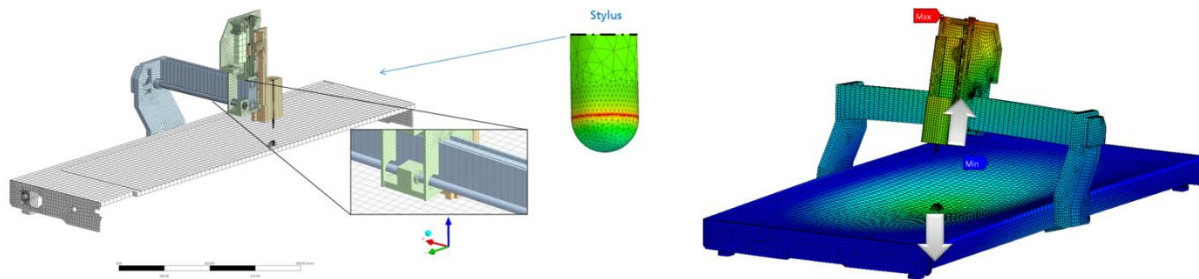


**Figure 89: Machine model as FE mesh and visualization of the deformation field (highly enlarged)**

The purpose of the calculation is to determine the displacement on the tool side of the spindle (Tool Center Point, TCP) and the workpiece side on the table. The relative total error results from the sum of the two portions TCP and workpiece. For the deformation of the machine structure, a forming force is assumed at the stylus, which also applies in the opposite direction at the workpiece. For the calculation, different machine positions are considered and a kind of characteristic map is created for the workspace.

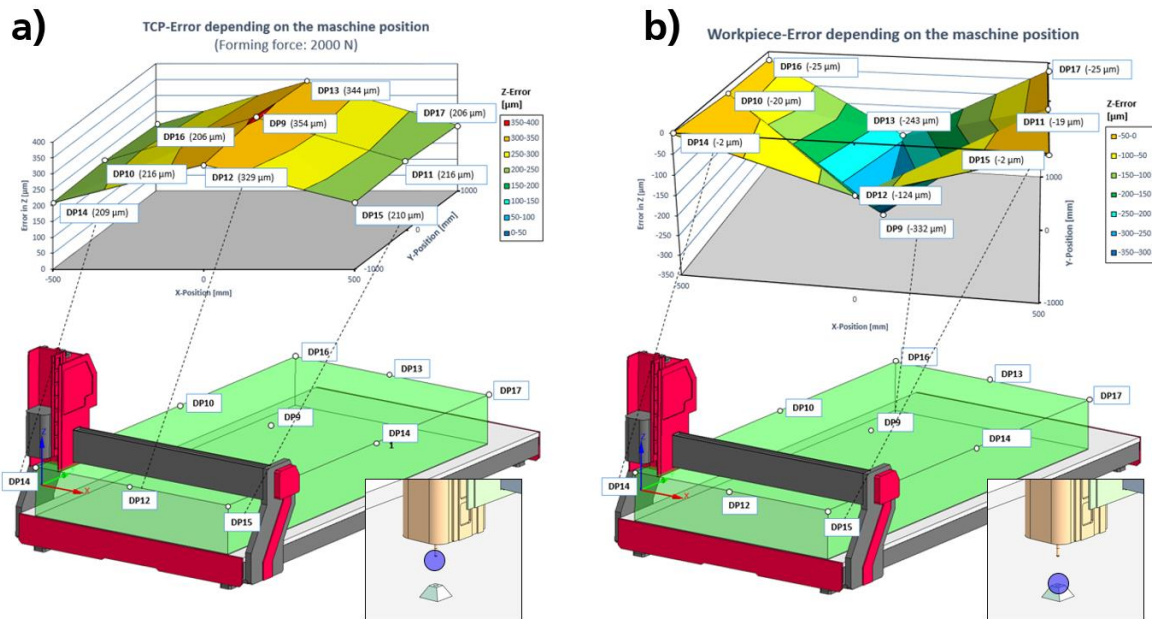


**Figure 90: Absolute displacements of the tool and the workpiece depending on the axis positions**

For this purpose, 27 grid points were defined in the workspace to represent the entire workspace. Intermediate values can be interpolated with the help of the grid points.

In the next simulation, the thermo-elastic behavior of the machine is investigated. The cause for the heating of the machine is the friction on linear guides, in bearings and heat loss from motors and motor spindle. These influences have the main part of the heating in the whole machine.

Transient thermal behavior (Warm-up Process):

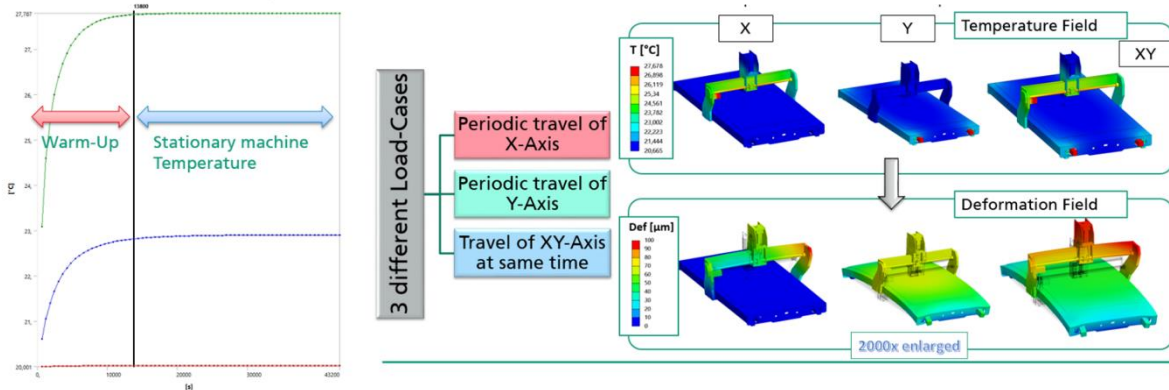


Figure 91: Thermal deformation of the machine due to internal heat influences

The periodic movement of the axes was considered as a load case, whereby a temperature response occurs over time that reaches a steady-state condition after a sufficiently long time. The evaluation of the displacements is analogous to the mechanical analysis.

### Deduction of optimal manufacturing strategies

With the help of the simulations, the process can be optimized and errors on the workpiece can be minimized by taking the individual sources of error into account during the process planning.

In contrast to the error proportions previously described in the individual chapters, the total error results from the addition of all individual error components.

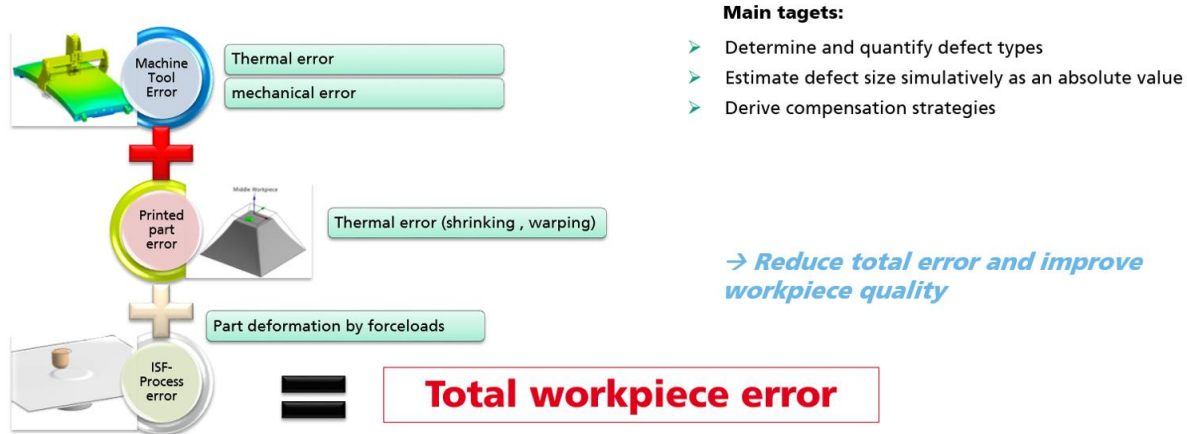


Figure 92: General overview of possible sources of errors

Process optimization is primarily about minimizing the individual fault components. In the case of the machine, for example, a high overall rigidity and a thermally stable design with a powerful cooling concept can be a possible solution. To reduce the shrinkage of the workpiece, the consideration of the shrinkage dimension can be done as a geometric overlay in the CAD layer. A methodology was developed in this project in which the previously calculated deformation field is added as an offset to the geometry and exported as a new solid, replacing the old CAD model.

## 7.6 WP6: Integration of developed technologies and iterative optimization of developed machine tool system and process technologies

### Integration and optimization of extruder technology into demonstrator system

The extruder technology has various methods for integrations. Either, the machine is capable of directly driving additional stepper or servo motors from its CNC control board, or it needs a translating interface to drive the motor from outside signals. The system was conceived at Sirris with modularity and adaptability in mind so it could quickly be transferred to other equipment. A microcontroller receives a signal (analog, digital, ethernet) and processes it to a speed setpoint as well as generates the required signals for the extruder.

This interface is based around common Arduino boards, programmed in barebone C.



**Figure 93 : Control scheme of the pellet extruder**

It is good to note that this choice of a microcontroller was driven by the need for Sirris to gradually expand the system and add functionalities (sensors, pellet feeders, cloud monitoring) and that the extrusion logic alone would be better suited to FPGA devices.

For CNC machines running Mach3 or Mach4 interfaces, a plugin is freely available to read, parse and execute 3DPrinter g-codes. The extruder axis can then be swapped for the pellet extruder, and given that the correct parameters are entered in the plugin, the extruder can be implemented rather seamlessly into the CNC framework.

The extruder planned to be mounted on the machine was delayed numerous times from the manufacturer at the end of the project, as such, relevant information about implementing the functions and interfaces were given to the partners for a later implementation.

### Integration and optimization of monitoring system into demonstrator

The monitoring technologies were integrated and tested in a machine tool at IWU as shown in Figure 94. An LED and the battery are attached to the forming tool. The sensors are clamped and tilted to enlarge the area where the LED is not hidden by the sheet clamping frame. A cardboard housing reduces the influence of the bright manufacturing environment. Basic tests, where the LED is moved laterally to the sensor, calibration measurements and measurements during a forming process with and without sheet were carried out.

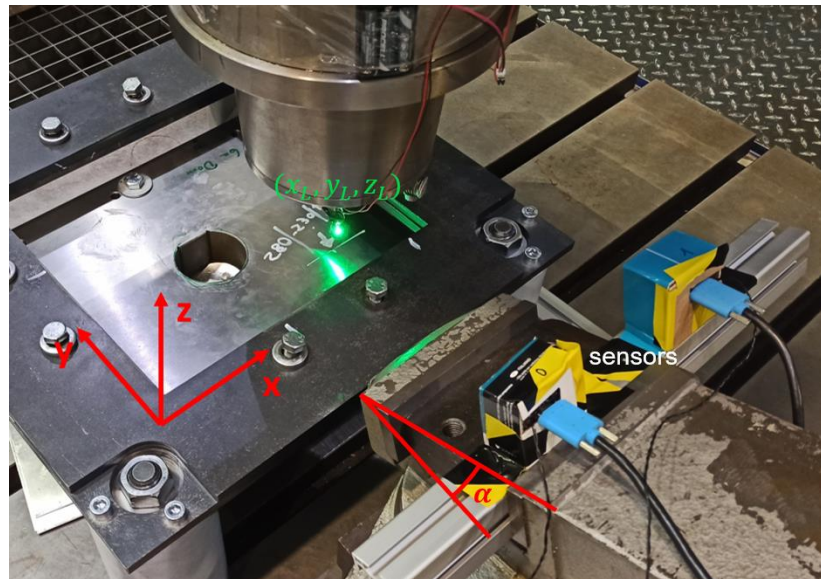


**Figure 94: Experimental setup for tool monitoring in a machine tool at IWU**

In the first experiment, the LED was moved stepwise (step size is 500  $\mu\text{m}$ ) laterally to the sensor in various lines. As shown in Figure 95, the mean lateral shadow position shift  $\overline{\Delta\xi_i}$  depends on position of the line, where the LED is moved. This means that in a tilted setup, the z-position of the LED needs to be integrated in the evaluation, if a vertical grated mask is used. For this purpose, the evaluation algorithms were further developed in order to calibrate the sensors and calculate the LED position in this setup. In future experiments, a mask that contains absolute and two-dimensional features could be installed alternatively. The optimization of the mask is mentioned in task 2.4.

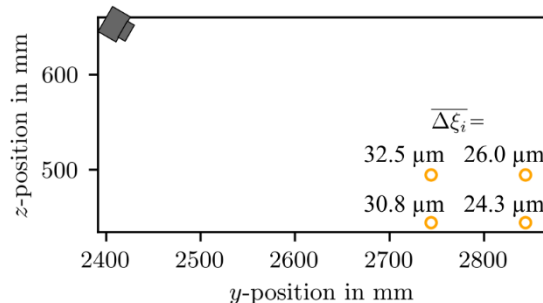


**Figure 95: Principle measurement setup to investigate the behavior of tilted sensors. The orange circles show the  $(y, z)$ -positions where the tool is moved in  $x$ -direction.**

Furthermore, the measurement system was tested during an incremental sheet forming process which is shown in Figure 96. In these experiments, the data of the draw-wire sensor was successfully used to associate the relative data of the tool monitoring system to the absolute tool position. The measured positions, that were taken while the tool has travelled once around the inner circle, are shown in Figure 97 in comparison to the defined reference positions. A systematic error occurs between the measured data and the reference data in the  $y$ -position component. It is assumed that the sources of the systematic error will be known so that the systematic error can be corrected. After the correction of the measured positions are close to the reference positions. The radius of a circle fitted to the measured position deviates 125  $\mu\text{m}$  from the reference radius. Using the new mask and perpendicular sensors, the deviation should be reduced.

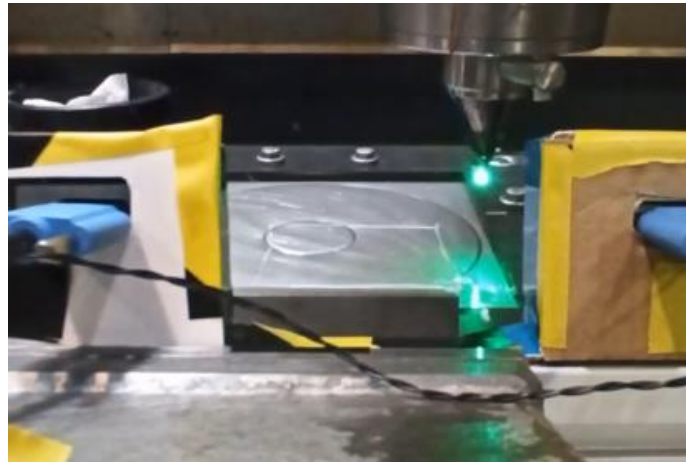


**Figure 96:** Partially formed sheet in an incremental sheet forming process during which the tool tip position was measured.

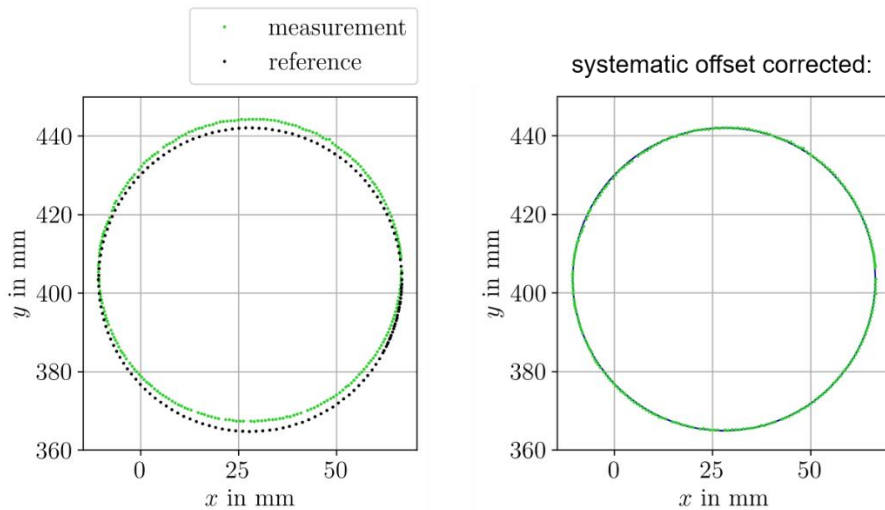


**Figure 97:** Results of the measurement using shadow imaging sensors during the incremental sheet forming process. The initial measurement data show a systematic deviation of the y-position (left) that are corrected subsequently (right).

## 7.7 WP7: Verification on real components

### Counter tools for studies on planes

Special consideration must be given to planes which have not been built up in the direction of compression. Depending on the material and forming depth, wall angles between  $45^\circ$  and  $60^\circ$  are possible with the ISF. Since the layers of the counter tool were built up in the z-direction and the load is not in the layer direction, there is a shear effect on inclined surfaces due to the horizontally occurring force  $F_h$  (Figure 98). The stylus could shear the upper layer from the layer below. In addition, the force  $F_v$  occurs in the z-direction during forming. This could cause the counter tool to be compressed by the low filling factor.

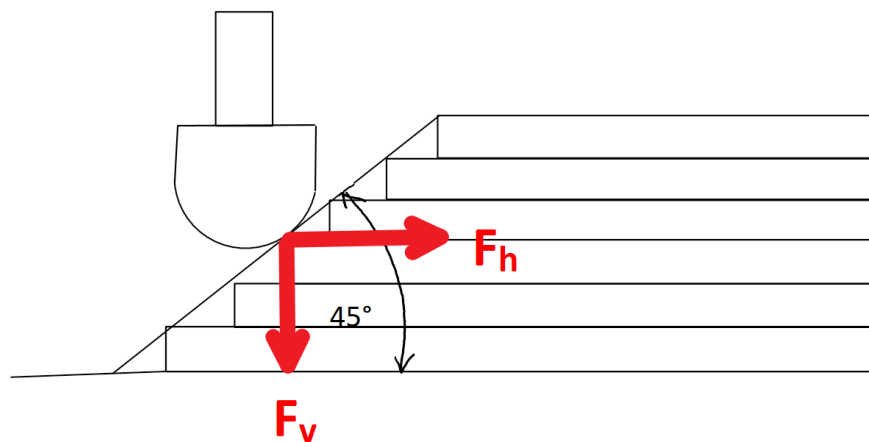


**Figure 98: Force flow at the counter tool surface**

To study the strength of a counter tool against the shear effect and other failure modes, two different counter tools were designed and printed. A truncated pyramid was chosen to perform the test on flat, inclined surfaces. This is very often found as a test geometry in ISF. The truncated pyramid has a wall angle of  $45^\circ$  and a base area of  $125 \times 125 \text{ mm}^2$ . The forming depth is 50 mm. This counter tool is a fully supporting counter tool, i.e. the sheet is in constant contact with the counter tool and is not only supported at the initial height. The truncated pyramid shown in Figure 99 is also still being examined at the corners and edges.

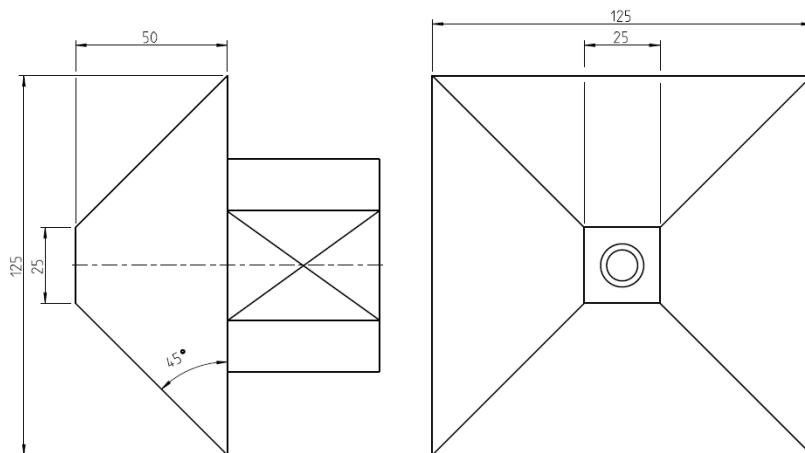


**Figure 99: Dimensions of the truncated pyramid**

The second geometry is a cone. Here, a convex curved surface can be examined. This is closer to the forming of free-form surfaces than the truncated pyramid and therefore allows a statement to be made regarding the process limits. The maximum diameter of the cone is 125 mm. The forming depth is also 50 mm. The cone has a diameter of 25 mm at the upper end. This also results in a wall angle of  $45^\circ$  for this counter tool. Figure 100 shows the cone with the blunted upper end. Accordingly, this counter tool is a truncated cone.

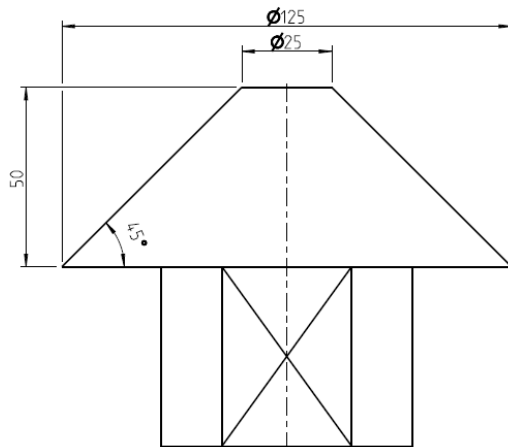


Figure 100: Dimensions of cone geometry

### Counter tools for studies on right-angled radii and edges

The 3D-printed counter tools can have different radii, which are to be reshaped. To study the accuracy of a radius, different radii have to be tested. On particularly small radii, the counter tool could also be damaged by the shear stress. In order to study a radius that extends around the entire counter tool, the counter tool shown in Figure 101 was designed and printed. This male is cylindrical and has a diameter of 70 mm. The tested radius of the counter tool is thus 35 mm. The height of the cylinder is 50 mm. If formed, this counter tool would only be a partially supporting counter tool, since 90° wall angles cannot be formed with the ISF.

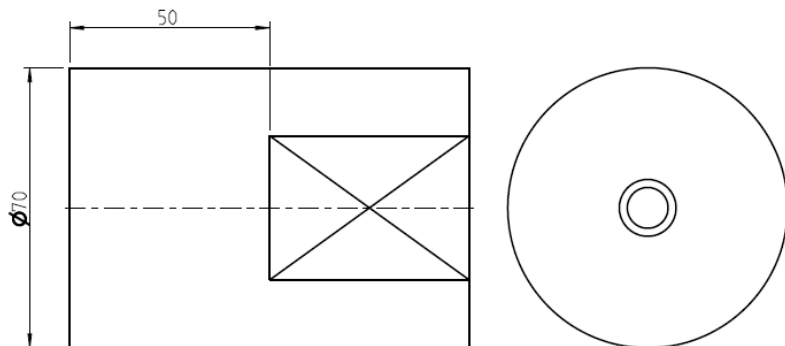


Figure 101: Dimensions of the cylinder

In order to test various other radii, two more counter tools were developed and printed. The first counter tool is a rectangle with rounded corners. The corners have radii of 1 mm, 5 mm, 7.5 mm and 10 mm. The effects of the different radii on the counter tool are to be tested on this. The base area of the counter tool is 60 x 36 mm<sup>2</sup> (Figure 102). This counter tool is also only a partially supporting counter tool, since a wall angle of 90° cannot be formed here either.

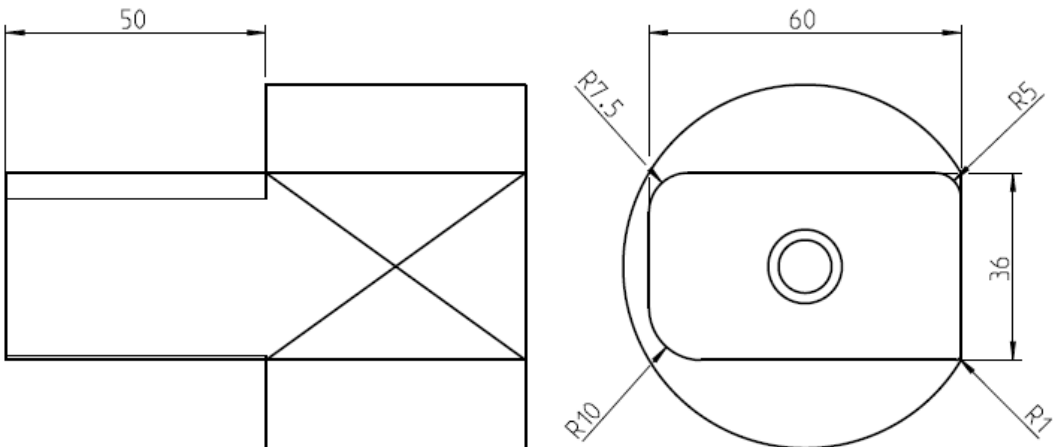


Figure 102: Dimensions of the quadrilateral

The second counter tool is a triangle, which also has rounded corners. The sides are each at an angle of  $60^\circ$  to each other. The rounded corners have radii of 1 mm, 5 mm and 7.5 mm. Since the sides converge at an acute angle, corners are formed which are particularly interesting for Section 4.3. With the radii, this also poses a greater risk of damaging the counter tool. This counter tool is also only a partial support.

### Counter tool for studies on corners

Since corners in counter tools have to absorb the entire forces at a very small point, there is a great risk of destruction or damage to the counter tool at these points. Shear stresses can quickly exceed a tolerable maximum at corners. In order to study different corners, the truncated pyramid described in Section 4.1 is to be manufactured without radii. This results in very tapered corners at the lower ends of the pyramid edges and less tapered corners at the upper ends. This can already provide a rough estimate of how well 3D-printed counter tools will hold at corners.

In order to be able to assess other corners, particular attention is paid to the behavior of the counter tool with the triangular shape (Figure 103), as described in Chapter 4.2. This may result in limits for the size of radii at certain corners. The corners have an angle of  $60^\circ$ . If this angle is too small for different radii at the corners and the counter tool is damaged during forming, a further comparison can be made with the rectangular counter tool, because here the corners have an angle of  $90^\circ$ .

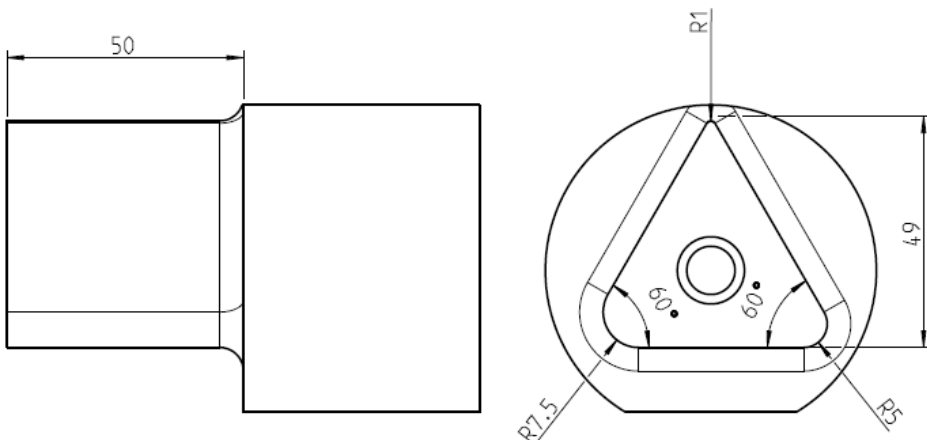


Figure 103: Dimensions of the triangle

## Test material

The test material is the soft pure aluminum

EN- AW-1050A H111. The pure aluminum exhibits sufficient plastic deformability due to its high uniform elongation of at least 22 % and is therefore suitable for basic tests. This material has a high formability. The tensile strength  $R_m$  is low at 65 MPa. This is important for investigating whether sheets can be formed at all with such a low filling factor in counterforming. The material used also has a low yield strength  $R_{p0.2}$  of 20 MPa. The initial sheet thickness  $s_0$  for the geometries is 1.2 mm.

## Test geometries

Due to the frame not moving in the z-direction, the sheet must be formed inside and outside. Therefore, the sheet is formed more than considered later in the evaluation. Using the truncated pyramid geometry as an example, Figure 104 shows how the sheet looks after forming. However, only the inner area marked in red is relevant for the later evaluation. Furthermore, no trimming is performed before evaluation.

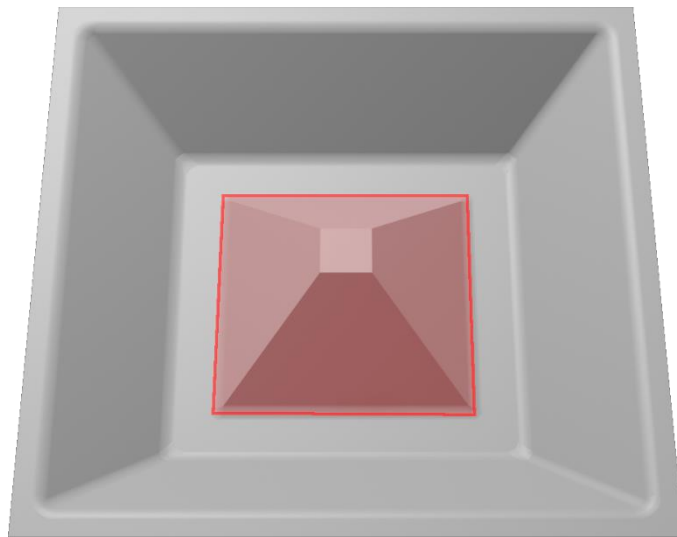


**Figure 104:** Plate after forming with truncated pyramid geometry (area marked in red relevant for evaluation)

In order to study different surfaces for their behavior during forming, the truncated pyramid and the truncated cone (cone) are used. In the case of the cone, the behavior of the lateral surface is mainly investigated, although investigations of the behavior at the upper edge are also carried out. Figure 105 shows the final geometry of the sheet after forming over the cone. Forming takes place over a 45° angle from an upper diameter of 25 mm to a diameter of 125 mm after a forming depth of 50 mm.

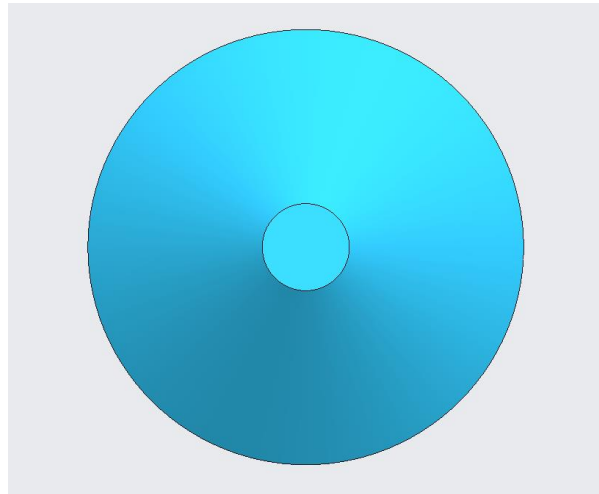


**Figure 105: Test geometry of the cone**

In the case of the truncated pyramid, the corners and edges are also examined in addition to the surfaces. This test geometry can therefore be used in a variety of ways for different parameters. The square truncated pyramid has an edge length of 125 mm (Figure 106). At the upper end, the edges are still 25 mm long. The forming also takes place to a depth of 50 mm and at a wall angle of 45°.

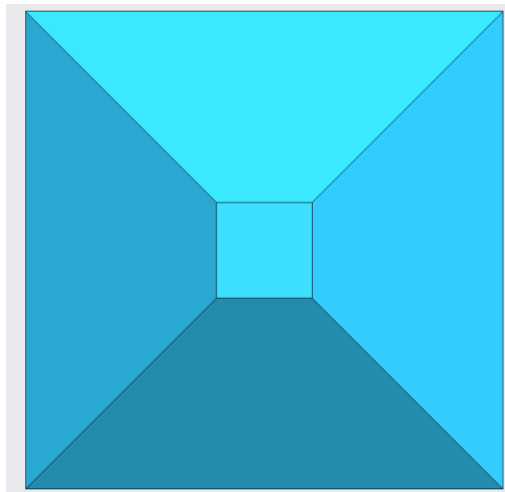


**Figure 106: Test geometry for the truncated pyramid**

Another test geometry is the cylinder. This is suitable for investigating radii and edges. The radius of the circumferential edge is 35 mm (Figure 107). Since the male part of the test geometry is only partially supporting, the behavior of the edges can also be investigated. In this case, the sheet is also formed to a depth of 50 mm. The wall angle to be formed is also 45° here.



Figure 107: Test geometry for the cylindrical counter tool

For the investigation of corners and radii, this rectangular test geometry with different radii at the corners was selected. This geometry with a quadrilateral as base surface is also only partially supported by the quadrilateral counter tool (Figure 108).

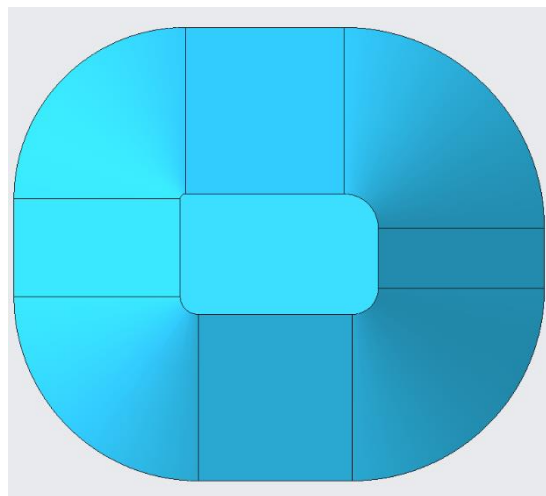
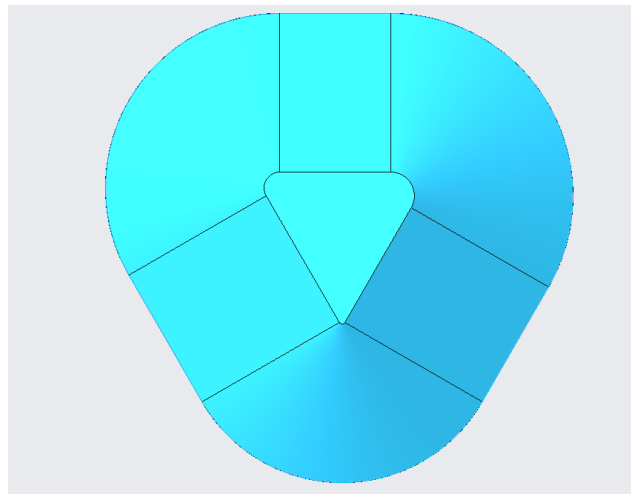


Figure 108: Test geometry for the quadrilateral counter tool

For further investigation of corners and radii, a test geometry with more acute corner angles was selected. The base of the test geometry is an equilateral triangle with different radii at the corners (Figure 109), as described in Chapter 4.3. The sheet is formed at a 45° angle above it. Here, too, the counter tool has only a partially supporting effect. Therefore, the wear at the corners and edges of the counter tool and the effects on the sheet are of particular interest.



**Figure 109: Test geometry for the triangular counter tool**

### Process strategy for forming

For the generation of tool paths (NC program) several ways are available. In the context of this work, the following variant was concentrated on. For the tool path creation of the stylus, the geometry was created in the CAD program as a surface model. The PRT file created in Creo Parametric was then converted into a neutral IGES format. This neutral interface allows the geometry to be integrated into the CAM program GIBcam.

A "contour milling program" can then be used to create a tool path in which the stylus traverses the contour to be produced in z-parallel steps. The tool moves counterclockwise in the x- and y-directions until a plane is formed around the counter tool. The stylus then forms the sheet at the outer edge on the same z-plane in a clockwise direction, since the clamping frame is immobile. This is followed by an infeed in the z-direction, where again the inner part is formed first.

For the test geometry of the truncated pyramid, the course of the paths and the position of the sheet in the clamping frame are shown schematically in Figure 110 and Figure 111. To take account of the rolling direction of the plate, it is always clamped so that the x-axis is parallel to this direction. The infeed during the tests is 0.5 mm per increment in the z-direction and the feed rate of the machine was set to 10 m/min.

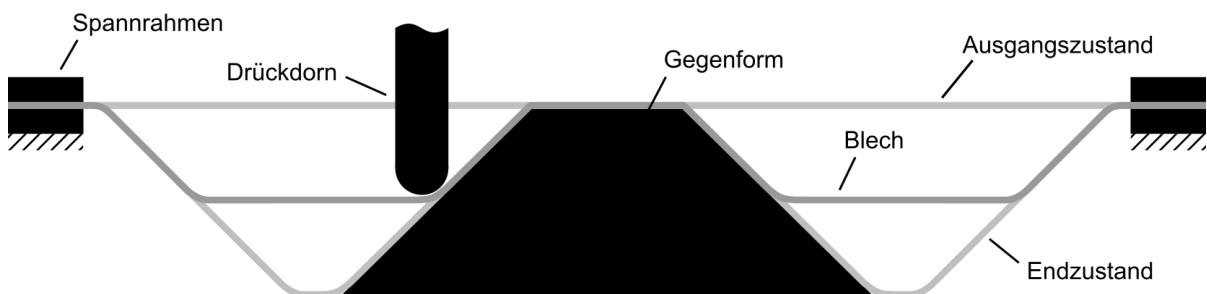


**Figure 110: Process strategy from the side view**

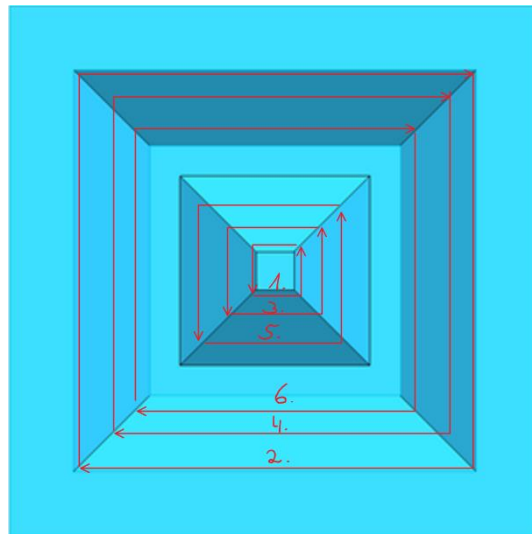


Figure 111: Process strategy for forming.

### Test procedure

For the evaluation of the 3D-printed counter tools, five aluminum sheets are formed per counter tool. The counter tools are measured after printing, the first, the third and the fifth test and evaluated later. The formed sheets will be measured in the same trials. The parameters will be the same for all trials so that the trials are comparable. The tests are all carried out with a stylus with a diameter of 30 mm and on the clamping frame described in Chapter 5.1.3. The initial sheets are 350 x 350 mm<sup>2</sup> with a sheet thickness of 1.2 mm. The infeed increment is 0.5 mm. The forming process requires 2 passes per plane. To avoid excessive twisting, the outer track is run clockwise and the inner track counterclockwise.

After each test, the sheet is cleaned with degreasing spray and cleaning cloths. After that, for each first test for a counter tool, it is exchanged for another one. Afterwards, the counter tools and sheets already worn are measured with the Comet 6 from Steinbichler. For this purpose, a chalk layer is applied to the plates or the counter tools. After measuring, two further tests are carried out with each counter tool before they are measured again together with the corresponding sheets.

The forming time associated with each part is shown in Table 1.

Table 1: Counter tools and the associated forming time

Counter tool	Forming time
Cone	28:52 min
Truncated pyramid	35:26 min
Cylinder	30:45 min
Quadrilateral	30:49 min
Triangle	28:58 min

### Systematization and evaluation of results

#### Evaluation of the counter tools and formed sheets

All five counter tools were measured directly after printing and dissolution of the support structure. Since the male parts were all printed without oversize, it was clear from the outset that small deviations in shape may occur in places due to the shrinkage process. In the following, each counter tool is examined individually and the shape deviations are pointed out. In addition, the geometry changes after the first, third and fifth test are explained for each counter tool.

On all sheets, a radius will be visible on the bottom edge. This is due to the tool radius, which is too large to approach the lowest point in the sheet. In addition, the sheets will usually show a decreasing deviation in the lowest forming area. This is due to the fact that the sheets were not trimmed after the forming process. The material around this area therefore hinders greater springback there.

## **Cone**

### **Cone male after printing**

The cone illustrates the problem of shrinkage, since it is undersized everywhere on the shell surface. At one point, the shrinkage is somewhat more pronounced, as shown by the blue colored area on the false color image in Figure 112. The three dots on the surface are due to markers used to merge the measurements.

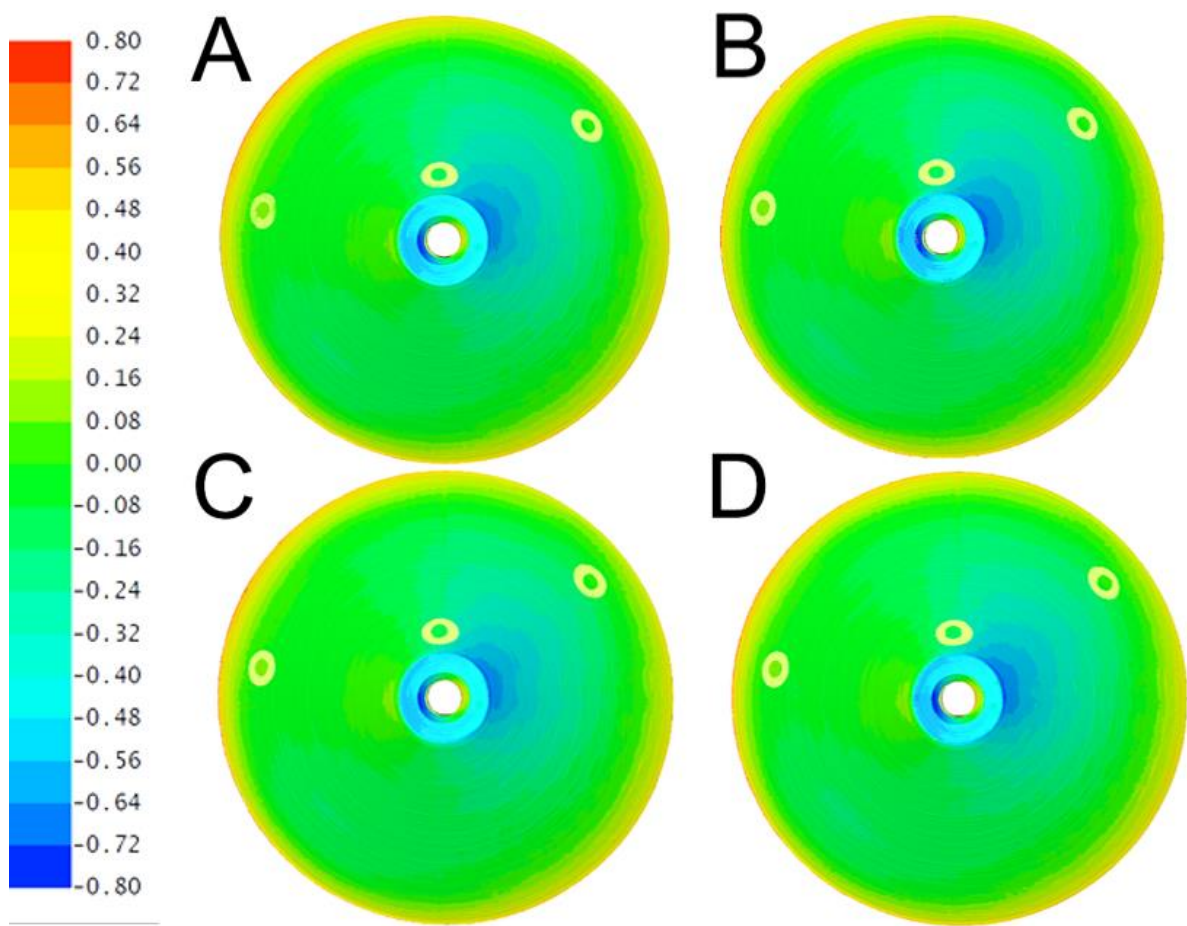


**Figure 112: Cone male after 3D printing; B: Cone male after the first attempt; C: Cone male after the third attempt; D: Tapered male after the fifth forming attempt.**

The bottom edge of the cone is orange to red in the false color image. This shows that the lower edges bulge upward by up to 0.6 mm. In some areas, a bulge forms at the edge upward in the z-direction. The lower surface with which the cone rests on the clamping is not straight, but moves outward in the z-direction away from the nominal geometry. Since the counter tool is very thin at the outer edge, there is a possibility that this will be pressed onto the clamping plate by the stylus and the sheet during forming and that the effects on the sheet will not be noticeable as a result. However, this could also already be in the area which the stylus cannot approach due to the tool radius.

After the first forming test, the edge at the most shrunken point of the tapered male part (Figure 112B) shows that the load is highest at the upper edges, since the deviation there after the first forming is approx. 0.1 mm greater than before this forming.

At the lower edge, there are no changes from the initial state. In addition, the counter tool can be used for further tests without any problems.

On the sheet after the first test, it can be seen that there is a bulge outward in the sheet at opposing areas (Figure 113A). These deviations are in the range of about 2 mm from the nominal geometry. The lines on the upper edge of the sheet were only used to orient the actual geometry to the nominal geometry. This also serves to ensure comparability between the measurements, since the part should be rotationally symmetrical.

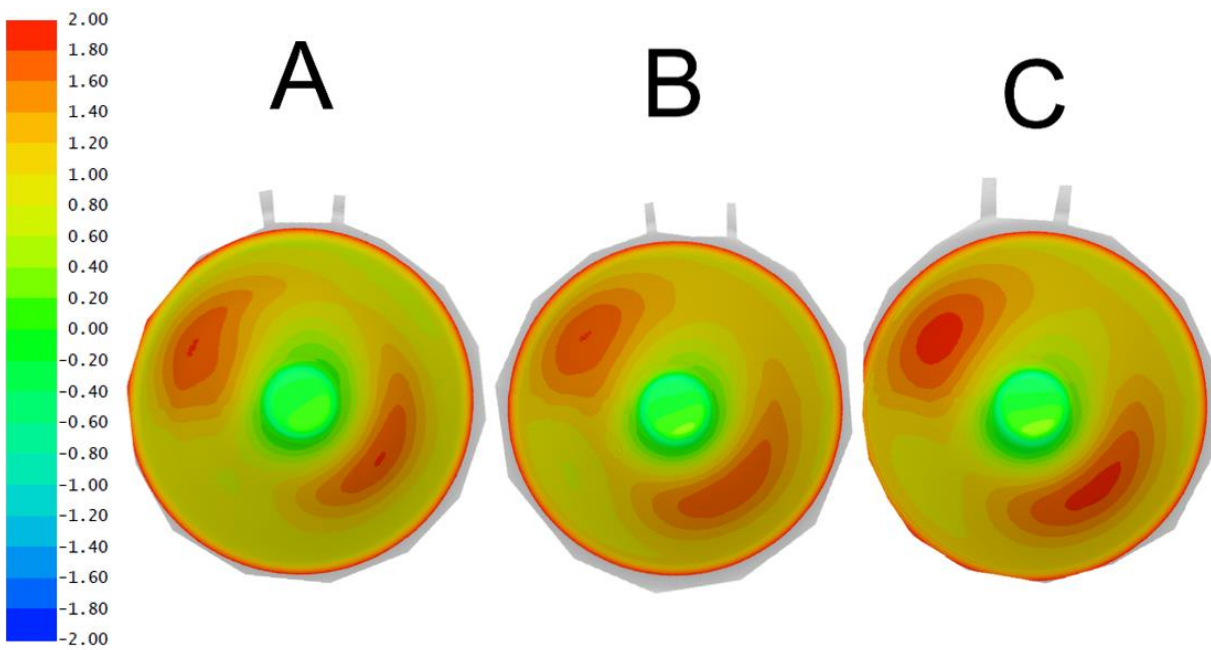


**Figure 113: Cone plate of the first test; B: Cone plate of the third test; C: Cone plate of the fifth test**

This picture also clearly shows that the upper part of the cone deviates from the nominal geometry by only approx. 0.2 - 0.3 mm and by up to 1.9 mm towards the bottom.

This counter counter tool shows no change after the second and third test (Figure 112C). It is still completely intact and can be used for further tests.

Since no changes could be seen on the counter tool, the sheet after the third test is also similar to the sheet after the first test (Figure 113B).

Even after the fifth test, no changes can be seen on the cone counter tool (Figure 112D). The counter tool is intact and after the tests still almost in the same condition as after printing.

Although the counter tool has not changed in measurement after the fifth forming test, the sheet shows strong changes in the areas of greatest deviation on the oblique surface (Figure 113C). No changes can be seen on the upper surface of the cone and on the circumferential edge compared to the measurements after the third forming test.

After the first test, a deformation of approx. 0.1 mm can be seen on the upper edge of the male part. The surfaces of the counter tool remain completely unchanged and therefore this geometry is suitable as a counterform for the ISF.

## Pyramid counter tool

### Truncated pyramid counter tool after printing

The shrinkage of the counter tool after printing can also be seen in the truncated pyramid. It is also easy to see where the cavities are located behind the surface layer, as these areas are somewhat caved in on the surface of the mantle (Figure 114A).

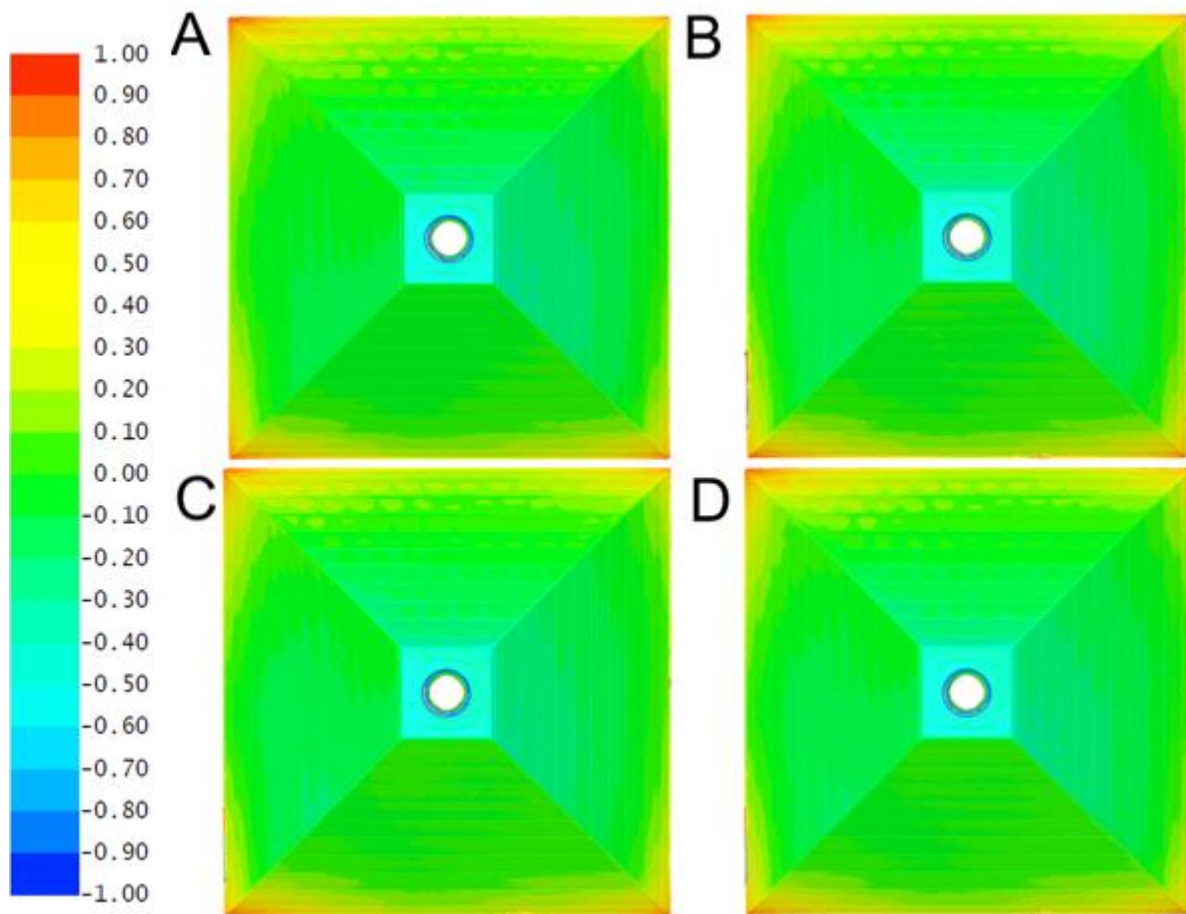


**Figure 114: Pyramidenstumpfplatze im Falschfarbenbild nach dem 3D-Druck (A), dem ersten (B), dem dritten (C) und dem fünften Versuch (D)**

In contrast to the cone, the entire lower circumferential edge of the pyramid is not curved upwards, but only the four corners. These are up to 1 mm off the nominal geometry after printing. However, since the stylus has a diameter of 30 mm, it will not be able to reshape the sheet at that point anyway. The area is not accessible for the stylus, as otherwise collisions with the base plate would occur. For this reason, the effects on the sheet metal are expected to be rather small. The lifting of the corners can also be seen particularly well in Figure 114A.

No major changes can be observed on the counter tool from before the test to after the test (Figure 114B). It is noticeable that the incidence of some areas on the upper surface appears somewhat smoothed. However, this is within a range of about 0.1 mm. In addition, all corners and edges are still intact after forming. There is also no shrinkage in the height of the truncated pyramid. After the first test, this counter tool is still completely intact and is suitable for further tests.

As with the cone plate, the deviations on the opposite sides are also greatest on this plate. These are around 1.3 mm. The deviations are highest on the inclined surfaces of the pyramid. The accuracy is best on the upper flat surface and in the upper areas of the four edges. In these areas, the deviations are not greater than 0.1 - 0.2 mm. In general, it can also be said that the springback in the lower area is lower than in the upper area of the forming. This is due to the fact that the sheets were not trimmed after forming. These deviations are evident in the false color image (Figure 115A). A bulge can also be seen at the upper edge in this figure, as

in the case of the cone sheet. This also served to align the measurement to the nominal geometry, since otherwise, due to the symmetry, the plate could not be aligned to the nominal geometry in the same way each time.

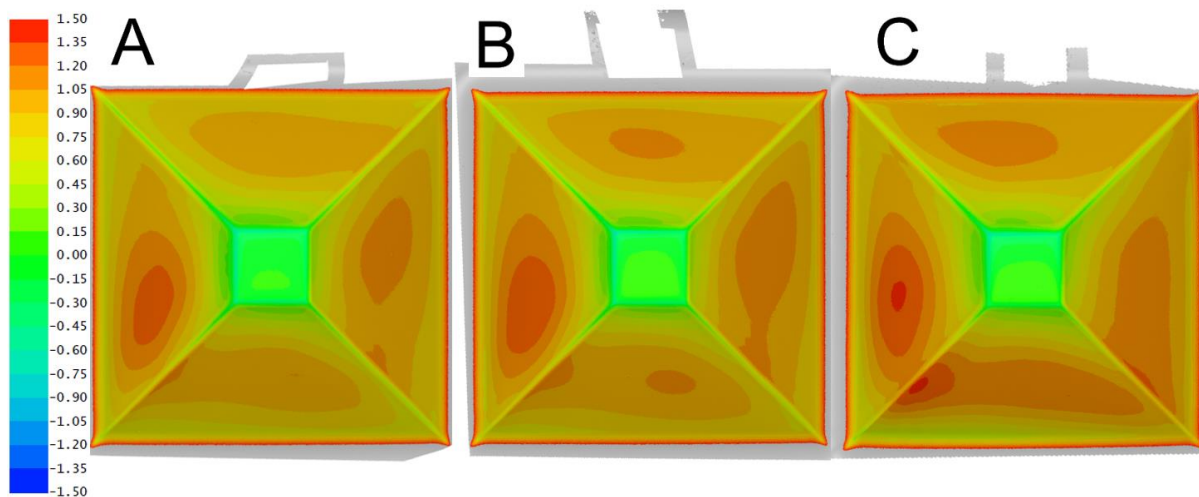


**Figure 115:** Truncated pyramid plate of the first (A), the third (B) and the fifth test (C)

In the comparative image (Figure 114C), no changes can be seen on the surfaces and the edges running obliquely downwards. Only the upper edges or corners show stronger deviations after the second and third test compared to after the first test. Since the sheet exerts the greatest pressure on the upper corners during forming, the greatest deviation is seen in these areas after the second and third forming. The corners were pressed into the part (Figure 116). The deviation increases by approx. 0.1 mm and thus amounts to 0.55 mm after forming.

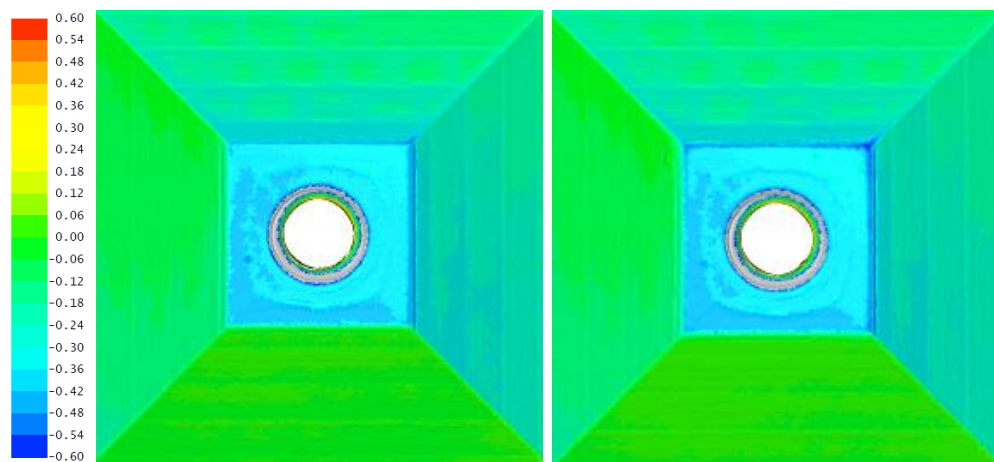


**Figure 116:** Upper surface of the pyramid butt plate after the first (left) and after the third forming operation (right)

In the plate, there are no changes at the corners after tests two and three compared to the first test. However, the deviations on the outer surfaces of the truncated pyramid become larger (Figure 115B). This can nevertheless be attributed to the depressed corners, since they cannot support the sheet as well as before during forming. As a result, it pushes the surfaces in their

center upwards more than after the first test. The deviations at these points after the third attempt are about 0.05 mm more than after the first attempt.

This counter tool remains unchanged from before on the surfaces, the oblique edges and the lower corners after the fifth test. The only minimal deviation can be seen at the upper corners, but even this deformation is in the range of less than 0.1 mm. Also the comparison from after the pressure to after the fifth test shows that the counter tool has deformed only at the upper corners by about 0.2 - 0.3 mm during the tests (Figure 117).

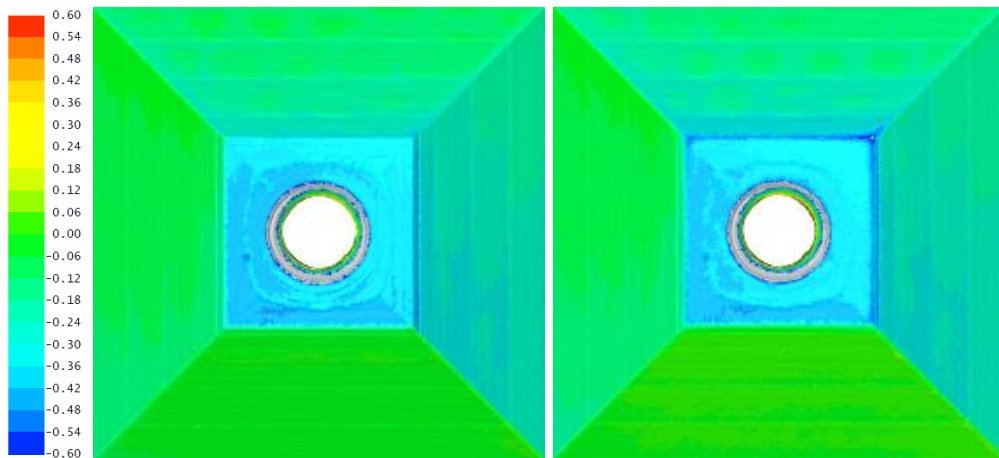


**Figure 117:** Upper surface of the truncated pyramid counter tool after 3D printing (left) and after the fifth test (right).

The measurement on the plate of the fifth forming test shows that the deviations in the plate increase on the four oblique side surfaces (Figure 115C). These nominal-actual differences increase by about 0.2 mm to up to 1.6 mm in these areas. The top two edges are as before, but the bottom two edges now show deviations of 1 mm. It is also noticeable that the stylus pushes material in the direction of movement towards the edges and therefore after an edge the deviations are always greater than before the edge.

The corners on the uppermost surface are deformed or rounded by up to 0.3 mm. The oblique edges of the truncated pyramid do not change and are therefore suitable for ISF. The oblique faces also retain their shape after the forming tests. It follows that corners must be designed with a radius rather than sharp edges.

## Cylinder

The cylindrical counter tool shows only minor deviations after printing, although shrinkage can clearly be detected here as well. This shrinkage is about 0.4 mm in the z-direction. However, deviations of up to 3 mm can be seen at one point on the bottom of the counter tool, as the counter tool has partially detached from the print bed during the manufacturing process. However, this has no effect on the forming process, since the counter tool rests on the lower base plate at the lowest point. However, it can be seen on Figure 118 that an undercut of up to 0.05 mm has occurred under the edges when printing the upper surface layer.

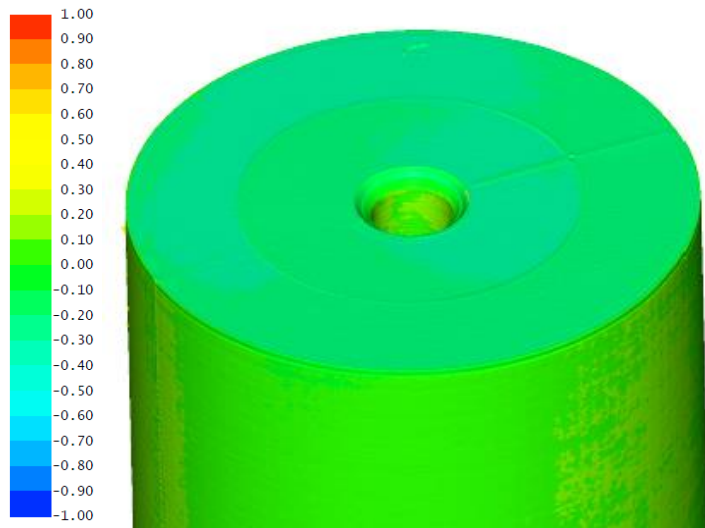


**Figure 118: Cylinder counter tool from below in the bottle color image**

Otherwise, only small adhesions can be seen on the outside of the counter tool. These arose during printing, since three counter tools were printed together and the printer has to settle between the counter tools and should not extrude any material. The post flow of the extruded material causes such buildup. However, these must be ground off so that the counter tool fits into the receptacle provided for it. The most important thing for the cylindrical male part, however, are the edges and these are only shifted downwards in the z-direction due to the shrinkage process, but otherwise the edges are only deviated from the nominal geometry by less than 0.1 mm in the x- and y-directions (Figure 119).



**Figure 119: Upper surface of the cylindrical counter tool in sectional view (section through the x-axis)**

#### Cylinder counter tool after the first test

Based on the comparison of before and after the first test, the shrinkage of the counter tool by approx. 0.1 mm can be seen in Figure 120. However, the edges of the counter tool are still intact. In all the sectional views, it can also be seen that the counter tool has been compressed by this amount and not just slightly displaced during the alignment after the measurement. However, the undercut, which was detected after the pressure, has not changed.

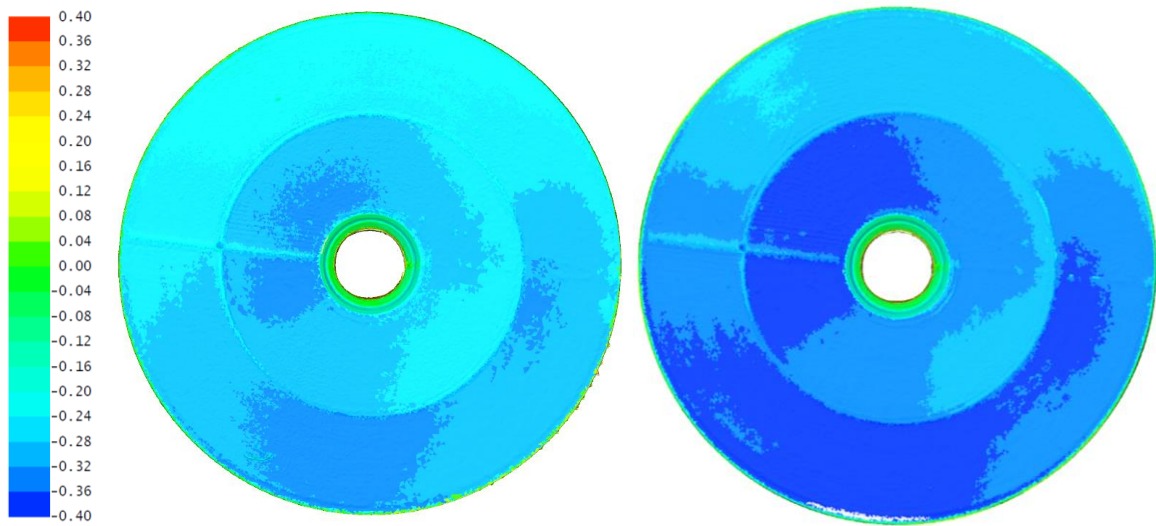


**Figure 120:** left: cone counter tool before the first test, right: cone counter tool after the first test

This geometry has similar characteristics to the cone, since  $90^\circ$  wall angle forming is not possible with the ISF. In order to be able to assign the sheets more easily, the designation as cylindrical sheet will be retained in the following.

Here, too, the largest deviations are on opposite sides

(Figure 121A). These nominal/actual differences amount to up to 1.2 mm. The edges are slightly shifted downward in the z-direction compared to the nominal value. This can be attributed to the shrinkage of the counter tool.

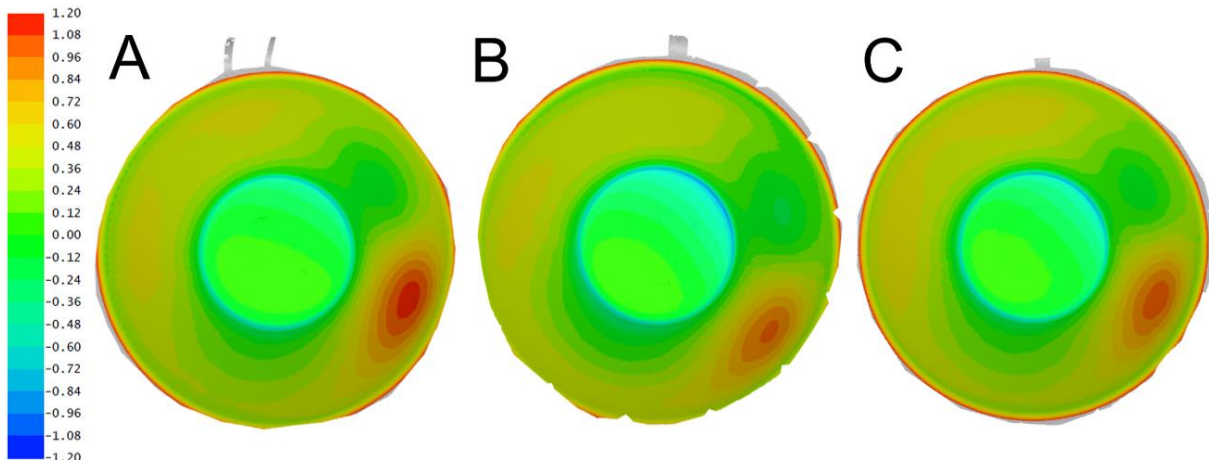


**Figure 121:** Cylinder sheet of the first (A), the third (B) and the fifth test (C)

On this counter form, it can be seen in the sectional view in the yz plane that the circumferential edge is beginning to give way. The initially sharp edge shows a clear deformation after the third forming test. This has been rounded off and the outer shell layer on the side of the counter tool is further depressed by the forces at this point, thus increasing the undercut to approx. 0.1 mm.

On this plate, the deformation of the cylinder counter tool after the third test is quite clear. The deviation at the upper circumferential edge is increased by approx. 0.2 mm (Figure 121B). However, the largest deviation on the surface of the cylinder sheet decreases from 1.1 mm to 0.97 mm. This may be due to the process.

In this counter tool, uniform shrinkage is observed after the fifth test. The upper surface of the counter tool is completely pressed down by the sheet during forming. It can also be seen at the edge that the forces acting on the counter tool are greatest there. There, as after the third test, the sharp edges have been rounded off further and form an outward bulge to a greater extent than before. However, the change compared to the last measurement is less than 0.1 mm.

This plate shows that the deformation of the cylinder counter tool after the fifth test is only very slight (Figure 121C). The deviation at the upper circumferential edge is the same as in the third test. This reflects the results from the measurement of the counter tool. The deviation on the inclined surface is in a similar range as after the third test. This is 1.03 mm for this sheet.

On the circumferential edge at the top of the cylindrical counter tool, the rounding of edges is even more apparent than in the previous geometries. It can be concluded from this that rounding must also be provided on edges which run over a 35 mm radius.

## Square

The square counter tool is also affected by shrinkage of the PLA material after printing. This accounts for about 0.4 mm in the height of the counter tool (Figure 122).

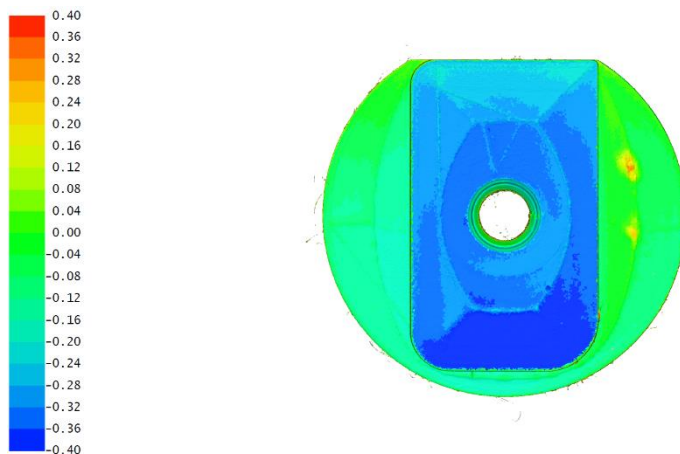


**Figure 122:** False color image of the square counter tool from above.

The edges that matter are affected by shrinkage only in height. In the spread in x- and y-direction, the edges are only less than

0.1 mm from the nominal geometry. In addition, the radii have been printed very well, so that a sharp edge can clearly be seen over which the sheets can be formed. The smallest radius of 1 mm was also printed very precisely.

As with the cylinder, adhesions can be seen on the outside of this male part in Figure 123. Here, too, these must be removed by grinding to ensure smooth insertion in the holder. Likewise, a deviation of up to 3 mm can be seen on the underside of this counter tool, which originates from the detachment of the material from the print bed during the manufacturing process. Here, too, the effects on the forming process are not considered relevant, since the counter tool rests on the lowest point at the bottom and is guided laterally through the holder.

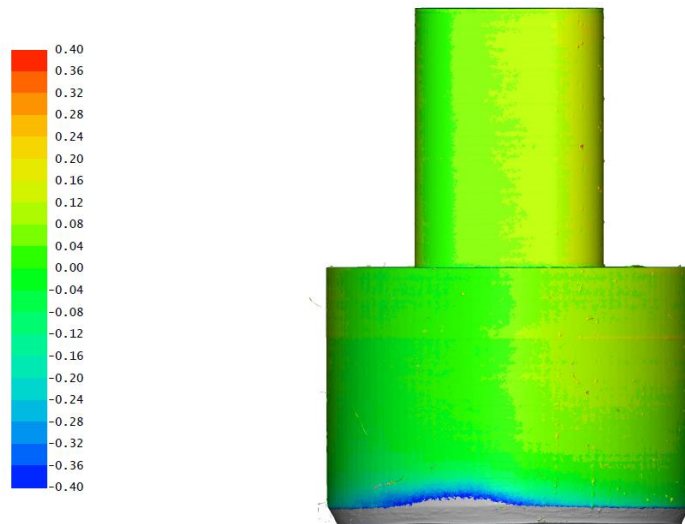


Figure 123: Adhesions on the square matrix after 3D printing

### Square counter tool after the first attempt

Like the cylinder counter tool, the counter tool exhibits shrinkage of less than 0.1 mm after the first attempt. In addition, a slight shearing of the material can be seen at the corner with the smallest radius (Figure 124). The material is still firmly bonded, but a bulge towards the outside can now be seen and the corner thus sinks downwards by approx. 0.2 - 0.3 mm.

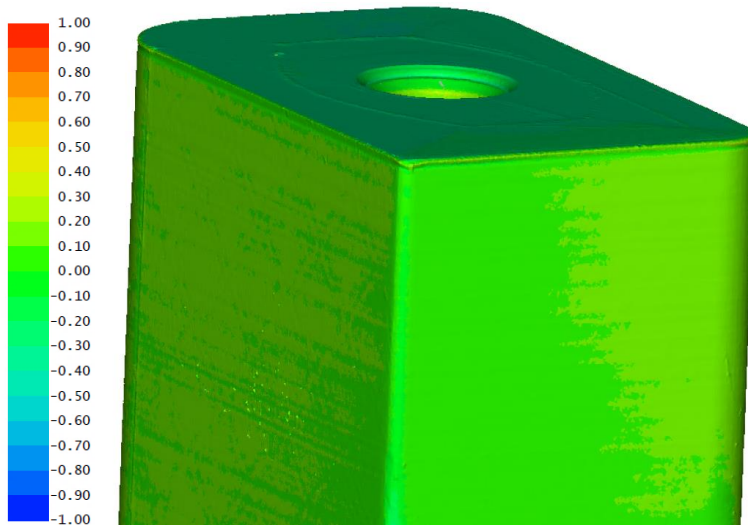


Figure 124: Shearing of the material at the corner with the smallest radius on the square plate after the first test

In this geometry, the largest deviations are on the two long sides. These deviations amount to just under 1.8 mm. Furthermore, it can be seen on the false-color image (Figure 125A) that the deviations at the corners become smaller the larger the radius. The deviation at the corner of the smallest radius is just under 1.4 mm. At the corner with the largest radius, this deviation in the sheet is only slightly more than 0.7 mm.

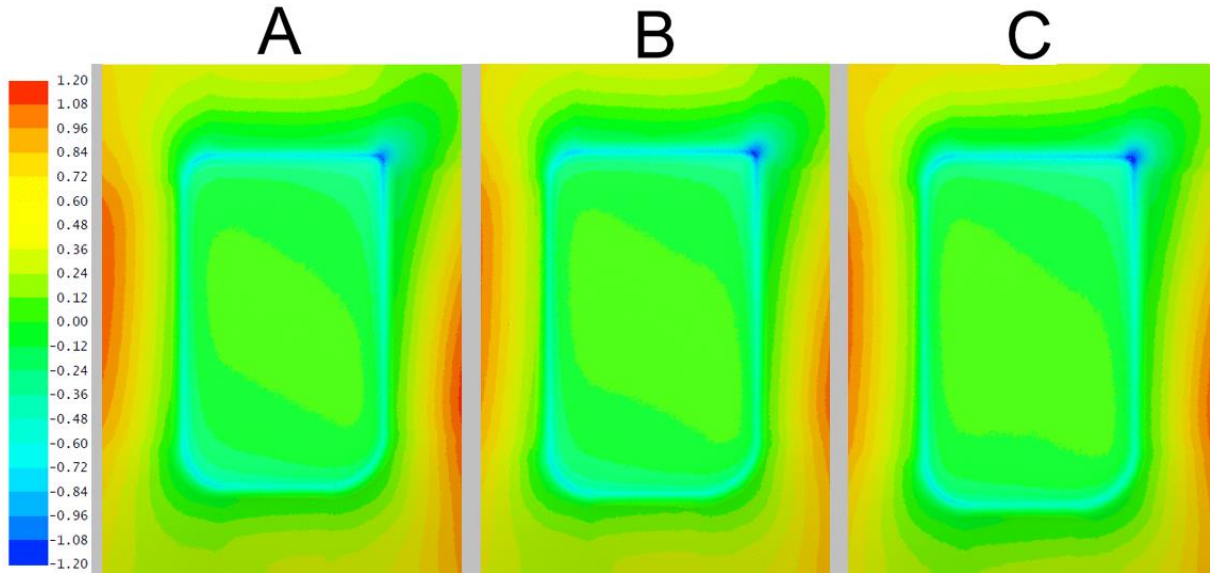


Figure 125: Upper surface of the square plate after the first (A), the third (B) and the fifth test (C)

After the third test, shearing of the material at the corner with the smallest radius can be seen on this counter tool. At this corner, the deviation from the nominal geometry is 0.8 mm. In addition, an outward bulge can be seen below this corner. This is the result of the sheared material. This phenomenon also occurs at the other three corners. However, the deviation is significantly smaller the larger the radius becomes. For example, the deviation at the 7.5 mm radius is only 0.5 mm. In addition, further shrinkage of the counter tool in the z-direction can only be detected to a very small extent of less than 0.05 mm on the evaluated false-color images.

After the third test, the deviation at the corner with the smallest radius is up to 0.2 mm larger (Figure 125B). This is due to shearing of the material at the counter tool. The outer surfaces are provided with the largest deviation on the long sides even after the third test. However, at 1.6 mm, this is 0.2 mm less than in the first test.

The square matrix shows no deviation at the corner with the smallest radius after the third test. The other corners also remain the same in terms of the nominal/actual difference. However, the edge is further rounded. The smaller the radius, the greater the shearing of the material at the edge.

The sheet shows an even more significant deviation after the fifth test than after the third test. This is particularly noticeable in the area of the smallest radius (Figure 125C), because the deviation increases by approx. 0.2 mm. This nominal-actual difference is due to the described rounding of the counter tool at the radii. Furthermore, the deviation at the oblique surfaces of the long side has increased somewhat. This is now up to 1.7 mm on one side and up to 1.45 mm on the other. In general, this deviation is slightly different for each test. Therefore, this change can be assumed to be process-related.

It can be seen from the square counter tool that corner radii of more than 5 mm are not a problem for the additively manufactured counter tool when the 90° angle between the faces is observed. However, even with such corners, the upper edges should be provided with a radius to avoid deformation of the counter tool. In addition, the larger the radius, the smaller the deviations on the counter tool.

## Triangle

The triangular counter tool behaves very similarly to the counter tool of the quadrilateral. The deviations in the z-direction due to shrinkage are up to 0.4 mm (Figure 126) and the corners are printed sharply and the radii are very accurate. The adhesions at the edges can also be ground off and the largest deviation at the bottom edge of up to 3 mm can also be neglected.

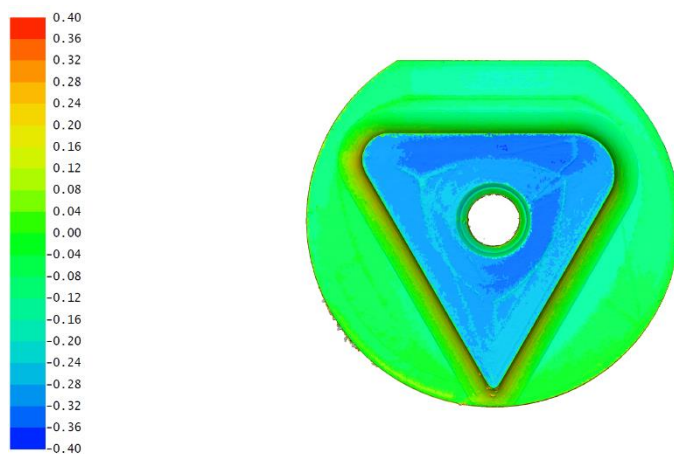
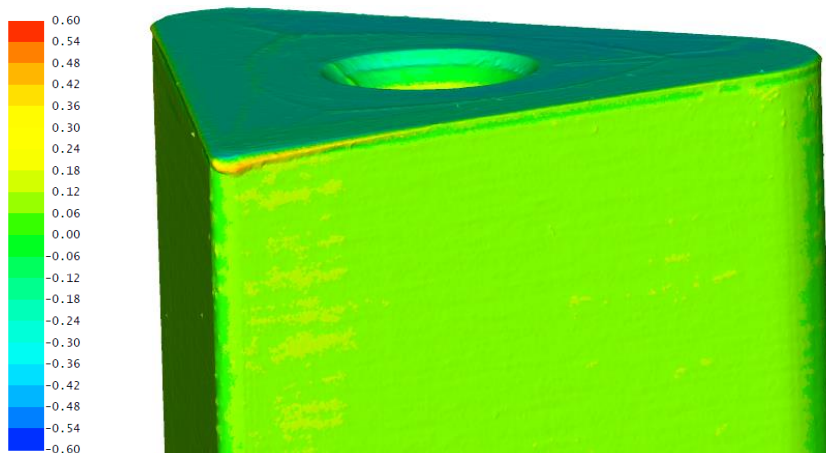


Figure 126: False-color image of the triangular matrix from above

No shrinkage phenomena appear on the counter tool after the first test. However, Figure 127 shows a clear change in geometry at the smallest radius. At this point, material is sheared off to the outside and the corner is rounded downward as a result. As the stylus moves counter-clockwise around the geometry, it can be seen that the greatest deformation occurs on the side after the stylus has moved around the corner or radius. In this area, a maximum deviation of 0.43 mm in the y-direction and 0.45 mm in the z-direction can be seen on the counter tool. In addition, it can be seen from the radii with an angle of 60° that deformation or shearing occurs on all three. The larger the radius, the smaller the shear. Figure 127 also shows that undercutting occurs below the edge, as with the cylindrical counter tool.



**Figure 127: Rounded corner of the triangular counter tool after the first attempt**

For the most part, the deformation of the counter tool can be easily understood on the sheet metal. The deviations on the uppermost triangular surface of the geometry are greatest at the radii (Figure 128A). However, the mean radius deviations are

(0.69 mm) a little smaller than that of the largest radius (0.73 mm). However, these deviations are roughly on the same level. The deviation at the smallest radius, on the other hand, is a lot larger at 0.91 mm. However, the largest deviations in the sheet metal are on the sloping surface and amount to almost 1.4 mm.

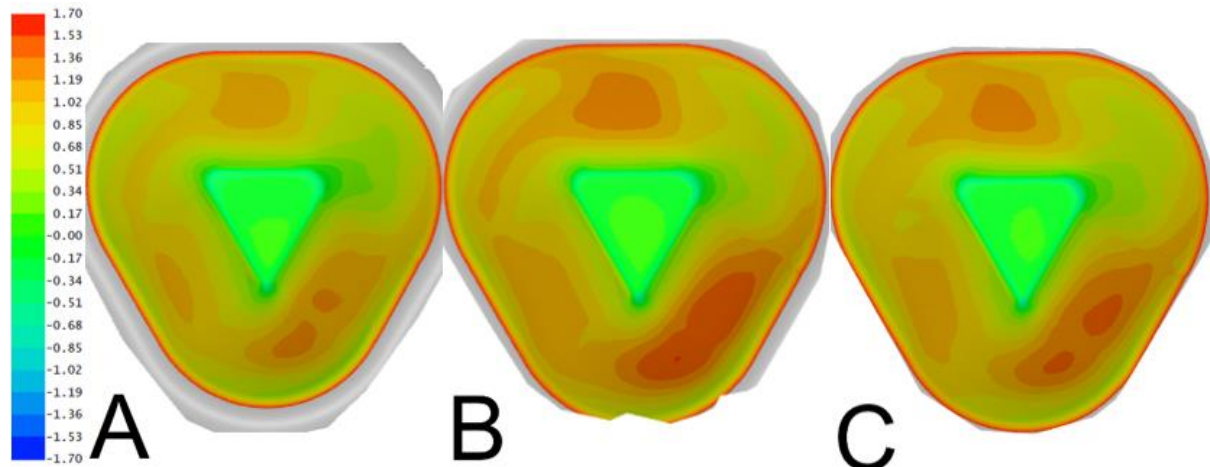


**Figure 128: Triangular sheets of the first (A), the third (B) and the fifth (C) test**

After the third attempt, this counter tool shows even more significant deviations at the corner with the smallest radius (Figure 129). The material is sheared further and the corner rounded down, so that there is a deviation from the target geometry directly at the corner of up to 0.7 mm in the z-direction. The other corners also show more shearing of the material than before, but are much closer to the target geometry than the corner with the smallest radius.



**Figure 129: Rounding of the corners of the triangular counter tool after the third attempt**

After the third test, the deformations of the counter tool can be seen on the sheet metal in terms of the size of the deviations at the corners. The extent of the deviation does not increase, but the ranges of this target-actual difference become larger (Figure 128B). Below the corner with the smallest radius, this means that the deviations after the third test increase by 0.2 - 0.3 mm compared to the first test.

After the fifth attempt, the counter tool shows no significant change compared to the measurement after the third attempt (Figure 130). The radii at the corners, especially in the sections, show that the shearing and rounding resulted in a more stable shape. The forces at these radii then act more extensively and not just at certain points on the edges.

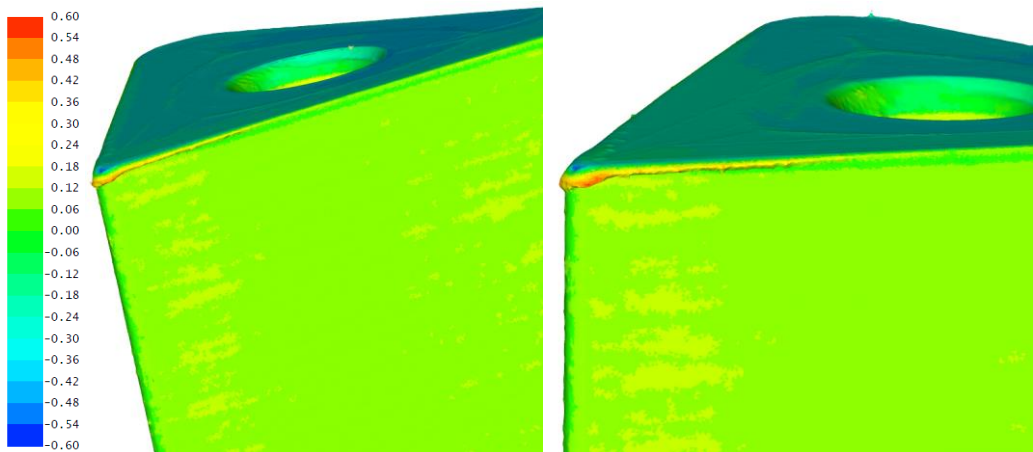


**Figure 130: Comparison of the triangular male part at the corner with the smallest radius between the measurement after the third attempt (left) and the fifth attempt (right)**

The measurement for the counter tool can be confirmed on the sheet of the fifth test, because the measured values are also very similar to those of the third test sheet (Figure 128C). The largest deviation diagonally below the corner with the smallest radius is smaller here at 1.45 mm compared to 1.55 mm. As already described for the other counter tools, this can be process-related.

The results of the triangular counter tool show that the corner radii should be at least 5 mm even with an angle of 60° between the surfaces. Here, too, the rounding of the corners and edges becomes clear. Therefore, the result confirms the previous statements regarding the provision of radii at corners and edges. Sharp corners with a small radius are not suitable for the ISF to absorb the forces.

The geometric properties of 3D-printed male parts for ISF were examined on a stenter specially designed and built for these tests using five different geometries. 1.2 mm thick EN AW-1050A H111 sheet metal was formed over the counterforms and the deviations of the male part and the sheet metal were measured after printing, the first, the third and the fifth test. These measurement results were compared with one another and, based on this, statements were made as to the suitability of various geometric elements for the counter tools.

In the course of the tests, the stenter has proven its suitability for the ISF. The counter tools basically withstood the process forces. In the case of the conical male part, there was almost no plastic deformation at all, and in the other four counter forms there were areas that were subject to plastic deformation. In most cases, the formed metal sheets clearly showed the

deformations of the counter tools. The tests showed that the 3D-printed counter tools are in principle suitable for the ISF. These counter tools are therefore a useful and material-saving alternative to milled wooden or plastic counter-moulds. However, the time required for the 3D printing, which can sometimes take several days, and the large geometric deviations is a negative aspect of this approach.

The positive and negative aspects of the 3D-printed male part with regard to the use for the ISF are listed in bullet points below.

## **7.8 WP8: Project management**

The dissemination strategy given in chapter 13 was adjusted and pursued during the project RapidSheet. Since the dissemination plan includes activities with national and international audience, it was ensured that the project results reach a wide audience. Additional user committee meetings and visits of interested companies enhanced the project visibility to industrial users whereas presentations on international conferences addressed the scientific community.

The project management was responsible to organize the conducted user committee meetings and steering committee meetings, see chapter 13. Thereby, discussions with participants of the user committee guided the developments towards the industrial needs.

During the project, the project management took also care of financial reporting between researchers and the founding organization.

## **8 Summary and Outlook**

RapidSheet realized machine concepts, process technology and simulation tools for additive technologies and incremental sheet metal forming. In the first step, the machine tool manufactured the counter tool in a large-scale additive manufacturing process that fulfills requirements such as fast production of a large bulk part with high surface quality, sufficient hardness, and highly accurate geometry also for nearly flat horizontal areas. After the printing, the machine tool formed sheet metal parts. Within the project this was demonstrated with a new developed 3-axes kinematic and a robot. For the optimization of the AM process and the ISF-process a model-based compensation was developed to avoid thermal and material behavior depending on deviations (e.g. necking and spring-back effects) as well as tool deviations due to forming forces. To tackle this challenge, new numerical simulation models with an adaptive refinement of meshes were developed in this project. Based on these simulations an optimized manufacturing strategy was deduced. In addition, a novel multi-sensor system was developed for measuring the tool deviations during ISF indepent from the machine tool kinematics. Future subsequent work will concentrate on the transfer of the project findings to innovative parts e.g. for micro-emobility, façade elements or design compoments.

## 9 Comparison of the results with the objectives of the proposal

The comparison of objectives and results is shown in Table 2.

Table 2: Comparison of objectives and results

Objectives	Results
<b>Comprising information about the performance of the new forming approach</b>	During the project new machine and robot systems for hybrid AM-ISF-processes were developed and evaluated.
<b>Design rules and requirements for printed dies for ISF processes:</b>	As result of the experimental and numerical process investigation design guideline describes cause-effect relationships as well as necessary decisions for design details was developed. It is now possible to include e.g. the warping/shrinking of the printed counter-tool as well as the forces and spring-back effects during the ISF into the design of the parts and tools. This enables users to establish the RapidSheet technologies at their own facilities.
<b>Comprehensive description of a process monitoring system</b>	The optical measurement system consists of several shadow imaging sensors each covering a subregion of the measurement range. Developed algorithms are used to evaluate the images of the shadow cast through a specially designed mask and consequently calculate the tool tip position. The quality of the recorded images increases with a brighter LED, a longer exposure time and a darker environment. Additionally, reflections by surrounding objects influence the measurement results. Measurement distances of at least up to 800 mm are achievable with a shadow imaging sensor. The lateral measurement range depends on the angle of incidence and is limited to approximately 300 mm. In the majority of the measurement range of a set of sensors, a position measurement uncertainty below 50 µm was achieved.
<b>Detailed information about the achievable part quality for the AM-ISF process,</b>	Especially for challenging part quality parameters like small radii and smooth surfaces very promising results could be achieved. It was found out that the relevant process parameters like the modifications of the stylus paths are important information for industrial users to achieve good-quality parts.
<b>Opportunity for SMEs to test their own geometries and sheets</b>	Tests were conducted in an implemented machine tool at IWU (AM and ISF) or a robot at Sirris (AM). The option to transfer the flexible tool system for a test to users is also given.
<b>Comprehensive numerical tools for the simulation of the combined AM- and ISF-process:</b>	The entire machine and process behaviour was investigated experimentally and by means of numerical simulation. In the result, digital twins of

	the AM and ISF process as well as the thermoelectric behavior of the developed machine tool were developed and verified.
--	--

## 10 Use of the grant

The use of the grant by the German institutes is shown in Table 3.

**Table 3 Use of the grant for the German institute**

Institute / Category	Sum
Fraunhofer IWU / A.1 • Scientific and technical staff Employees with completed scientific education	28,66 PM
Fraunhofer IWU / A.1 • Scientific and technical staff Employees with completed technical college education	0,28 PM
Fraunhofer IWU / B Equipment	0 €
Fraunhofer IWU / C Services provided by third parties	0 €
BIMAQ / A.1 • Scientific and technical staff Employees with completed scientific education	23 PM
BIMAQ / A.1 • Scientific and technical staff Employees with completed technical college education	0 PM
BIMAQ / B Equipment: The plan was to procure a workstation for real-time data processing. However, since storing the image data from 20 cameras in real time is not possible even with the workstation, this approach was not pursued. Instead, a concept was pursued in which the camera data is preprocessed decentrally on one Raspberry Pi 4 each and fused centrally on an industrial PC. In order to obtain the necessary funds for the procurement of the industrial PC, the funds for the workstation were reallocated accordingly with the amendment notice on 28.12.22.	3326.05 €
BIMAQ / C Services provided by third parties	0 €

## **11 Explanation of the necessity and appropriateness of the work performed**

The work done is fully in line with the proposal. In order to achieve the project goal, it was necessary and appropriate to investigate the possibilities of incremental sheet metal forming on tool machines with 3D printed counter tools. Without the implementation of these work packages, scientific work and the derivation of sound findings would not be possible.

## 12 Demonstration of the Scientific, Technical and Economic Benefits of the Results Obtained, in Particular for SMEs, as well as their Innovative Contribution and Industrial Applications

The results of this project are particularly important for SMEs, as they enable the production of individual sheet metal parts by using 3D printed counter tools for the incremental sheet metal forming process and provide important information on the design of production equipment and technology for potential users. Compared to conventional forming methods, the use of incremental sheet forming combined with additive manufacturing of the counter die significantly reduces the cost and number of tools required and reduces the time needed to obtain a finished component. The entire hybrid technology developed in this project can be based on commonly available devices in production plants: CNC machines or controlled welding robot arms. As a result, the enterprise's entry point into this technology requires minimal financial outlays. In addition, the developed simulation models and measurement system allow a more accurate manufacturing of large sheet metal parts. This makes the manufacturing technology even more attractive for customers and thus enhances the market for producing SMEs.

The results and their relevance for SME are shown in Table 4.

**Table 4 Results and their relevance for SME**

<b>Result</b>	<b>Relevance for SME, innovative add-on, industrial application</b>
FE ISF model	The developed numerical model of the incremental sheet forming process allows the SME efficient design and testing of various process setups depending on the geometry of the final product.
Material model identification software	The developed software allows the SME engineers a user-friendly evaluation of rheological parameters of the investigated material model based on experimental flow stress input data.
Combined extrusion and forming platform	The studies on the integrability of the ISF, extrusion and measurement process into a machine show the requirements, advantages and limitations of the developments to the applying SMEs and enable to reduce risks in investment decisions and to integrate new production equipment into manufacturing operations faster. The robotic extrusion cell at Sirris received attentions from various industrial, active in the field of robotics, renewable energy, composite manufacturing. Due to the rather innovative and unique nature of the cell and developed software various R&D and SME coaching projects were born from the integration, focusing both on the material, renewability and processing aspect.
FE machine model	Modeling the thermal influence of 3D printing and the kinetic effect of ISF on the displacement and twisting of the machine frame gives SME an indication of the misalignment that occurs when using light machine structures in this application, in addition to the typical spring-back phenomena of sheet metal forming.
Tool deflection measurement system	Laboratory studies show the potential of the developed shadow imaging system in ISF. The innovative technology is also particularly suited in other applications where a small region of interest is to be measured in a large measuring volume like robotic manufacturing. This technology is a new market for SMEs operating in the field of

	metrology. In addition, SMEs in the manufacturing sector can apply the measurement system to reduce geometrical deviations of produced parts.
--	---

### 13 Update of the plan submitted with the application for the transfer of results to industry, supplemented by an assessment of the feasibility of this transfer concept, which also includes all work published or to be published shortly in connection with the project

The realization of transfer of the investigation results of this project to industry and particularly to SME is given within the next three years.

The measures are shown in Table 5.

**Table 5 Measures for dissemination and exploitation**

<b>During project phase</b>				
<b>Time pe- riod</b>	<b>Activity</b>	<b>Objective</b>	<b>Responsible</b>	<b>Result</b>
twice per year	User committee meeting	Ensure the practical relevance of the project results to the UC (see WPs) select future and present test cases, get feedback, report project progress	IWU, BIMAQ	realized on 5.3.21, 27.9.21, 24.2.22 and 23.6.22
twice per year	User committee meeting	Ensure the practical relevance of the project results to the UC (see WPs) select future and present test cases, get feedback, report project progress	SIRRIS	done
each year	User committee meeting	Ensure the practical relevance of the project results to the UC (see WPs) select future and present test cases, get feedback, report project progress	AGH	realized on 5.3.21, 24.2.22, 23.6.22,
Project closure	User committee meeting	Final Project results and conclusion	IWU, SIRRIS, AGH, BIMAQ	realized on 3.11.22
Total duration of project	Publication of Project goals and research approaches on institute website	Communication between Consortium partners and UC	BIMAQ	<a href="https://www.bimaq.de/en/research/projekte/rapidsheet/">https://www.bimaq.de/en/research/projekte/rapidsheet/</a> publ. Jun.21, updated Jun.22
Six-monthly	Bachelor and master theses on the subject	Transfer the content of research	IWU, BIMAQ, SIRRIS, AGH	BIMAQ: 1 completed, 1 current AGH: 2 completed, 1 current IWU: 3 completed

				Sirris : 1 completed *
Total duration of the project	Reporting and Feedback towards DFMRS, MPC, SIRRIS and its different Working groups at conference, seminars, newsletters, publishing of final report	Information and marketing of project results within the sector and particularly to SMEs	IWU, SIRRIS, AGH, BIMAQ	Institutes provided conference and journal publications. An interim report with results from 2022 was handed to the DFMRS and the final report is prepared in collaboration.
Total duration of the project	Visits of interested companies	Informing & acquiring companies for the results of the project	IWU, SIRRIS, AGH, BIMAQ, DFMRS, MPC	24.2.22 Chemnitz, 12.5.22 Białystok, 12.6.22 Krakow, 27.6.22 Chemnitz
May 2022	Presentation of research results at Sensoren und Messsysteme 2022	Presentation of recent results	BIMAQ	10.-11.5.22 Nuremberg, publication **
August 2022	Presentation of research results at SAS 2022	Presentation of recent results	BIMAQ	1.-3.8.22 Sundsvall, publication **
September 2022	Publication of research results at SFU/ICRAFT in Chemnitz	Poster or integration in a paper	IWU	Poster presentation during industry session
2021	Project presentation on the Fraunhofer IWU website and VEMAS newsletter	Introduce project objective and expected results towards targeted SMEs.	IWU	Done
2022 (April)	Presentation of research results at CIRP Sponsored conference in Karpacz (international)	Presentation of recent results	AGH, IWU	Two presentations of research results at CIRP sponsored conference in Karpacz, Poland. **
2022 (September)	Presentation of research results at Forming conference (international)	Presentation of recent results	AGH	24th International Conference on Computer Methods in Mechanics (CMM) and the 42nd Solid Mechanics Conference (SolMech) in

				Swinoujscie, Poland. **
2022	Publication in national and international journals	Public presentation of research results		Done, see list below

\* Bachelor and master theses:

- K. Hammoud: Charakterisierung und Optimierung eines schattenbasierten Angulationsensors unter in-situ Bedingungen. Bachelor theses, 2022.
- F. J. Kenne Ngningaye: Aufbau und Charakterisierung eines Multi-Sensor-Systems mit Sensordatenfusion zur berührungslosen Werkzeugpositionsmeßung beim inkrementellen Blechumformen. Master theses, 2023.  
(to be submitted in Jul 2023)
- Magdalena Cyrańska: Development of an intelligent die for the micro forming process with real-time force measurement capability, Bachelor theses, 2023.
- Marcin Marszałek, 2022, Development and implementation of algorithms to control a robotic arm during an incremental forming process, Bachelor theses, 2023.
- Guillaume Paternostre de la Mairie : Optimisation d'un procédé d'additive manufacturing robotisé réalisant des moules pour le fromage incrémental de tôles, Master theses, 2021

\*\* Conference papers/ contributions:

- M. Terlau, A. von Freyberg, D. Stöbener, A. Fischer: In-Prozess-Messung der Werkzeugablenkung beim inkrementellen Blechumformen. 21. GMA/ITG-Fachtagung "Sensoren und Messsysteme 2022", Nürnberg, 10.-11.5.2022, pp. 90-96.
- M. Terlau, A. von Freyberg, D. Stöbener, A. Fischer: In-Process tool deflection measurement in incremental sheet metal forming. IEEE Sensors Applications Symposium (SAS 2022), Sundsvall, Sweden, 1.-3.8.2022, No. 1570797357 (6 pp.).
- Sitko M., Smyk G., Madej L., Development of inverse analysis software dedicated to the identification of flow stress model parameters, XXXIII CIRP Sponsored Conference on Supervising and Diagnostics of Machining Systems Manufacturing Autonomy Design and Research, IN, 26-30.06, Karpacz, Polska, 2022, short abstract.
- Perzynski K., Pawlikowski K., Madej L., Numerical analysis of the additive manufacturing process of support dies for incremental forming operations, XXXIII CIRP Sponsored Conference on Supervising and Diagnostics of Machining Systems Manufacturing Autonomy Design and Research, IN, 26-30.06, Karpacz, Polska, 2022, short abstract.
- Kräusel, V. et al., Investigation of the suitability of a tool element manufactured by fused filament fabrication for incremental sheet metal forming, SHEMET 2023, Nuremberg, Germany
- Matthias Demmler, Janine Gläzel, Alexander Geist, Dieter Weise, Alexander Pierer: Simulative Prozessauslegung für die geometrieflexible Umformung, in: maschinenbau Ausgabe 1/20.
- Pierer, Alexander & Wiener, Thomas & Hoffmann, Michael & Hauser, Markus & Naumann, Martin & Lara de León, Melvin & Mende, Matthias & Koziorek, Jiri & Dix, Martin. (2022). Inline Quality Monitoring of Reverse Extruded Aluminum Parts with Cathodic Dip-Paint Coating (KTL). Sensors. 22. 10.3390/s22249646.



After project closure				
Time period	Activity	Objective	Responsible	Result
2023	Final report	Presentation of research results	DFMRS, MPC, AGH	submitted 2023
2023	Final presentation	Public presentation of research results and discussion with the project steering committee and interested parties from industry and research	DFMRS, MPC, AGH	Submitted 2023
2023	Publication of results at conferences	Development of adaptive controller concept, discussion in professional circles	IWU, BIMAQ, SIRRIS, AGH	Realized on 4.4.23
2023	Publication in national and international journals	Public presentation of research results	BIMAQ, AGH	2 papers submitted in 2022/23, 2 papers published in 2023, ***
from 2023	Dissertation project staff	Research results are part of a PhD project	IWU, BIMAQ	from 2023
from 2023	Involvement in teaching	Integration in the context of cooperation with colleges and universities	AGH, BIMAQ	from 2023
2024 (May)	Presentation of research results at 56th CIRP Conference on Manufacturing Systems	Poster or integration in a paper	BIMAQ	will be done 2024 (May)
2024 (October)	Presentation of research results at 3DMC 2024	Poster or integration in a paper	BIMAQ	will be 2024 (October)

\*\*\* Papers submitted or published in 2023:

- A. von Freyberg, M. Terlau, D. Stöbener, A. Fischer: Optische Messung der Werkzeugablenkung in der inkrementellen Blechumformung. tm - Technisches Messen, 2023. doi.org/10.1515/teme-2022-0102
- K. Perzynski, K. Pawlikowski, L. Madej: The role of die definition in the numerical simulations of two-points incremental forming processes, Computer Methods in Materials Science, 23(1), 2023. https://doi.org/10.7494/cmms.2023.1.0795
- M. Terlau, A. von Freyberg, D. Stöbener, A. Fischer: Optical tool deflection measurement approach using shadow imaging. Measurement: Sensors (13 pp.) (submitted in May 2022)
- M. Terlau, A. von Freyberg, D. Stöbener, A. Fischer: Shadow imaging based multiple sensing approach for tool deflection measurement. Precision Engineering (12 pp.) (submitted in March 2023)

## Annex

### Annex 1: References

- 
- [1] N. Moser; D. Pritchett; H. Ren; F. Kornel: Ehmann and Jian Cao: An Efficient and General Finite Element Model for Double-Sided Incremental Forming, J. Manuf. Sci. Eng 138(9), 091007 (Jun 20, 2016)
  - [2] H. Meier; V. Smukala; O. Dewald; J. Zhang: Two Point Incremental Forming with Two Moving Forming Tools. KEM, Proc. of the 12th International Conference on Sheet Metal 344, 2007, pp. 599–605.
  - [3] Fatronik, Incremental sheet forming – industrial applications, International seminar on novel sheet metal forming technologies, Jyväskylä (Finland), 2006
  - [4] Hirt, G.: Begründung eines Schwerpunktprogramms. Modellierung inkrementeller Umformverfahren. Saarbrücken, 2002
  - [5] Jeswiet, J.: Rapid prototyping of a headlight with sheet metal. Transaction of NAMR/SME. Vol. XXX, 2002, pp. 33-38
  - [6] Leach, D.: A new incremental sheet forming process for small batch and prototype parts. Proceedings of the 9th Int. Conference on Sheet Metal, SHEMET 2001, Leuven, pp. 211-218
  - [7] Filice, L.: Analysis of material formability in incremental forming. Annals of the CIRPS, vol. 51/1/2002: 199-202
  - [8] Powell, N.: Incremental forming of flanged sheet metal components without dedicated dies. IMECE part B, J. of Engineering Manufacture, 1992, vol. 206, pp. 41-47
  - [9] Matsubara, S.: Incremental Backward Bulge Forming of a Sheet Metal with a Hemispherical Tool. J. of the JSTP, vol. 35, pp. 1311-1316, 1994
  - [10] Amino, H.; Makita, K.; Maki, T. Sheet Fluid Forming And Sheet Dieless NC Forming International Conference New Developments in Sheet Metal Forming”, Fellbach, Germany, 2000
  - [11] N .N.: Variants of incremental sheet metal forming, IUL TU Dortmund, 2021.
  - [12] Behera, A. K.: Accuracy improvement in single point incremental forming trough systematic study of feature interactions. In: Key Engineering Materials Vol. 473 (2011) pp. 881-888
  - [13] Malhotra, R.: IMPROVEMENT OF GEOMETRIC ACCURACY IN INCREMENTAL FORMING BY USING A SQUEEZING TOOLPATH STRATEGY WITH TWO FORMING TOOLS. In: Proceedings of the ASME 2011 International Manufacturing Science and Engineering Conference, MSEC2011, June 13-17, 2011, Corvallis, Oregon, USA
  - [14] Verbert, J.: Multivariate Adaptive Regression Splines as a Tool to Improve the Accuracy of Parts Produced by FSPIF. In: Key Engineering Materials, Vol. 473, 2011, pp. 841-846

- 
- [15] Bambach, M.: Strategies to improve the geometric accuracy in asymmetric single point incremental forming. In: Production Engineering – Research and Development, Feb. 2009 Published online, ISSN 0944-6524 (Print), 1863-7353 (Online)
  - [16] Micari, F.: Shape and dimensional accuracy in Single Point Incremental Forming: State of the art and future trends. In: Journal of Materials Processing Technology, Vol. 191, 2007, pp. 390 – 395
  - [17] Araghi, B. T. et al.:Investigation into a new hybrid forming process: Incremental sheet forming combined with stretch forming. CIRP Annals - Manufacturing Technology 58 (2009) 225–228
  - [18] Duflou, J. R.: Force Measurements for Single Point Incremental Forming: An Experimental Study. In: Advanced Materials Research Vols. 6-8, 2005, pp. 441-448
  - [19] Jeswiet, J.: Forces in Single Point and Two Point Incremental Forming. In: Advanced Materials Research Vols. 6-8, 2005, pp. 449-456
  - [20] Lixia, W., Qiuhe, Y, Shuqian, H.: Sheet Metal Multipoint Forming Technolgy Based on Hydro-forming. In: Advanced Materials Research, Vols. 179-180 (2011), pp. 1278-1281
  - [21] DIN 8584-3: Fertigungsverfahren Zugdruckumformen - Teil 3: Tiefziehen; Einordnung, Unterteilung, Begriffe.Berlin, 2003
  - [22] Scholz, Peter: Einsatz von Aluminiumschäumen als Matrizenwerkstoff bei der inkrementellen Blechumformung, Masterarbeit an der Fakultät für Maschinenbau der Technischen Universität Chemnitz, Professur Umformendes Formgeben und Fügen, Chemnitz, 2015
  - [23] Ames, J.: Systematische Untersuchung des Werkstoffflusses bei der inkrementellen Blechumformung mit CNC-Werkzeugmaschinen. Rheinisch-Westfaelische Technische Hochschule Aachen, Dissertation, 2008
  - [24] Li, M.-Z., Cai, Z.-Y., Li, X.J.: Principle and applications of multipoint matched-die forming for sheet metal. In: Proceedings of the Institution of Mechanical Engineers, Part B: Journal of Engineering Manufacture, Vol. 222 (2008), pp. 581-589
  - [25] Hundt, T., Schmidt, C., Denkena, B., Engel, K., Horst, P.: Variable forming tool and process for thermoset prepgres with simulation verified part quality. In: Key Engineering Materials Vols. 611-612, pp. 391-398
  - [26] Cai, Z.-Y., Wang, S.-H., Xu, X.-D. et al.: Numerical simulation for the multi-point stretch forming process of sheet metal. In: journal of materials processing technology, Vol. 209 (2009), pp. 396–407; IWU Augsburg
  - [27] Hundt, T.: Formwerkzeuge. Umformwerkzeug. Entwicklung und Erforschung eines beheizten modularen rekonfigurierbaren Umformwerkzeugs zur geführten endkonturnahen Formgebung von Prepeggelegen mit simulationsbasierten Aktorpositionierung. Hannover,2009
  - [28] H. Ren, J. Xie, S. Liao, D. Leem, K. Ehmann, J. Cao: In-situ springback compensation in incremental sheet forming, CIRP Annals 68 (1) (2019) 317-320. doi:10.1016/j.cirp.2019.04.042.

- 
- [29] P. Konka, R. Lingam, U. A. Singh, C. Shivaprasad, N. V. Reddy: Enhancement of accuracy in double sided incremental forming by compensating tool path for machine tool errors, *The International Journal of Advanced Manufacturing Technology* 111 (3-4) (2020) 1187–1199. doi:10.1007/s00170-020-06149-1.
- [30] P. Konka, R. Lingam, N. V. Reddy: Tool path design system to enhance accuracy during double sided incremental forming - an analytical model to predict compensations for small/large components, *Journal of Manufacturing Processes* 58 (2020) 510–523.
- [31] T. Pfeifer; R. Schmitt: *Fertigungsmesstechnik*, 3. Auflage, Oldenbourg Verlag, München, 2010.
- [32] U. Mutilba, J. A. Yagüe-Fabra, E. Gomez-Acedo, G. Kortaberria, A. Olarra: Integrated multilateration for machine tool automatic verification, *CIRP Annals* 67 (1) (2018) 555–558. doi:10.1016/j.cirp.2018.04.008.
- [33] N. A. Sazonnikova, V. N. Ilyuhin, S. V. Surudin, N. N. Svinarov: Increasing of the industrial robot movement accuracy at the incremental forming process, in: 2020 International Conference on Dynamics and Vibroacoustics of Machines (DVM), IEEE, 2020, pp. 1–8. doi:10.1109/DVM49764.2020.9243898.
- [34] G. Berkovic, E. Shafir: Optical methods for distance and displacement measurements, *Advances in Optics and Photonics* 4 (4) (2012) 441–471. doi:10.1364/AOP.4.000441.
- [35] E. Grenet, P. Masa, E. Franzi, D. Hasler: Measurement system of a light source in space (2015).
- [36] M. Pietrzyk; L. Madej; L. Rauch; D. Szeliga: *Computational Materials Engineering: Achieving high accuracy and efficiency in metals processing simulations*, Elsevier, Amsterdam, 2015.
- [37] R. Verfürth: *A Review of A. Posteriori Error Estimator and Adaptive Mesh-Refinement Techniques*. B. G. Teubner, Stuttgart, 1996
- [38] . A. Meyer: *Programmer's Manual for Adaptive Finite Element Code SPC-PM 2Ad*. Preprint SFB393 01-18 TU Chemnitz, 2001.
- [39] S. Beuchler, A. Meyer, and M. Pester: *SPC-PM3AdH v1.0 - Programmer's Manual*. Preprint SFB393 01-08 TU Chemnitz, 2003.
- [40] L. Madej: Digital/virtual microstructures in application to metals engineering – A review, *Archives of Civil and Mechanical Engineering*, 17, 2017, 839–854.
- [41] D. Braess: *Finite Elemente Theorie, schnelle Löser und Anwendung in der Elastizitätstheorie*. Springer, Bochum, 2007.
- [42] A. Kumar, V. Gulati, P. Kumar: Investigation of process variables on forming forces in incremental sheet forming. *International Journal of Engineering and Technology* 10(3):680–684, 2018
- [43] P. Konka, R. Lingam, N. V. Reddy: Tool path design system to enhance accuracy during double sided incremental forming - an analytical model to predict compensations for small/large components, *Journal of Manufacturing Processes* 58 (2020) 510–523.
- [44] O. Martínez-Romero, M. L. García-Romeu, D. Olvera-Trejo, I. Bagudanch, A. Elías-Zúñiga: Tool Dynamics During Single Point Incremental Forming Process. *Procedia Engineering* 81:2286–2291, 2014